Aus der

Radiologischen Universitätsklinik Tübingen

Abteilung Präklinische Bildgebung und Radiopharmazie

Combining gene-editing with brain imaging: from genes to molecules to networks

Inaugural-Dissertation
zur Erlangung des Doktorgrades
der Humanwissenschaften

der Medizinischen Fakultät
der Eberhard Karls Universität
zu Tübingen

vorgelegt von

Marciano, Sabina

2024

Dekan:	Professor Dr. B. Pichler
1. Berichterstatter	Professorin Dr. K. Herfert
2. Berichterstatter:	Professor Dr. C. la Fougère

Tag der Disputation: 08.01.2024

Table of Contents

Combining gene-editing with brain imaging: from genes to molecules to networks

List of abbreviations

%ID/g	percent injected dose per gram
[^{11}C]TMP	[^{11}C]trimethoprim
[^{11}C]RAC	[^{11}C]raclopride
[^{11}C]MP	[^{11}C]methylphenidate
[^{11}C]DTBZ	[^{11}C]dihydrotetrabenazine
5-HT	serotonin
3-MT	3-methoxytyramine
AAV	adeno-associated viral vectors
AD	Alzheimer's Disease
BBB	blood-brain barrier
BP	binding potential
BP_{ND}	binding potential non-displaceable
CAG	cmv enhancer/chicken β-actin
Cas9	crispr-associated nuclease
CCW	counterclockwise
CER	cerebellum
CMV	cytomegalovirus
CRISPR	clustered regularly interspaced short palindromicrepeat
CW	clockwise
DA	dopamine
DAR	dopamine receptor
DAT	dopamine transporter
DHFR	dihydrofolate reductase
DIO	double inverted orientation
DOPAC	3,4-dihydroxyphenylacetic acid
D2R80A	dopamine type 2 receptor mutant
DSB	double strand break
DVR	distribution volume ratio
EcDHFR	E.coli dihydrofolate reductase
FBP	filtered back projection
FOV	field of view
FWHM	full width at half maximum
GFP	green fluorescent protein
HA-tag	hemagglutinin-tag
HBSS	hank's balanced salt solution
hCB_2	human type 2 cannabinoid receptor
HDR	homologous directed recombination
HEPES	4-(2-hydroxyethyl)-1-piperazineethanesulfonic acid
HPLC	high performance liquid chromatography
HSV1-tk	herpes simplex virus type 1 thymidine kinase
Hsyn	human synapsin promoter
HVA	homovanilic acid
i.v.	intravenous
IHC	immunohistochemistry

InDel	insertion deletion
KD	knockdown
L-DOPA	L-3,4-dihydroxyphenylalanine
LE	Long Evans
LOR	line of response
MRI	magnetic resonance imaging
NHEJ	non-homologous end joining
NLS	nuclear localization sequence
OSEM	ordered subset expectation maximization
PAM	protospacer adjacent motif
PD	Parkinson's Disease
PET	positron emission tomography
PFA	paraformaldehyde
PgP	p-glycoprotein
PKM2	isoform of pyruvate kinase
PVE	partial volume effect
RNAi	RNA interference
RNP	ribonucleoproteins
ROI	region of interest
RT-qPCR	quantitative real-time polymerase chain reaction
s.c.	subcutaneous
SaCas9	Cas9 derived from s*taphylococcus aureus*
SD	Sprague Dawley
SgRNA	single guide RNA
SN	substantia nigra
SNc	substantia nigra pars compacta
SNR	signal-to-noise ratio
SpCas9	Cas9 derived from s*treptococcus pyogenes*
STR	striatum
SUV	standard uptake value
TAC	time activity curve
TALENs	transcription activator-like effector nucleases
TH	tyrosine hydroxylase
VMAT2	vesicular monoamine transporter 2
VOI	volume of interest
WPRE	woodchuck hepatitis virus post-transcriptional regulatory element

1. Introduction

1.1. Overview

Understanding the molecular and functional signatures and the significance of genes in neurological disorders is primary in neuroscience. The genetic, molecular and functional alterations underlying the pathological changes in conditions like Parkinson's (PD), Alzheimer's (AD), and Huntington's diseases remain largely unknown and could serve as early markers of disease.

The overall aim of this work was to establish platforms to modulate genes and their encoded proteins and assess the outcomes of the gene perturbation non-invasively. In other words, the research goal was to couple gene-editing with *in vivo* imaging to longitudinally study how genes regulate brain molecular and functional dynamics. Our research has the potential to identify early neurobiological markers and promising therapeutic interventions. Within this framework, we carried out two studies.

In the first study, *"we combined the clustered regularly interspaced short palindromic repeats (CRISPR)-associated nucleases (Cas9) with in vivo positron emission tomography (PET) and functional magnetic resonance imaging (fMRI) in the adult rat brain to investigate the direct link between genes, molecules and the brain connectome"* [1]*. "Receptors, transporters, and ion channels play a role in neurological diseases, and genetic screenings are constantly discovering new targets whose mechanistic role in pathogenesis is not yet well understood. Our research focused on using CRISPR/Cas9 to knock down the Slc18a2 gene, encoding the vesicular monoamine transporter (VMAT2), involved in the storage and release of dopamine (DA). The extensive knowledge of the gene makes it an excellent basis for studying the gene-molecules-networks relationship"* [1].

CRISPR/Cas9 was chosen as Science's 2015 "Breakthrough of the Year" and awarded the Nobel Prize in 2020 [2, 3]. Already six years after the first relevant paper, CRISPR/Cas9-related publications raised from a few hundred to almost 5000 [4], highlighting the global research interest and the feasibility of this new technique. Developed in bacteria as a defense mechanism towards viruses, the system was engineered to modify any gene of interest in several organisms [5-13]. Significantly, CRISPR/Cas9 mutates, silences, induces, and replaces

genomic elements even in humans. CRISPR/Cas9 is employed in several clinical trials to treat cancer, thalassemia, human papillomavirus, optic neuropathy [14-16].

We applied CRISPR/Cas9 gene-editing in the adult rat brain, where traditional genetic tools have been difficult to adapt. *"Rats are particularly advantageous for imaging studies due to the larger brain size and limited spatial resolution and sensitivity of preclinical scanners [17]"* [1]. Notably, only two studies have employed CRISPR/Cas9 gene-editing in rats. However, the results of the gene perturbation have been investigated either through behavioral examinations or *in vitro* [18, 19]. Our experimental goal extended beyond those approaches in combining the genome-engineering platform with *in vivo* PET and simultaneous PET/fMR imaging. Besides its diagnostic relevance, PET allows the non-invasive quantification of protein expression changes *in vivo* and over time in the same subjects. Additionally, due to its high sensitivity in the nano- to picomolar range (10^{11} to 10^{12} mol/L) [20], it offers a reliable quantitative estimate of the neurochemical changes in regards to neurotransmitters synthesis, storage, release, and reuptake [21-27]. Therefore, the imaging modality enables a non-invasive, longitudinal investigation of the induced molecular changes in the rat brain. Compared to PET, MRI presents superior temporal and spatial resolution. Further, blood oxygen level dependent-functional MRI (BOLD-fMRI) indirectly detects neuronal activity via hemodynamic coupling [28], delineating the extent of functional connectivity (FC) between anatomically separated regions [29]. Therefore the two modalities are strongly complementary, as they provide molecular (PET) and functional information (BOLD-fRMI). The simultaneous application of PET/BOLD-fMRI enables the direct spatial and temporal correlation of both measurements [30-36], aiding in the understanding of the brain adaptations from molecules to networks.

We anticipate our combinatorial approach to be a starting point to investigate the impact of specific genes on the brain molecular-connectome dynamics, identifying early neurobiological markers and tailored therapies for normalizing brain function.

To provide a quantitative measure and monitor the Cas9 and sgRNA brain expression over time, it would be of interest to perform *in vivo* PET imaging with reporter gene probes. Despite several reporter genes have been developed in the last years, these show major limitations, which include f.e. endogenous expression in the brain, resulting in high background binding or low brain uptake [37-43].

In the second study, our goal was to carachterize the pharmacokinetics and metabolism of [^{11}C]trimethoprim (TMP), a promising PET reporter probe to image *E. coli* dihydrofolate reductase (*Ec*DHFR)-expressing cells in the rat brain. The radioligand is an analog of TMP, an antibiotic for clinical use, binding to *Ec*DHFR and crossing the blood-brain barrier (BBB) when given orally [44-46]. [^{11}C]TMP has shown great potential as reporter gene probe in xenografted tumor mouse models [47], binding with very low affinity to the mammalian DHFR (4-fold less) and being biologically inert [47]. As no studies on [^{11}C]TMP suitability for brain imaging were perfomed in the rat, our aim was to investigate the potential of [^{11}C]TMP to image *Ec*DHFR in the species.

1.2. State of the art

The neurotransmitter DA plays a vital role in brain functions ranging from pleasure and motivation to motor control. Imbalances in DA transmission can lead to various disorders, including depression, attention deficit hyperactivity disorder, psychotic disorders, and PD [48-54]. The molecular signatures underlying these diseases have not yet been fully clarified, and therapeutic interventions are still missing. Scientific research in the field remains a “hot topic” and focuses on identifying the mechanisms behind alterations of DA signaling.

In this regard, the potential of CRISPR/Cas9 to engineer animal models and dissect the underlying molecular alterations could help develop future interventions. CRISPR/Cas9 overcomes the costly and time-consuming breeding of germlines and allows gene-editing in adult and aged animals, avoiding compensatory changes occurring at early developmental stages. Beyond that, we prove that CRISPR/Cas9 can be used to disclose the direct link between specific genes and molecular dynamics if combined with PET imaging. Indeed,

molecular changes can be measured in the brain non-invasively, with high specificity and sensitivity, and over time with PET. One well-characterized example is the radioligand [^{11}C]RAC, a widely used DA receptor (DAR) antagonist, which determines the availability and release of DA non-invasively [55-57].

In summary, we combine *in vivo* CRISPR/Cas9 gene-editing with molecular brain imaging in the adult rat brain to study the gene-molecules relationship, outplaying the current approaches limited to assessing the editing efficiency and relying on invasive experiments (electrophysiology) or *in vitro* analyses.

Given the role of newly discovered molecules in neurological disorders' onset and progression, our work aids in the identification of early neurobiological markers and tailored therapeutic interventions, as it sets the fundamentals to study the molecular brain dynamics, non-invasively and over time.

1.3. DA signaling and related disorders

DA signaling alterations result from neuronal dysfunctions in the substantia nigra compacta (SNc), ventral tegmental area, striatum, prefrontal cortex, and hippocampus [58-60]. DA is synthesized through two steps via the enzymes tyrosine hydroxylase (TH) and DOPA decarboxylase. Then, it is packaged into vesicles by the VMAT2, which releases the neurotransmitter in the synaptic cleft in response to neural activation. Once released, DA exerts either inhibition or excitation on the target neuron by binding to its metabotropic receptors (DAR). Five subtypes of DAR have been identified, divided into two families: D1-like (D1R and D5R), excitatory or inhibitory, and D2-like (D2R, D3R, D4R), mainly inhibitory. DA is subsequently recycled in the presynaptic terminal through the DA transporter (DAT) and can be either repacked into vesicles or degraded to its metabolites homovanillic acid (HVA), 3-methoxytyramine (3-MT), and 3,4-Dihydroxyphenylacetic acid (DOPAC) by a set of enzymes: monoamine oxidase catechol-O-methyl transferase, and aldehyde dehydrogenase (Figure 1) [61].

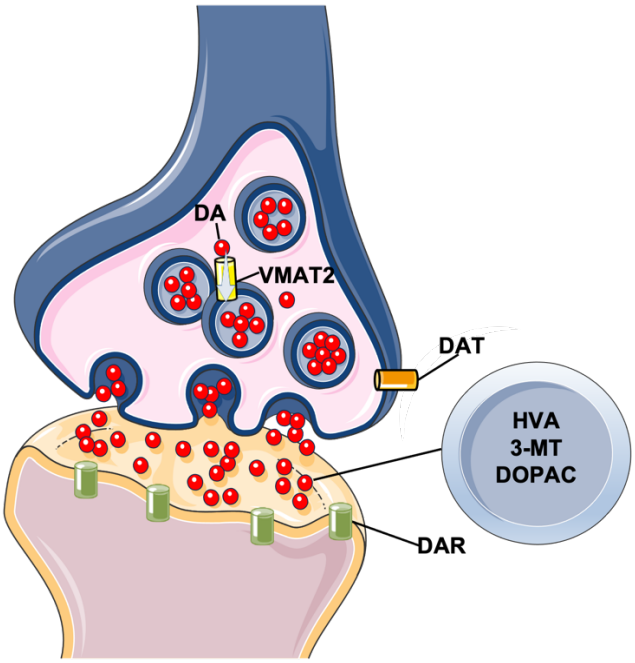

Figure 1: Simplified representation of dopamine (DA) signaling. DA (red) is embedded in presynaptic vesicles (blue) by the vesicular monoamine transporter 2 (VMAT2, yellow). Upon stimulation and calcium-mediated exocytosis, the neurotransmitter is released in the synaptic cleft and binds to DA receptors (DAR), located at the postsynapse (green). DA is either degraded into its metabolites homovanillic acid (HVA), 3-methoxytyramine (3-MT), and 3,4-Dihydroxyphenylacetic acid (DOPAC) or taken up in the presynaptic neuron through its transporter (DAT) (orange).

Being a highly reactive molecule, DA is considered a potential neurotoxin. If left unpackaged in the cytosolic environment, it can be particularly detrimental to the nigrostriatal neurons, which are susceptible to oxidative stress and lack antioxidant capacity [62, 63]. VMAT2 packages more than 90% of DA into vesicles [64], thus increasing neural response and exerting neuronal protection towards the neurotoxin. Therefore, a subtle balance of the DA concentration in the system is essential to avoid its accumulation and reduction, ultimately leading to psychotic or motor disorders such as schizophrenia, depression, and PD.

A dysregulated DA system contributes to positive, negative, and cognitive symptoms of schizophrenia. Schizophrenic patients present hyperactive DA transmission in the mesolimbic areas and hypoactive DA transmission in the prefrontal cortex [65-67]. Further, they show differences in DA contents in the prefrontal and cingulate cortex and hippocampus, as evidenced by PET studies [68]. As for the role of the neurotransmitter in depression, preclinical and clinical studies indicate that antidepressants enhance the DA neurotransmission in the

mesolimbic area [69, 70]. More precisely, chronic treatment with antidepressant drugs induces presynaptic DAR subsensitivity or postsynaptic DAR supersensitivity [71]. Further, depressed patients present a compensatory upregulation of D2R in the basal ganglia compared to healthy subjects [72]. Psychomotor retardation and diminished motivation are typical symptoms of depression, nevertheless also common to PD patients [5]. PD patients present motor comorbidities as key symptomatic features. The massive loss of DA in the SNc leads to a loss of signaling in the striatum, which triggers alterations in the thalamic area and frontal cortex [73]. The surviving dopaminergic neurons in the SNc and the increased density of striatal D1R and D2R mitigate the DA denervation, delaying PD symptoms [74-76]. Motor symptoms appear when 50 - 60% of dopaminergic neurons are lost, limiting effective treatments since the diagnosis is already severe [77].

As current therapies do not prevent or arrest DA-related diseases, there is an urge to solve the underlying molecular alterations and explore novel therapeutic targets to formulate more effective interventions.

1.4. VMAT2-mediated DA signaling

VMAT2 is a transmembrane carrier localized on the membrane of small and dense core vesicles within monoaminergic neurons expressing DA, serotonin (5-HT), norepinephrine, epinephrine, and histamine [78]. Interestingly, VMAT2 co-releases GABA in dopaminergic neurons, whereas the neurotransmitter is not synthesized *de novo* but taken up into the presynaptic neuron by its transporter [79, 80]. VMAT2 functions as a toxin-extruder antiporter, exchanging cellular toxins for extracellular protons at the cell membrane (Figure 2) [81].

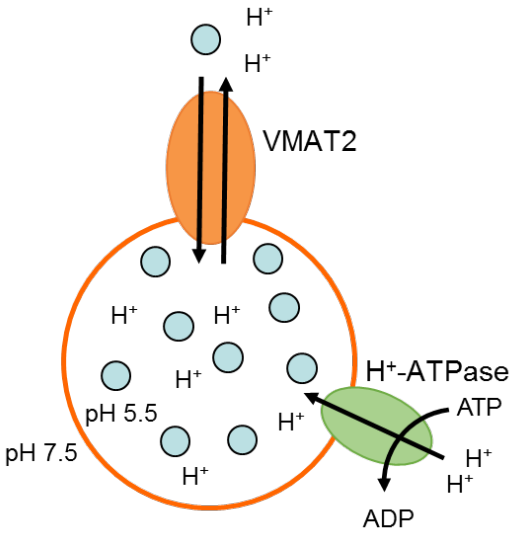

Figure 2: Vesicular monoamine transporter (VMAT2). VMAT2 (orange) uses ATP to transport 2 protons (H^+) from the cytoplasm to the vesicle, creating an electrochemical gradient across the vesicular membrane, thus promoting the release of 1 monoamine (blue circles).

VMAT2 plays an essential role in neurotransmission and neuroprotection, as it releases monoamines in response to neural activity and confines neurotoxins [82, 83]. Proper storage of DA in synaptic vesicles by VMAT2 favours neurotransmitter homeostasis and protects dopaminergic neurons from detrimental effects of DA accumulation. Indeed, the neurotoxic effects of misplaced DA, related to its cytosolic accumulation and oxidative stress, are known to play a role in PD [84-86]. Specifically, *Slc18a2* gain-of-function is protective towards PD [87, 88], while *Slc18a2* mutations cause infantile PD with motor and cognitive impairment [89]. Studies suggest that *Slc18a2* may also be a candidate gene for psychotic disorder. Indeed, its impact on the functional integrity of the striatal presynaptic DA system affects cognitive functioning and leads to schizophrenia and bipolar disorder [90-93].

To elucidate the role of the VMAT2 in neurological disorders, several investigators have deleted its coding gene in mice [94-97]. Besides the costly and time-consuming breeding, the gene knockout was not selective for the targeted neurons, resulting in the appearance of unselective behavior phenotypes [98].

1.5. CRISPR/Cas9

Many preclinical trials failed to translate into clinics because performed on animal models which did not fully recapitulate the disease pathogenesis [99]. This highlights the use of proper disease models to study the priming mechanisms and test novel therapeutics. Recently developed genetic tools provide a more useful means to generate preclinical models. CRISPR/Cas9 represents the most promising avenue to unveil the influence of genes on individual phenotypes, as it shows numerous advantages over other gene editing approaches, such as Transcription Activator-Like Effector Nucleases (TALENs) and RNA interference (RNAi) (Table 1).

Table 1: Comparison between gene-editing strategies. Clustered regularly interspaced short palindromic repeats (CRISPR)-associated nucleases (Cas9) (CRISPR/Cas9), Transcription Activator-Like Effector Nucleases (TALENs), and RNA interference (RNAi).Table adapted from [100].

	CRISPR/Cas9	TALEN	RNAi
Target	Genomic DNA	Genomic DNA	mRNA
Modification	Knockout	Knockout	Knockdown
Components	Cas9, sgRNA	2 TALENs	siRNA or shRNA
Time	Medium	Long	Short-Medium
Cost	Low	High	Low-High
Off-Target effects	Low	Low	High
Ease of experiment	Easy	Moderate	Easy

CRISPR/Cas9 editing has shown potential in neuronal cells in several species [7-11, 13, 101, 102]. It overcomes the need to breed genetically modified rodents, a costly and time-consuming process (9 – 12 months to get the desired progeny) [103]. Remarkably, CRISPR/Cas9 components can be injected into adult animals, avoiding compensatory changes occurring at early developmental stages. Importantly, CRISPR/Cas9-edited animals carry mutations on the endogenous gene, thereby providing better disease models than germlines, in which exogenous promoters drive the mutations.

1.5.1 Mechanism

CRISPR/Cas9 edits single or multiple genes *in vivo*, elucidating the role of encoded proteins in certain diseases. The system embodies the Cas9 nuclease, which snips through the DNA like a pair of molecular scissors. The nuclease is driven to the target genomic sequence by a small RNA molecule (single guide RNA, sgRNA) and produces a double-strand break (DSB) 3 bp upstream of a protospacer adjacent motif (PAM) (Figure 3).

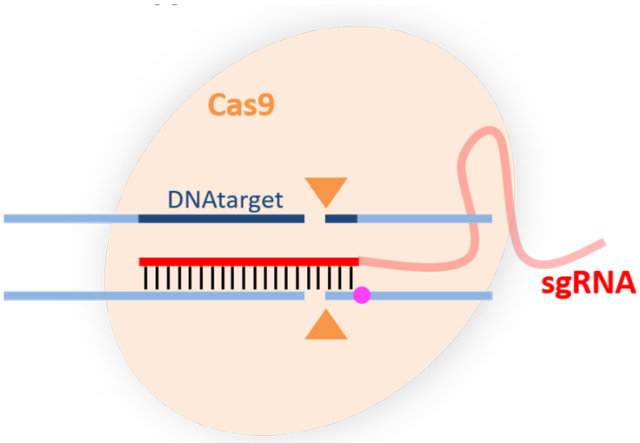

Figure 3: Scheme of the CRISPR/Cas9 system. The Cas9 nuclease (orange) is targeted to the genomic DNA (blue bar) by a sgRNA (red) consisting of a scaffold component, which serves for the interaction with the Cas9 and a variable sequence of 20/22 nucleotides (nt), which directs the Cas9 to the target DNA site (dark blue bar) using standard DNA-RNA complementarity base-pairing rules. Hence, the Cas9 mediates a double-strand break three bp upstream of a protospacer adjacent motif sequence (PAM, pink). Thus, in the presence of the PAM string, the Cas9 nuclease can be directed to any DNA of interest by simply altering the first 20/22 nt of the sgRNA corresponding to the genomic target sequence.

Following the DNA cleavage, the cell's native repair machinery mends the cut via non-homologous end-joining (NHEJ) or homologous directed recombination (HDR). NHEJ binds the DSB together, introducing random insertion/deletion (InDel) at the breakpoint junctions. HDR uses a DNA sequence as a template leading to precise editing (Figure 4) [104].

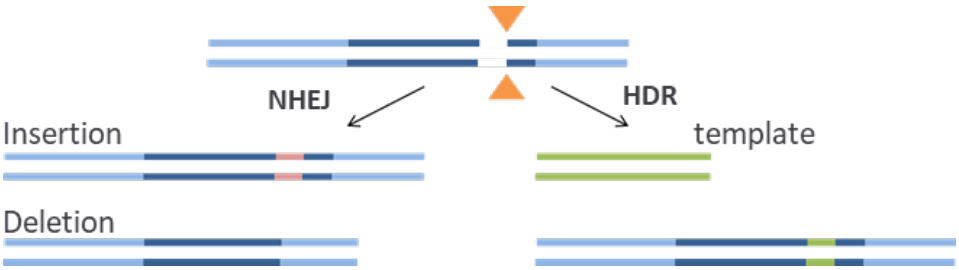

Figure 4: Repair mechanisms following the Cas9-induced double-strand break (DSB). The DSB, induced by Cas9 (orange arrowheads), is repaired through *(i)* non-homologous end joining (NHEJ), an error-prone process that produces insertions/deletions disrupting the gene of interest. *(ii)* homology-directed repair (HDR), if a DNA template is provided, allowing for precise gene-editing.

Hence, depending on the experimental objective, one could use the cellular DNA damage repair mechanisms to achieve gene destruction (NHEJ) or correction (HDR). However, NHEJ repair takes place more frequently than HDR since it happens in cellular growth (G1) and mitotic (M) phases [105]. HDR occurs in the S/G2 stages of the cell cycle, limiting its use in postmitotic neurons [106].

1.5.2 Applications

The most obvious benefit of CRISPR/Cas9 use in human research lies in its potential to eradicate deadly genetic diseases. Its therapeutic application might have an enormous impact on human health; for correcting over 600 genetic diseases [107-109]. Beyond its therapeutic potential, the gene-editing platform could be employed in animal species to model diseases and shed light on the molecular changes arising from manipulating specific genes. Numerous CRISPR/Cas9 preclinical trials involving pigs [7, 101], non-human primates [8], zebrafish [9, 102], mice [10], drosophila [11], and bacteria [110] have shown encouraging results. Also, its recent use in plants like rice [111], tobacco [112], and crop [113] offers a promising avenue in agricultural biology and biofuel production. CRISPR/Cas9 potential is continuously expanding with novel applications beyond gene silencing and correction. Indeed, a catalytically dead Cas9 lacking nuclease activity but retaining DNA binding ability with no apparent loss of target or binding specificity allows the live imaging of genomic loci and transcriptional regulation [114-118]. CRISPR-epigenomic thrives among the latest application and could be used to disclose the relationship between epigenetic markers and gene expression [119]. Further, the RNA-targeting Cas13 family of effectors shows higher RNA KD efficiency than shRNA and CRISPRi [120, 121]. Recently, the potential of the Cas12a family to modify up to 25 targets at once in a single cell has been harnessed [122]. Moreover, efficient and specific base-editing can be performed in human cells without introducing DSB [123].

1.5.3 Challenges

Cas9 nuclease permanent expression leads to gene-editing outside the target locus and potentially to mutations on other genes, as it can tolerate mismatches between the target sequence and the sgRNA (up to 5 within the protospacer region and the PAM) [124]. These off-target effects represent the main drawback of CRISPR/Cas9 and a great concern related to its application in humans. Several bioinformatics tools predict off-targets based on the homology to the target sequence. They can be employed to select the sgRNA with the least off-target probability [125]. A Cas9 (D10) that nicks the DNA instead of cutting both strands minimizes the likelihood of off-target events. However, D10Cas9 requires two sgRNAs, two PAMs, to make a functional nickase, limiting the target sites [126]. Truncating the sgRNA might also reduce the off-targets; however, shortening the sgRNA length reduces the number of target sequences [127]. The introduction of Cas9 at high concentrations, besides its long-lasting expression, increases the appearance of off-target events. Most likely, once all the target sites have already been cleaved, DSB will be directed towards off-target sequences [128]. Recently synthesized anti-CRISPR/Cas9 proteins could be delivered post-editing to inhibit Cas9 unnecessary persistent activity and editing errors outside the target region [129]. Notably, undesired targeting of cells outside the area of interest can also be considered an off-target event. Proper delivery cargos for CRISPR/Cas9-components therefore limit the occurrence of off-targets (see section delivery).

Another main challenge to be faced when administering CRISPR/Cas9 *in vivo* are the immune responses elicited towards the system's components. Indeed, the overall immunogenicity of the CRISPR/Cas9 complex, being of bacterial origin, needs to be addressed as persistent Cas9 expression favors antigen presentation. While the innate immunity, triggered by the nucleic acid cargo, does not appear frequently, the adaptive immunity, directed against Cas9, is common and seems to be pre-existing in the human population due to the exposure via the microbiome [130]. This pre-existing adaptive immunity represents a significant drawback, particularly concerning clinical studies, as, besides the

safety issues, it might affect the gene therapy efficacy. To overcome this critical limitation, CRISPR/Cas9 could be delivered through nanovectors shielding the immunogenic Cas9 from antibodies recognition [119].

1.5.4 Delivery

While CRISPR/Cas9 holds tremendous potential, its practical application is not straightforward. Indeed, Cas9 and sgRNA need to be delivered to the nucleus of target cells, minimizing immunogenic reactions and off-target events. The nuclease delivery is particularly challenging due to its high molecular weight and gene length. CRISPR/Cas9-components can be administered in different formats such as *(i)* RNA, produced through *in vitro* transcription or synthetic polymerization, *(ii)* single plasmid DNA (spDNA) and viral vectors, which need to translocate into the nucleus for transcription, or *(iii)* preformed ribonucleoprotein (RNP) complexes, which can be delivered through lipidic, polymeric or inorganic nanovectors. RNPs show higher editing efficiency when directly compared to spDNA [131], can generate the desired editing within 3 hours, and are cleared out after 24 hours, limiting the toxicity and off-targets derived from the persistent Cas9 expression [132]. In addition, RNPs *in vivo* effects and limited immunogenic reactions have been successfully validated in the mouse brain [133]. For these reasons, RNPs are considered the new frontier for CRISPR/Cas9 transfer. Nevertheless, adeno-associated viral (AAV) vectors, non-pathogenic viruses infecting mammalian cells at all cell cycle stages, represent the current primary mode of delivery. Indeed, AAV gene transfer is relevant for most neuroscience applications and indispensable for disease modeling. AAVs can be modified to target specific sequences in the host genome and present excellent tissue spread, stable transgene expression, versatility, low immunogenicity, and translational potential [10, 134, 135]. Nevertheless, the AAVs' main hindrance is the limited packaging capacity [136], which restricts the use to smaller Cas9 such as the ones derived from *Campylobacter jejuni*, *Streptococcus thermophilus, Neisseria meningitides,* and *Staphylococcus aureus* (SaCas9) [137-141]. Besides overcoming the AAV-packaging constraints, SaCas9 shows the same cleavage rates, reduced off-targets, and effective nuclease activity *in vivo*

compared to the better-characterized *Streptococcus pyogenes* Cas9 (SpCas9) [142]. Nevertheless, its PAM sequence is less abundant [18, 143, 144].

Significantly, the editing efficiency of CRISPR/Cas9-components delivered through AAVs relies mainly on the choice of the AAV-serotype, which is responsible for the tropism towards the cells of interest. The recombinant AAV serotype AAV2/1 is the most employed to target nigral neurons due to its widespread and high transduction frequency [145, 146]. However, recent experiments show the greatest neuronal transduction rate with the AAV-PHP.EB in both adult and neonatal rats [147]. This novel serotype is derived from the AAV9 capsid, from which it differs by a heptamer amino acid insertion [148, 149]. AAV.PHP.EB is the enhanced version of its precursor AAV-PHP.B and shows a higher brain tropism and transduction rate [150-152]. It has the tremendous advantage of permeating the BBB, leading to vast gene transfer and long-term expression (up to 12 months) in the striatum, cerebellum, and cortex [152]. AAV-PHP.EB is also suitable for local vector delivery and produces significantly higher focal expression in the rat SN, even when multiple vectors are administered simultaneously, compared to previously tested serotypes [147, 148]. Further, it is suitable for CRISPR/Cas9-components delivery [150]. Yet, AAV-PHP.EB dose-response studies in adult rats are missing, and the serotype has shown strain-limitations in mice [153].

1.6. PET imaging

PET imaging provides a non-invasive tool to measure molecular changes in the brain with high specificity and sensitivity over time. PET relies on the detection of γ-rays emitted by neutron-deficient isotopes that dispose of the surplus of positive charge, turning a proton into a neutron through nuclear transmutation. As a result, a positive electron (positron, e^+) and an electron neutrino (v_e) are emitted. While the neutron escapes without interactions, the positron interacts with the surrounding tissue until it annihilates, at a certain distance r, with an electron. As a result, two photons (γ) are ejected in opposite directions, describing a trajectory termed line of response (LOR), within the same coincidence timing window (Figure 5A). Positron emitters are used to label biologically active molecules

absorbed or metabolized in the body (oxygen, ammonia, glucose) or specific substrates of molecular targets (receptors, transporters). Their distribution in the target tissue is quantified through detectors, termed scintillators. Scintillators convert the energy of the γ-ray pairs into visible light and must be placed in opposite directions and circular configuration (Figure 5B) [154].

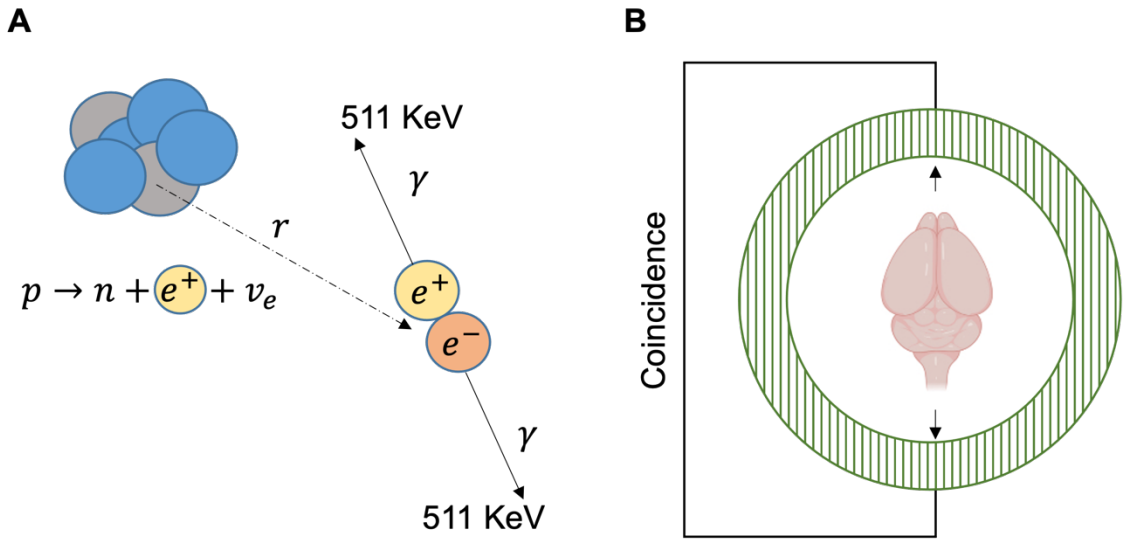

Figure 5: Formula and representation of the nuclear transmutation process and PET detection mechanism. A: Positive electrons (e^+), emitted from the unstable nucleus of the isotope, collide with the electrons (e^-) of the surrounding tissue. The distance of the positron to the annihilation point is indicated with r. As a result of this annihilation, two photons (γ) are ejected with the energy of 511 KeV in opposite directions as shown in B: The two photons that strike the PET detectors, at nearly identical times, are recorded as coincident. Brain icons in the figure were created with BioRender.com

Scintillators are typically made of crystalline materials like lutetium oxyorthosilicate or bismuthgermanate and must possess high light output, high stopping power, and good timing, energy, and spatial resolution. The latter depends on the radial offset and represents the distance where two infinitely small point sources can still be distinguished from each other. The spatial resolution of small animal PET systems equals 1.5 - 2.5 mm and is measured as the full width at half maximum (FWHM) of the point spread source in the center field of view (FOV).

Upon the impact of the photons with the scintillating crystals, the visible light is converted into an electric signal by photomultiplier tubes or avalanche photomultipliers and transformed into a digital signal by analog-digital converters.

However, not all the acquired events contribute to the signal, indeed not only true coincidences (photons from the same positron annihilation) (Figure 6A) but also random events (photon pairs from uncorrelated annihilations detected in the same coincidence timing window) (Figure 6B) and scatter events (photons from the annihilation pair which scatter and lose energy before reaching the detector) (Figure 6C) can contribute to the background noise [154].

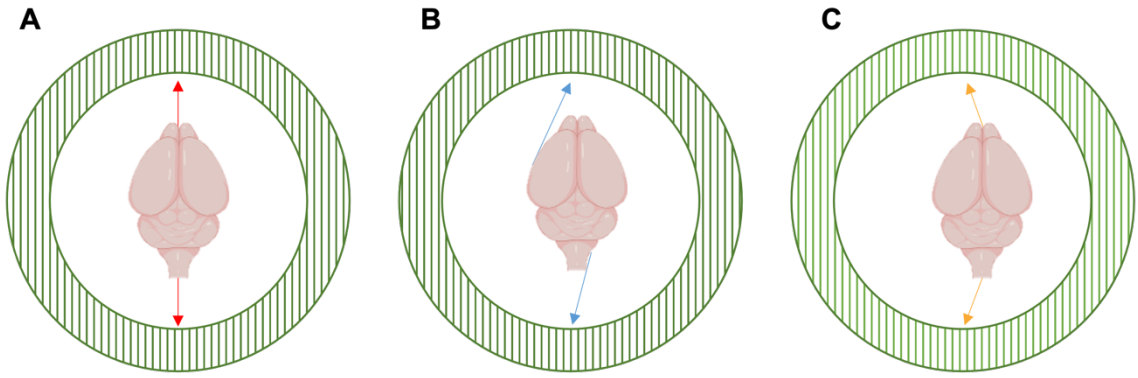

Figure 6: Types of coincidence events. True (A), random (B), and scatter (C) coincidences. In the last two types of coincidences (B, C), the annihilation event does not lie on the line of response (LOR) between the two-photon detections. Brain icons in the figure were created with BioRender.com

The missed detection of the scattered photon pairs, termed attenuation, depends on the scanner circular geometry and tissue depth, and is ~ 20% in rats [155]. The attenuation leads to data underestimation and must be measured with magnetic resonance imaging (MRI), computed tomography systems, or subtracting the signal of a transmission source (e.g., ^{57}Co or ^{68}Ge) rotating around the subject to the signal derived from a blank scan (acquired without the subject). Besides the attenuation, the dead time and the partial volume effect (PVE) might worsen the image quality and lead to biased quantification of the acquired PET data. The dead time is the time window required to register a second event, depends on scintillators and electronic components, and is corrected performing statistical measures. The PVE leads to spillover to the surrounding tissues in objects smaller than three times the spatial resolution and is estimated performing scans on phantoms of known size [154].

After the photons' detection, the applied corrections, and the digital post-processing, the PET raw data are reconstructed into an actual image.

Mathematical algorithms such as the analytical 2-dimensional (2D) filtered back projection (FBP) or the iterative ordered subset expectation maximization (OSEM) can be applied. FBP reconstruction is the most used algorithm due to its fast and robust nature. However, OSEM leads to high-quality images with improved signal-to-noise ratios (SNR), contrast, and spatial resolution [156]. Further, it outperforms FBP also in terms of binding values estimates for certain radioligands [157]. The choice of the reconstruction algorithm is therefore a compromise between the computing times and the statistical relevance of the data and relies on the radioligand of interest and study design.

1.6.1 PET imaging and dopaminergic transmission

PET has become an essential tool to study regional physiology in humans and has been extensively used for the differential diagnosis of neurodegenerative diseases [158]. Due to the lack of definitive diagnostic tests and conditions such as Lewy body dementia, AD, multiple system atrophy, and PD presenting similar clinical patterns, PET imaging with DA markers becomes crucial. Besides its relevance in clinical diagnosis, PET imaging is also beneficial for validating animal models of disease and studying non-invasively and over time the molecular brain architecture. Indeed, due to its high degree of sensitivity, PET measures DA synthesis, storage, release, and reuptake, promoting the identification of novel therapeutic targets [20-27]. PET ligands for the VMAT2, DAT, and DAR sites measure the DA functioning on pre and postsynaptic terminals, giving insights into the molecular dynamics of neurodegeneration [159-163] psychotic disorders [164-167], and addiction [168-170]. Further, PET is used to image neurotransmitter release using receptor-ligand tracers, such as [^{11}C]RAC, whose binding is sensitive to the concentration of the endogenous neurotransmitters. These experiments assume that the radioligand and the neurotransmitter compete for the same receptor binding site [56]. The increase in neurotransmitter release causes the displacement of the radioligand from its binding site hence, a decrease in its specific binding. Vice versa, the neurotransmitter reduction increases the receptor availability leading to increased

radioligand binding. The change of specific binding reflects the change of neurotransmitter concentration [171].

1.6.2 Kinetic modeling

Depending on the study design, PET scans can be acquired in static or dynamic mode. When working with a radioligand with known kinetics, a static acquisition can be performed when the equilibrium between the target and reference region is reached. Instead, the radioligand distribution in the target tissue can be mapped performing PET scans in dynamic mode; the acquisition lasts from the moment the radioligand is administered until it is cleared out of the system. Thus, while the results of static scans are expressed in a semi-quantitative values, in the form of standard uptake values (SUV), and percent injected dose ($\%ID$), the dynamic data can be quantified using kinetic modeling.

In the static acquisition, the total amount of radioligand in the tissue is quantified, for a drawn region or volume of interest (ROI, VOI), as the radioactivity normalized to the injected dose ($\%ID$) or the injected dose per body weight (SUV) [172]:

$$\%ID = \frac{C_{img}}{C_{inj}} \left[\frac{\frac{MBq}{mL}}{MBq} \right] \times 100 \quad [1]$$

$$SUV = \frac{C_{img}}{C_{inj}} \left[\frac{\frac{MBq}{mL}}{\frac{MBq}{g}} \right] \quad [2]$$

Where C_{img} is the image-derived radioactivity concentration in the tissue and C_{inj} is the ID. Nevertheless, the $\%ID$ and SUV mirror the radioactive concentration in the target tissue relying solely on the injected radioactivity. However, the radioactivity concentration depends as well on the physiology of the tissue (blood flow, metabolism) and on the input function, which is the time course of radioactivity concentration in the blood/plasma. Ultimately, both define the availability of the radioligand in the target tissue. Hence, the dynamic PET data and the extracted input functions are needed to determine the *in vivo* kinetics of the radioligand, as they provide information on its distribution in tissue and blood, respectively [172].

1.6.2.1 Compartmental models

In a dynamic PET study, PET data are obtained over time after the tracer is administered. To interpret the PET data, one can assume that there are separate pools of tracer as “compartments”. Yet, to model the PET data as compartments several assumptions need to be met: *(i)* the physiological processes are at equilibrium and *(ii)* are not influenced by the radioligand administration and PET acquisition, *(iii)* the concentration in the compartments is homogeneous, and the radioligand transfer is not gradient driven. With these assumptions in mind, one has to look at compartments not as physical volumes but as different states of the radioligand (e.g., bound, free, unspecifically bound) (Figure 7) [172].

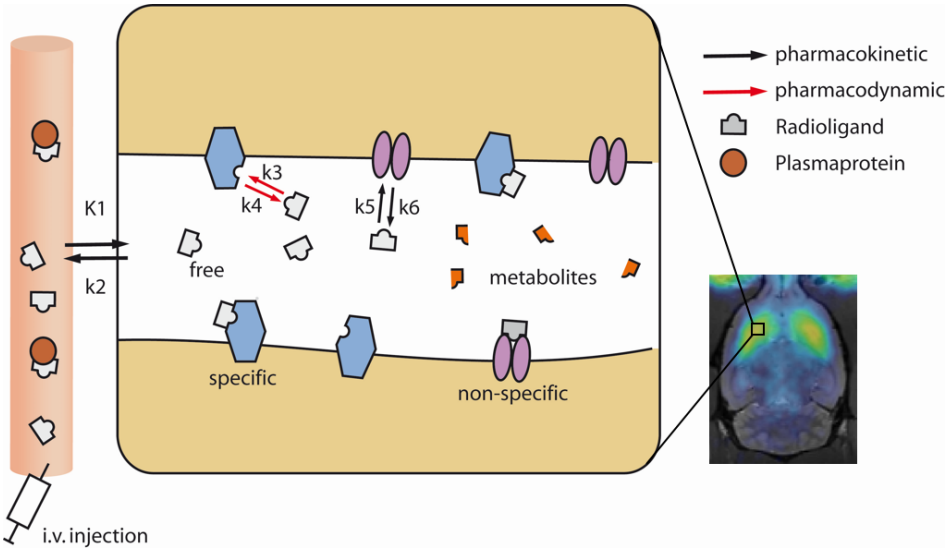

Figure 7: Radioligand distribution from the blood to the tissue. Following its intravenous (*i.v.*) administration, a fraction of the radioligand may bind to plasma proteins and not travel into the brain. The remaining quote may cross the capillary membrane and enter the tissue. From here, the radioligand may be free, specifically bound to its substrate, or non-specifically bound to another target. The binding may be defined by reversible or irreversible kinetics. Figure courtesy of Prof. Dr. K. Herfert.

The simplest model is the 1 tissue compartment model (1TCM) and defines the concentration of the radioligand distributing from the plasma to the tissue (described with K_1) and back to the plasma (described with k_2) (Figure 8A).

k_2 holds information concerning flow, tracer extraction, and partition coefficient. If the radioligand concentration in the blood remained constant, its concentration in the tissue would also become steady, and equilibrium would be achieved. The

ratio of the radioligand concentration in the target region and plasma at equilibrium is the partition coefficient (V_T, volume of distribution), defined as:

$$V_T = \frac{C_T}{C_P} = \frac{K_1}{k_2} \quad [3]$$

An essential application of 1TCM is measuring regional blood flow (perfusion). Radioligands used for this purpose are [^{15}O]H_2O, [^{15}O]butanol, [^{11}C]butanol.

In the 2TCM, an additional compartment is described, which identifies with the fraction of radioligand binding reversibly to the substrate (described with k_3) and then displacing to its free or non-specifically bound state (described with k_4).

For radioligands with irreversible binding or those which are trapped in the cell, e.g., [^{18}F]FDG, k_4 is set to zero. For radioligands with high specific binding to a receptor and low non-specific binding, e.g., [^{11}C]RAC, k_5 and k_6 can be neglected, and C_F and C_{NS} combined to a single compartment (Figure 8B). Instead, for radioligands with high non-specific binding to the substrate, k_5 and k_6 can be defined using a 3TCM. However, this model requires fitting of 6 parameters and might lead to unreliable fits (Figure 8C) [173].

Therefore, the choice of the model is a trade-off between parameters introduced to gain a good fit and the statistical errors. For most radioligands, C_F and C_{NS} can be combined into one single compartment assuming that k_5 and k_6 are infinitesimal small and a 2TCM can be applied.

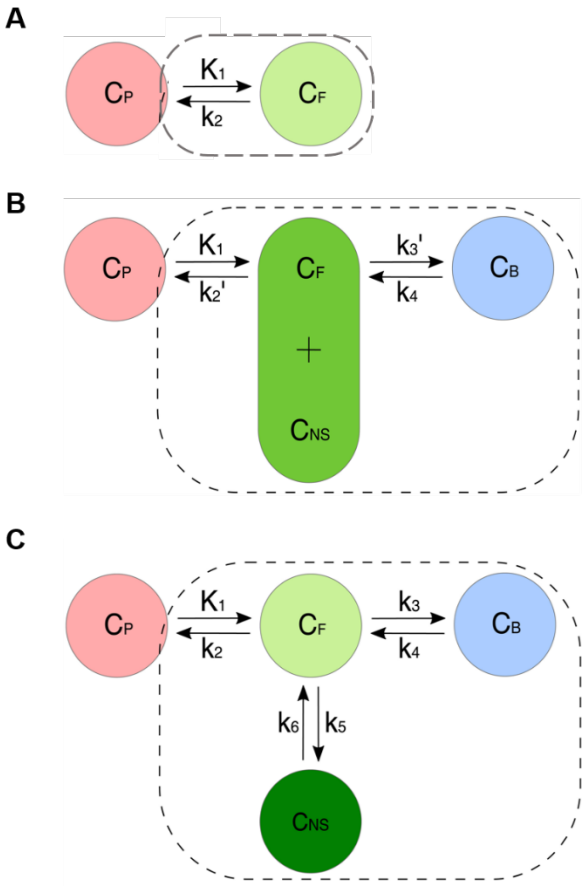

Figure 8: Tissue compartment models. A: 1-tissue compartment model. B: 2-tissue compartment model. C: 3-tissue compartment model. C_P: radioligand in plasma, C_F: free radioligand in tissue, C_B: radioligand specifically bound to a substrate, C_{NS} non-specifically bound radioligand in tissue. Figure adapted from [173].

To estimate the rate constants, an arterial input function is required. The input function can be derived from *(i)* plasma input models, which measure the radioactivity in the whole blood/plasma from blood samples collected during the PET scan, and *(ii)* reference tissue models, which compare the radioactivity in the target and reference region.

(i) Plasma input models represent the gold standard method since they incorporate the radioligand distribution over time in the plasma in the form of an arterial input function.

(ii) Reference tissue models are a non-invasive alternative method based on the assumption that a reference region devoid of specific binding exists from which an indirect input function is derived. These are mainly used in PET imaging of receptor function. One assumption common to all reference tissue models is that the ratio of the rate constants $K1$ and $k2$ is the same in all studied regions:

$$\frac{K_1}{k_2} = \frac{K_1'}{k_2'} \quad [4]$$

Where K_1' and k_2' are used to describe the rate constants in the reference tissue [154].

Therefore, reference tissue models can be used to derive the binding parameters from a reference region without the use of an arterial input function [174].

A simplified reference tissue model (SRTM), which assumes that the tracer can be represented by 1TCM in both the ROIs and the reference region, was initially developed for [^{11}C]RAC data quantification, and has now become widely used for the analysis of reversibly binding neuroreceptor tracers. Using SRTM it is possible to estimate micro- ($K_1 - k_2$) or macroparameters (V_T) by non-linear curve fitting. SRTM reduces the number of fit parameters from four to three, generating good fits to the kinetic data and a stable parameter estimation process [175-179].

1.6.2.2 Graphical analyses

Graphical methods do not estimate the system kinetics. Instead, the data are converted into a line plot which slope has a physiological meaning. The slope equals the V_T for each ROI, with higher slopes corresponding to higher binding potential (BP) defined as the ratio of the receptor's total concentration in the tissue (B_{max}) and the radioligand dissociation constant at equilibrium (K_D):

$$BP = \frac{B_{max}}{K_D} \quad [5]$$

B_{max} is referred to as B_{avail} since not all the existing receptors are available for the radioligand to bind, due to the occupancy by endogenous molecules.

When the radioligand specific binding is not compared to plasma concentrations but to a reference region with unspecific binding, the BP is defined as non-displaceable BP_{ND}. BP_{ND} can be derived from the V_T values in the target region and region devoid of specific binding (V_{ND}) [154]:

$$BP_{ND} = \frac{V_T - V_{ND}}{V_{ND}} = \frac{V_T}{V_{ND}} - 1 \quad [6]$$

Where $\frac{V_T}{V_{ND}}$ is often termed as distribution volume ratio (DVR):

$$BP_{ND} = DVR - 1 \quad [7]$$

Among the graphical analysis, the Logan plot is widely used for reversibly binding neuroreceptor tracers. Although, using the Logan plot one can estimate only macroparameters (BP_{ND}, V_T), the algorithm shows several advantages. Indeed, only two free parameters need to be estimated by regression, which can be obtained from a one-step procedure rather than from iterative fitting. Therefore, it shows fast computational time and independence from a kinetic model [180].

1.6.3 Properties of a successful brain PET ligand

Compared to therapeutics, a brain PET tracer has more rigorous criteria in terms of potency (single-digit nM or sub-nM) and pharmacokinetic (low or no radiometabolites' formation and low non-specific binding). Therefore, PET radioligand development is a challenging process requiring the intersection of multiple properties. Most important properties of a successful brain PET tracer have been exhaustively described elsewhere [181] and are summarized below:

1. Carbon-11/fluorine-18-labeling site

An essential criterion is a chemical structure with an accessible labeling site for the incorporation of short-lived radionuclides such as [^{11}C] ($t_{1/2}$ = 20.4 min) or [^{18}F] ($t_{1/2}$ = 109.7 min).

2. Sufficient blood-brain barrier penetration

A suitable brain PET tracer must also penetrate the BBB sufficiently to produce good brain uptake. Limited radioligand uptake can lead to a weak PET signal, masked by the signal of the background noise. This is especially crucial in brain imaging studies, where the vascular signal, about 3% in the rat brain [182], can substantially lead to uptake overestimation. A good radioligand should have a SUV > 1.5. The ability of a radioligand to penetrate the BBB relies on its size and charge, lipophilicity, plasma protein binding, and dependency on efflux pumps transport. The lipophilicity is expressed in Log*P* values, being *P* the n-octanol/water partition coefficient of the unionized species. High Log*P* values indicate high lipophilicity and vice versa. However, a radiotracer with high lipophilicity might become extensively bound to blood proteins, reducing the quote freely available in plasma to cross the BBB. High Log*P* values also lead to enhanced radiotracer non-specific binding to the white matter (composed mainly

of the lipid-rich myelin), producing a high background signal. Thereby, radioligands' Log*P* value must be in the range 1 – 3. The corresponding distribution coefficient at physiological pH is termed Log$D_{7.4.}$ In general, radiotracers with moderate lipophilicity, Log$D_{7.4}$ values between 2.0 – 3.5, show optimal BBB entry *in vivo* [13].

Further, the tracer should not be a substrate of the efflux pumps at the BBB. The strong efflux transport, mainly mediated by the P-glycoprotein (PgP) [183, 184], is among the main factors hindering the radioligand brain uptake [185]. PgP is an ATP-dependent transmembrane glycoprotein expressed at the luminal side of endothelial cells of blood capillaries. It actively transports certain lipophilic substrates back to the vascular space, thus impeding their access to the brain [186]. Interestingly, interspecies variations of PgP expression have been reported and could explain the observed divergences in terms of radioligand brain uptake between rodents and humans [187, 188]. For example, the radioligand for the serotonin receptors [^{11}C]RWAY is a strong substrate of PgP in rats, but not in non-human primates, where it shows acceptable brain accumulation (SUV > 2) [189, 190]. Along with the interspecies variability, PgP intraindividual differences exist, e.g., rats display 2-fold higher PgP expression in the cerebellum than other brain regions [191]. PgP inhibitors, such as Elacridar, can be administered to suppress PgP mediated efflux and increase the radioligand brain uptake [192, 193].

3. Appropriate pharmacokinetics

A successful radioligand must hold brain pharmacokinetics suitable to the isotope half-life. It must show fast kinetics to reach and bind its target site while clearing from the brain with low non-specific binding ($t_{1/2}$ < 30 min).

4. High specificity and selectivity

The radioligand must have high selectivity for the target compared to similar molecules. Ideally 30 – 100-fold higher, as defined by its equilibrium dissociation constant (K_d). Further, it should have high affinity for the intended target (in the single digit nanomolar range), expressed as the reciprocal value of the K_d ($1/K_d$).

5. High SNR

The binding affinity required to make a successful ligand is dependent on the number of binding sites for the radiotracer in a VOI (B_{max}). If B_{max} is high, a lower K_d is required to produce an adequate SNR. However, if the binding affinity is too high, equilibrium might not be reached on the timescale of *in vivo* imaging, making reliable quantification difficult. A ratio of $B_{max}/K_d \geq 10$ is considered good [194, 195]. Target density in the brain might be significantly different among species. For example, the noradrenaline transporters binding sites are 7 times more expressed in the rat brain than in non-human primates. Despite the promising rat imaging data, these interspecies differences precluded using the SPECT tracer [^{123}I]NKJ64 in humans [196-199].

6. Lack of radiometabolites crossing the blood-brain barrier

As part of the elimination process, radioligands are metabolized into more hydrophilic molecules by enzymes in the liver. Radiometabolites must not penetrate the BBB, as they cannot be distinguished from the signal produced by the parent radiotracer. When this happens, it leads to bias in the PET data quantification, as for the DAT tracer [^{11}C]PE2I. [^{11}C]PE2I is metabolized in rats and humans in a compound crossing the BBB and binding to DAT [200, 201]. Instead, the [^{18}F]SP203 tracer for the metabotropic type 5 glutamate receptor is metabolized in rats but not in humans [202, 203].

Typically, most radioligands showing favourable *in vitro* properties fail when translated into clinics, as they do not possess one or all the criteria mentioned above. In addition, even if successful in one species, they may not work in others. Recently developed methods can better approximate the radioligand *in vivo* performances. For example, plasma and brain unbound fractions can be measured to extract the percentage of compound free to cross the BBB, thus available for the target (ideal unbound fraction > 10% plasma, > 1% brain) [204, 205]. Further, *in vitro* metabolism studies can be combined with high performance liquid chromatography (HPLC) and mass spectrometry to mimic the *in vivo* condition [206].

1.6.4 PET reporter gene imaging

Novel radioligands, used to image engineered cells, have been developed to offer a deeper understanding of the molecular basis of pathogenesis in animal models of disease and monitor the gene therapy efficacy in humans [207-209]. Recently, they have been used for neuronal tracking and to manipulate brain protein expression [210]. These PET probes allow the direct detection of genetically engineered cells when the reporter gene encodes *(i)* an enzyme catalysing the transformation of the PET substrate to products trapped within cells or *(ii)* a receptor that is a target for the tracer [39, 211-213]. Exemplary brain reporter genes and their advantages and disadvantages are reported below.

1.6.4.1 HSV1-tk

The herpes simplex virus type 1 thymidine kinase (HSV1-tk) has been the most exploited enzyme-based reporter gene. It phosphorylates selectively specific radiolabeled substrates, which are then trapped in the cell [214]. Its ectopic expression may trigger immunogenic responses, leading to cell death or reduced reporter gene expression over time. Further, because currently, available tk substrates do not cross the BBB, HSV1-tk cannot be used to image reporter gene expression in the intact brain. Nevertheless, it is used as reporter gene or therapeutic in pathological conditions where the brain permeability is compromised, e.g., glioblastoma [37].

1.6.4.2 D2R80A

When DA binds to D2R, it evokes a decrease in the cellular cyclic AMP levels. A mutant form of D2R, D2R80A, has been developed to suppress this intracellular signaling path. D2R80A can be used as an imaging or therapeutic probe in neurodegenerative diseases involving D2R replacement therapy. However, the system suffers from high background signals in D2R-rich brain regions, such as the striatum [37-40].

1.6.4.3 hCB_2

The mutant form of the human type 2 cannabinoid receptor (hCB_2) and its PET ligand have been validated *in vitro* and *in vivo* in several species, showing good BBB penetration and reversible and specific CB_2 binding *in vivo*. CB_2 is poorly

expressed in the brain and only in the cerebellum and pons in physiologic conditions. However, it is upregulated by activated microglia during inflammation, an essential feature of neurological disorders. Its use is therefore compromised in these conditions [41-43].

1.6.4.4 PKM2

PKM2 is an isoform of pyruvate kinase (PK) involved in glycolysis, modulating metabolic processes, and cell proliferation [215-217]. PKM2 protein is upregulated in diseases like tumors or heart disorders [218, 219]. Instead, low expression levels are found in the healthy and diseased brain, which allows for high brain SNR [220]. Nevertheless, PKM2 seems to be involved in inflammatory responses, essential features of neurological disorders. Its use is therefore compromised in these conditions [221].

1.6.4.5 EcDHFR

The enzyme *Ec*DHFR converts dihydrofolate into tetrahydrofolate and is specifically antagonized by TMP. TMP is an antibiotic approved for clinical use, which crosses the BBB when given orally. This peculiarity has been successfully exploited to regulate the expression of proteins in the rat brain [44-46]. Most importantly, TMP shows very low affinity to the mammalian DHFR (4-fold less), producing a small background signal [222]. Alike TMP, its radiochemical analogs, [^{11}C]TMP, [^{18}F]TMP, and [^{18}F]FE-TMP, bind to *Ec*DHFR-engineered cells *in vitro* and *in vivo* [47, 210, 223, 224]. In 2021 Shimojo *et al*., reported, after completion of our study, the applicability of radiolabeled and fluorescent TMP derivatives for neuronal tracking, brain circuits imaging, and protein expression manipulation [210]. However, they observed very low brain uptake in the mouse and non-human primate brain (SUV ~ 0.15), and dependence on PgP efflux transport in the mouse brain [210].

1.7. Brain functional connectivity

"The brain is a network of spatially distributed but functionally and structurally interconnected regions that exhibit correlated activity over time. They communicate with each other via highly specialized neuronal connections and

are organized in neuronal circuits and networks. Understanding how functional connections between regions are arranged in the healthy and diseased brain is therefore of great interest" [1]. Brain regions are defined functionally connected if they engage in the same brain function, even though they are anatomically separated [225, 226]. Importantly, functionally connected areas show coherent activity patterns even at rest, in the absence of external stimuli [227, 228]. When acquired at rest, the generated readout is called resting-state (rs)-FC [229]. fMRI can be used to delineate the level of FC at high spatial and temporal resolutions based on spontaneous fluctuations of the BOLD signal, which indirectly detects neuronal activity via hemodynamic coupling [28]. Neurons lack reservoirs of glucose or oxygen. When engaged in a certain activity, they are provided with more energy by the adjacent capillaries through a process termed hemodynamic response, which supplies them with increased regional cerebral blood flow and oxygen [230, 231]. This leads to a change in the levels of deoxygenated (paramagnetic) and oxygenated (diamagnetic) hemoglobin that can be detected by BOLD-fMRI. Ultimately, the generated BOLD contrast is a complex response, dependent not only on blood oxygenation but also on cerebral blood flow and volume [232, 233].

The fluctuations of the BOLD signal, reflecting the spontaneous fluctuations of the underlying neurons [29], can be measured to derive the brain FC. Applying a seed-based approach to the BOLD-fMRI data, the FC is calculated as the temporal correlation between the BOLD signals extracted from the ROIs, using Pearson's correlation coefficient. Using this method, the overall brain connectivity can be visualized with a connectivity matrix, showing the strength of all connections between seed regions within the brain (Figure 9). Yet, the seed-based analysis is vulnerable to bias, as the seed needs to be determined a priori.

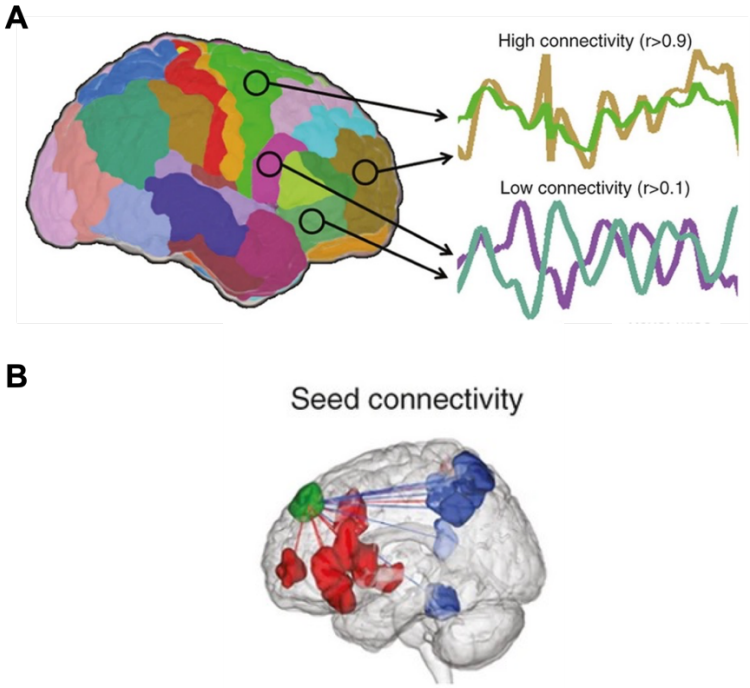

Figure 9: Brain FC. A: BOLD signals are extracted from pre-defined ROIs and their temporal fluctuations are correlated pair-wise. B: Using a seed-based approach, the FC of the predefined seed (green) and each voxel of the brain is computed. Figure courtesy of Tudor Mihai Ionescu.

Using rs-fMRI several brain rs-networks have been identified, such as the default mode and sensorimotor networks (DMN, SMN). The DMN comprises cortical regions and is associated with ideation and mind wandering [234, 235]. The SMN, instead, is involved in sensory processing and motor function and comprises the striatum, thalamus, and somatosensory and motor cortices [228, 236-242]. Alterations of these networks are linked to neurological diseases, and may serve as early therapeutic and diagnostic biomarkers [243, 244].

1.8. Scientific question

1.8.1 Imaging endogenous gene expression changes in the rat brain

"Receptors, transporters and ion channels are important targets for therapy development in neurological diseases [...] but their mechanistic role in pathogenesis is often poorly understood" [1]. Gene-editing and *in vivo* imaging approaches will help to identify the molecular and functional role of these targets and the consequences of their regional dysfunction on whole-brain level.

We combine CRISPR/Cas9 gene-editing with *in vivo* PET and PET/BOLD-fMRI to investigate the direct link between genes, molecules, and the brain connectome. *"The extensive knowledge of the Slc18a2 gene encoding the VMAT2, involved in the storage and release of DA, makes it an excellent target for studying the gene-networks relationships"* [1].

In this doctoral thesis we intended to address the following question: Can *in vivo* molecular and functional imaging be coupled to CRISPR/Cas9 gene-editing to investigate the gene-molecules-networks brain dynamics non-invasively and over time?

The specific aims of the study were:

- Knock down the *Slc18a2* gene in primary neurons and validate the CRISPR/SaCas9-induced KD efficiency on a protein and DNA level.
- Knock down the *Slc18a2* gene in the rat SNc and evaluate the CRISPR/SaCas9-induced VMAT2 KD efficiency and the downstream molecular and motor changes *in vivo* with PET imaging, behavioral analysis, and *ex vivo* through immunohistochemistry (IHC) and biochemistry.
- Knock down the *Slc18a2* gene in the rat SNc and evaluate *in vivo* the CRISPR/SaCas9-mediated VMAT2 KD efficiency, the functional adaptations in the DMN and SMN, and the underlying molecular changes with PET/BOLD-fMRI.

1.8.2 Imaging exogenous gene expression in the rat brain

In vivo imaging with PET reporter probes enables the quantification of the expression of ectopic genes, e.g., CRISPR components, in the brain of experimental animal models. However, until today no PET reporter gene for the *in vivo* quantification in the brain has been identified. Previous experiments in xenografted tumors have shown the potential of [^{11}C]TMP, binding to *Ec*DHFR, as PET reporter probe. Indeed, [^{11}C]TMP shows very low affinity to the mammalian DHFR (4-fold less) and is biologically inert [47].

The specific aim of the second part of this doctoral thesis was to investigate the brain pharmacokinetics and biodistribution of the previously published PET tracer [^{11}C]TMP targeting the reporter gene *Ec*DHFR for *in vivo* imaging in the rat brain.

2. Materials and Methods

2.1. Imaging endogenous gene expression changes in the rat brain

2.1.1 *In vitro* validation of the CRISPR/SaCas9-induced *Slc18a2* KD

2.1.1.1 Experimental design

"SgRNAs targeting the second exon of the Slc18a2 gene and the first exon of the lacZ gene were designed based on the PAM sequence of SaCas9 (NNGRRT) (Table 2). [...] Primary neurons were dissected from the rat cortices and transduced with AAVs. Seven days post-transduction, the protein expression level and mutation rate of the harvested genomic DNA were inspected by immunofluorescence and surveyor assay" [1] (Figure 10).

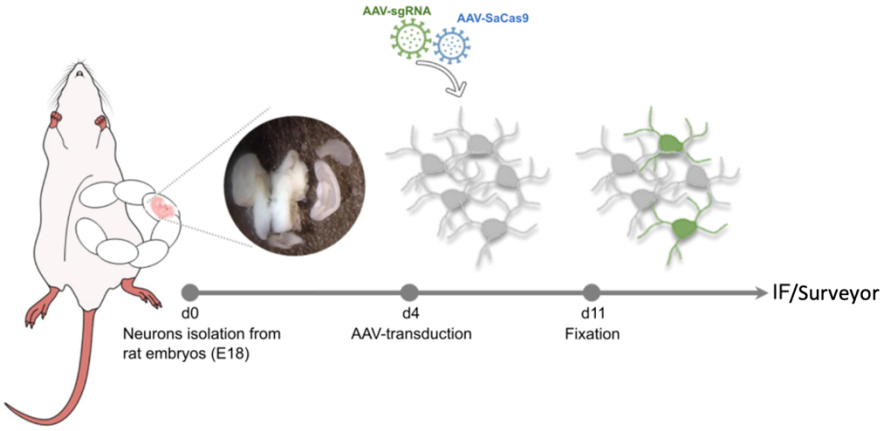

Figure 10: Experimental design of the *in vitro* validation. Primary neurons were dissected from the cortices of embryos at embryonic day 18 (E18). AAVs transduction was performed after 4 days. One-week post-transduction, the neurons were processed for immunofluorescence (IF) and Surveyor assay to evaluate the KD efficiency on protein and DNA level, respectively. Figure adapted from [1].

Table 2: SgRNAs sequences. sgRNAs targeting the *Slc18a2* and *LacZ* genes. Table from [1].

SgRNAs	DNA Target Sequences 5'- 3'	PAM (NNGRRT) 5'- 3'
Slc18a2	CGATGAACAGGATCAGTTTGC	GCGAGT
lacZ	CCTTCCCAACAGTTGCGCAGC	CTGAAT

2.1.1.2 Viral vectors

"SgRNAs were cloned into an AAV-PHP.EB expression vector containing a GFP reporter sequence, driven by the CMV promoter, for the identification of transduced neurons. A second AAV-PHP.EB construct was produced to express

SaCas9, flanked by two nuclear localization sequences (NLS) to allow its translocation into the nuclei. The vector expressed the nuclease via the CAG promoter and contains three HA-tags to visualize the targeted neurons (Figure 11). Cloning of the sgRNAs, plasmid construction, as well as the production of concentrated and purified AAV-PHP.EB vectors, delivered at a concentration of 10^{13} gc/mL, were carried by SignaGen Laboratories (Johns Hopkins University, USA). [...] The genomic mutation rate was assessed using a different set of AAVs with AAV2/1 serotype, for a conditional design, kindly provided by Matthias Heidenreich (prev. Zhang lab, Broad Institute of MIT and Harvard, Cambridge, USA)" [1].

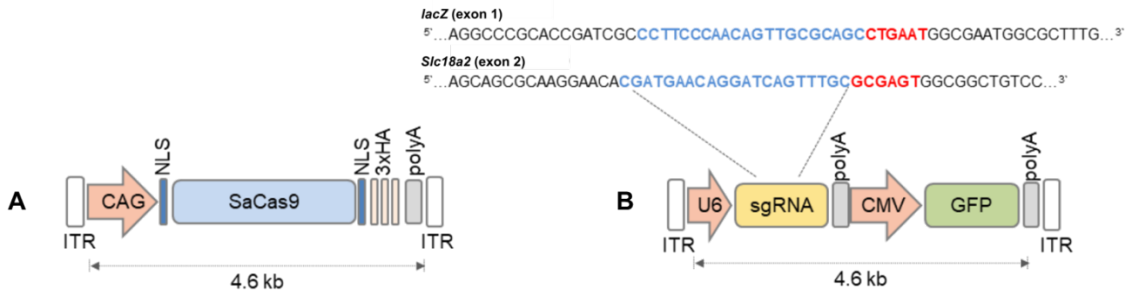

Figure 11: Plasmids. A: The SaCas9 sequence is flanked by two NLS to allow its translocation into the nuclei and is expressed under the control of the CAG promoter. The construct contains three HA-tags for the identification of transduced neurons. B: Plasmid expressing the sgRNA targeting the*Slc18a2* gene (KD) under the U6 promoter or the sgRNA targeting the bacterial *lacZ gene* (control). The vector expresses GFP via the CMV promoter, to allow the visualization of targeted neurons. GFP: green fluorescent protein, CMV: cytomegalovirus, NLS: nuclear localization sequence, CAG: CMV enhancer/chicken ß-actin, HA: hemagglutinin. Figure adapted from [1].

2.1.1.3 Animals

Wild-type Sprague Dawley (SD) pregnant rats were purchased from Charles River Laboratories (Sulzfeld, Germany) and delivered at embryonic day 17. Rats were kept on a 12 h day-night cycle at a room temperature of 22 °C and 40 – 60% humidity. Animals received a standard diet and tap water ad libitum before and during the experimental period. All animal experiments were performed according to the German Animal Welfare Act and were approved by the local ethical authorities, Regierungspräsidium Tübingen, permit number R15/19M.

2.1.1.4 Culture and transduction of rat primary neurons

"Primary cortical neurons were obtained from rat embryos of a pregnant SD rat from embryonic day 18 (E18) (Charles River, Sulzfeld, Germany). Embryos were decapitated and quickly removed from the mother rat. Cortical dissection was performed in ice-cold HBSS (100 mL 10 × HBSS, 870 mL dH_2O, 3.3% 0.3 M HEPES pH 7.3 and 1% pen/strep) (LifeTechnologies, Massachusetts, USA). The obtained tissue was washed three times with 10 mL ice-cold HBSS PhenolRed-free (LifeTechnologies, Massachusetts, USA) and then digested at 37 °C for 20 min in 8 mL HBSS with 2.5% trypsin (LifeTechnologies, Massachusetts, USA). Cortices were washed 3 times with 10 mL HBSS containing 3.7% FBS, and then gently triturated in 2 mL HBSS. For the maintenance, neurons were plated on poly-D-lysine-coated 24 well plates (BD Biosciences, Heidelberg, Germany) or coverslips (Neuvitro Corporation, Vancouver, USA) at a density of 16 × 10^4/well, and cultured in Neurobasal media supplemented with 2% 1 × B27, 0.25% Glutamax, 0.125% Glutamate and 1% pen/strep (LifeTechnologies, Massachusetts, USA) for four days. Afterward, AAVs carrying the expression of the vectors for the SaCas9 and sgRNAs (1:1 ratio), were added to the culture medium at 200,000 MOI (AAV-PHP.EB-sgRNA-lacZ: 1.7 × 10^{12} gc/mL, AVV-PHP.EB-SaCas9: 1.4 × 10^{12} gc/mL, AAV-PHP.EB-sgRNA-Slc18a2: 2.1 × 10^{12} gc/mL, final viral volume 37.5 µL/well). For the Surveyor assay, conditional AAVs for SaCas9, sgRNA-Slc18a2, Cre-recombinase (AAV2/1, 1:1:0.5 ratio) were used. Neurons were processed one-week post-viral treatment" [1].

2.1.1.5 Immunofluorescence

"Rat primary neurons were processed one-week post-AAV-transduction. Coverslips were washed twice with DPBS and fixed in 4% paraformaldehyde (PFA) in DPBS for 15 min at RT. Blocking and permeabilization were performed for 30 min at RT in DPBS with 5% donkey serum, 0.5% Triton-X100, and 0.05% BSA. Primary antibody incubation (VMAT2, 1:50, EB06558, Everest Biotech, Ramona, USA) was performed for 60 min at RT. The immunofluorescent signal was detected using Cy3 conjugate secondary ab (1:250, Vector Laboratories Ltd., Peterborough, UK, kindly provided from Birgit Fehrenbacher, Department of

Dermatology, University of Tübingen, Germany). Coverslips were mounted using ProLong Antifade Diamond Medium containing DAPI (LifeTechnologies, Massachusetts, USA) and imaged with a TCS-SP2/Leica DM IRE2 confocal laser scanning microscope. Images were processed with Leica Confocal Software LCS (Version 2.61) (original magnification 630) (Leica Microsystems, Wetzlar, Germany)" [1].

2.1.1.6 Surveyor assay

"The presence of genetic deletions was evaluated in rat primary neurons with the Surveyor assay (Surveyor kit, Integrated DNA Technologies, Coralville, USA). [...] Following the viral infection, the genomic DNA was extracted using the QuickExtract DNA Extraction solution (Epicentre, Madison, USA), according to the manufacturer´s instructions, and was normalized to 100 ng in dH_2O. 18 – 25 nt primers were designed 200 – 400 bp away from either side of the SaCas9 target site to amplify the loci of interest by touchdown PCR (primers are provided in Table 3). DNA amplification was performed using 0.5 µL Phusion Polymerase (LifeTechologies, Massachusetts, USA), as previously reported [104]. A single band product was visualized on 1.5% agarose gel, isolated and purified using QuiaQuick Spin columns (Qiagen, Hilden, Germany), following the supplier protocol. 400 ng of the purified PCR product were mixed with 2 µL Taq DNA polymerase buffer (LifeTechnologies, Massachusetts, US) to allow the cross-annealing of the mutated and wild-type sequences. The re-annealing process was conducted at the following cycling conditions: 10 min at 95 °C, 95 °C to 85 °C at -2 °C/s, hold 1 min, ramp down to 75 °C at -0.3 °C/s, hold 1 min, and so on until 4 °C temperature was reached. This cross-annealing procedure converts the mutations into mismatch duplexes (heteroduplexes), which can be recognized performing a nuclease digestion [245]. The annealed products were digested for 20 min at 42 °C using 2.5 µL $MgCl_2$ (0.15 M), 1 µL Surveyor nuclease, and 1 µL Surveyor enhancer. Products were then resolved on a 2.5% agarose gel, stained with 1% SYBR Gold DNA (LifeTechnologies, Massachusetts, USA) in 1% TBE buffer. The size of the occurring bands indicated the location of the mutation (expected DNA fragments sizes are provided in Table 3).

To quantify the KD efficiency, the software ImageJ was used (U. S. National Institutes of Health, Bethesda, Maryland, USA). Peak areas of the bands visualized on agarose gel were selected and the percentages of the transduced neurons acquiring the editing (%) was calculated using the following formula [104]:

$$Editing(\%) = 100 \times \left(1 - \sqrt{\left(1 - \frac{b+c}{a+b+c}\right)}\right) \quad [8]$$

where a is the integrated intensity of the undigested PCR product and b, and c are the integrated intensities of each cleavage product" [1].

Table 3: Primers sequences. Selected primers used to amplify the *Slc18a2* and the *lacZ* loci for the Surveyor assay and DNA expected fragments sizes (bp). Table from [1].

SgRNAs	Forward Primer 5'- 3'	Reverse Primer 5'- 3'	Fragment size (bp)
Slc18a2	CTTGGGGATCCTCTAAGGCAG	TACAGCGCGGTTCTTCAACT	313_280
lacZ	GTCGTGACTGGGAAAACCCT	TTGTTCCCACGGAGAATCCG	200_80

2.1.2 *In vivo* evaluation of the CRISPR/SaCas9-induced Slc18a2 KD and downstream molecular changes

2.1.2.1 Experimental design

Wild-type Long-Evans (LE) rats were injected with AAV-PHP.EB vectors into the right SNc and were divided into two groups. Control rats were injected with AAV-PHP.EB-sgRNA-lacZ and AVV-PHP.EB-SaCas9. KD rats were injected with AAV-PHP.EB-sgRNA-Slc18a2 and AVV-PHP.EB-SaCas9. DPBS was injected into the contralateral side as sham. Afterwards, *in vivo* PET scans with imaging markers of VMAT2 expression, DA availability, nerve terminal integrity and inflammatory responses were performed in KD and control rats using respectively [^{11}C]DTBZ (8 – 10 weeks post-injection), [^{11}C]methylphenidate (MP) (10 – 12 weeks post-injection), [^{11}C]RAC (12 – 14 weeks post-injection) and [^{18}F]GE-180 (14 – 16 weeks post-injection). Starting 10 weeks after CRISPR/Cas9 targeting, motor consequences of the CRISPR/SaCas9-induced VMAT2 KD were explored by several behavioral tasks. 19 weeks post-injection, biochemical and histological analyses were performed to corroborate the *in vivo* findings (Figure 12).

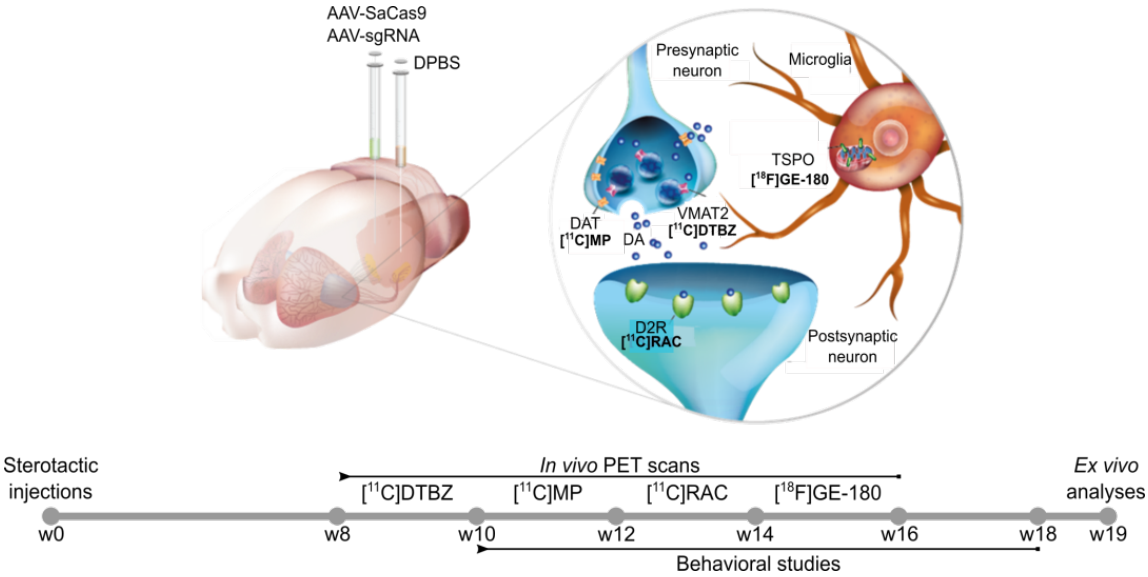

Figure 12: Experimental design of the *in vivo* study. AAV-PHP.EB for SaCas9 and sgRNA-*Slc18a2* (KD) or sgRNA-*lacZ* (control) were injected into the right SNc of wild-type LE rats. DPBS was injected into the contralateral SNc. Starting 8 weeks after AAVs delivery, VMAT2 expression, DAT availability, postsynaptic changes, and inflammatory responses were quantified using dynamic PET imaging with [^{11}C]DTBZ, [^{11}C]MP, [^{11}C]RAC, and [^{18}F]GE-180, respectively. Motor consequences of the KD were investigated with behavioral tests. *Ex vivo* analyses were performed to corroborate the *in vivo* data. Figure adapted from [1].

2.1.2.2 Animals

"Wild-type LE rats (f, 7 – 8 weeks, 202 ± 17 g, n= 24) were purchased from Charles River Laboratories (Sulzfeld, Germany). Rats were kept on a 12 h day-night cycle at a room temperature of 22 °C and 40 – 60% humidity. Animals received a standard diet and tap water ad libitum before and during the experimental period. All animal experiments were performed according to the German Animal Welfare Act and were approved by the local ethical authorities, permit number R4/20G" [1].

2.1.2.3 Stereotactic injections

"Rats were anesthetized by injecting a mixture (1 mL/kg) of fentanyl (0.005 mg/kg), midazolam (2 mg/kg,) and medetomidine (0.15 mg/kg) intraperitoneally and were placed onto a stereotactic frame (Harvard Apparatus, Holliston, MA, USA) with the skull flat between Lambda and Bregma. The following coordinates were used for the injections (flat skull position): AP: - 5 mm, ML: ± 2 mm, DV: - 7.2 mm, below the dural surface as calculated relative to Bregma. Rats were injected with 3 µL AAVs into the right SNc and were divided

into two groups. Control rats (n= 10) were injected with AAV-PHP.EB-sgRNA-lacZ (1.7 × 10^{12}gc/mL) and AVV-PHP.EB-SaCas9 (1.4 × 10^{12} gc/mL) (1:1 ratio). VMAT2 KD rats (n= 14) were injected with AAV-PHP.EB-sgRNA-Slc18a2 (2.1 × 10^{12} gc/mL) and AVV-PHP.EB-SaCas9 (1.4 × 10^{12} gc/mL) (1:1 ratio) (see AAVs in Figure 10). DPBS (3 µL) was sham-injected into the contralateral SNc. Solutions were infused at a rate of 0.2 µL/min using a 5 µL Hamilton syringe (Hamilton, Bonaduz, Switzerland) and an automated microsyringe pump (Harvard Apparatus, Holliston, MA, USA). To allow for the diffusion of AAVs into the tissue, the needle was left in place for 10 min, and then slowly retracted at 0.2 mm/min. After the surgery, an antidote containing atipamezole (0.75 mg/kg) and flumazenil (0.2 mg/kg) was injected subcutaneously (s.c.). The rats were kept warm in their cages until fully recovered" [1].

2.1.2.4 *In vivo* PET imaging and data analysis

"Three small-animal PET scanners (Inveon, Siemens, Erlangen, Germany) and dedicated rat brain beds (Jomatik Gmbh, Tuebingen, Germany) with stereotactic holders and temperature feedback control units (Medres, Cologne, Germany) were used. These ensured the delivery and removal of the anesthesia gas and stabilized the body temperature at 37 °C during the PET data acquisition. Anesthesia was induced by placing the animals in knock-out boxes and delivering 2% isoflurane in oxygen air. Subsequently, a 24 G catheter (BD Insyte, NJ, USA) was placed into the tail vein for the tracer administration. [...] The rats were placed in the center of the FOV and PET acquisitions started 5 s before the bolus injection of the tracer. The list-mode data from the dynamic acquisitions of [^{11}C]DTBZ, [^{11}C]RAC and [^{11}C]MP were histogrammed into 39 time-frames (12×5 s, 6×10 s, 6×30 s, 5×60 s, 10×300 s), from [^{18}F]GE-180 into 16 time-frames (5×60 s, 5×120 s, 3×300 s, 3×600 s). PET scans were reconstructed using the OSEM3D map algorithm, and a matrix size of 256 × 256 × 159, resulting in a pixel size of 0.38 × 0.38 × 0.79 mm.

Data preprocessing analysis was performed with Matlab (Mathworks, Natick, MA, USA), Statistical Parametric Mapping 12 (SPM12, Wellcome Trust Centre for Neuroimaging, University College London, England), and the QModeling toolbox

[246]. First, realignment of all frames was performed using SPM12 and average images were generated for every scan. The mean images were then used for coregistration to the Schiffer rat brain atlas provided by PMOD software [247].
To generate the respective TAC, VOIs were defined over the target and reference regions. VOIs were placed over the right and left striatum for [^{11}C]DTBZ, [^{11}C]RAC, and [^{11}C]MP. Cerebellum was used as reference region.
BP_{ND} for [^{11}C]DTBZ, [^{11}C]RAC and [^{11}C]MP were calculated over the all frames in the regions of interest with Logan reference [248], with a population average k2' retrieved from SRTM [176] ([^{11}C]DTBZ: 0.41 min^{-1}, [^{11}C]RAC: 0.34 min^{-1}, [^{11}C]MP: 0.18 min^{-1}). [^{11}C]DTBZ and [^{11}C]RAC binding changes (%), here expressed as ΔBP_{ND}, were calculated according to the formula:

$$\Delta BP_{ND} = 1 - \frac{BP_{ND}\ right\ striatum}{BP_{ND}\ left\ striatum} \times 100 \quad [9]$$

[^{18}F]GE-180 standard uptake in the right striatum was calculated over the interval between 30 – 60 min after scan start and normalized by the standard uptake calculated in the left (DPBS-injected) striatum over the same time interval.
QModeling was used to generate voxel-wise BP maps for [^{11}C]DTBZ, [^{11}C]RAC and [^{11}C]MP. [^{18}F]GE-180 average uptake images were generated with an in-house-written script in MATLAB" [1]. In Table 4 injected and molar activities at the time of injection are reported for each radioligand.

Table 4: Radioligands' injected molar activity. [^{11}C]DTBZ, [^{11}C]MP, [^{11}C]RAC, and [^{18}F]GE-180 injected and molar activity. Table from [1].

Radioligand	Injected Activity (Mean ± SD) MBq/Kg	Molar Activity (Mean ± SD) GBq/µmol
[^{11}C]DTBZ	25 ± 1	93 ± 35
[^{11}C]MP	25 ± 1	57 ± 14
[^{11}C]RAC	25 ± 1	88 ± 41
[^{18}F]GE-180	24 ± 3	576 ± 283

2.1.2.5 Data exclusion

"Four rats were excluded from the study because two rats from each cohort died during a PET acquisition. One additional control rat was excluded from the [^{11}C]MP analysis due to a poor SNR" [1].

2.1.2.6 Behavioral studies

2.1.2.6.1 Cylinder test

"Untrained rats were placed individually inside a glass cylinder (19 cm Ø, 20 cm height). The test started immediately, and lasted 5 min. During the test session rats were left undisturbed and were videotaped with a camera located at the bottom-center of the cylinder to allow a 360 ° angle view. Paw touches were analyzed using a slow-motion video player (VLC software, VideoLan). The number of wall touches, contacts with fully extended digits, was counted. Data were analyzed as follows" [1]:

$$contralateral\ paw\ touches\ (\%\ to\ total) = \frac{contralateral\ touches}{total\ touches} \times 100 \qquad [10]$$

2.1.2.6.2 Rotameter test

"Rotational asymmetry was assessed using an automated rotameter system composed of four hemispheres (TSE Systems GmBH, Bad Homburg, Germany) based on the design of Ungerstedt and Arbuthnott [249]. Rats were placed into an opaque half bowl (49 cm Ø; 44 cm height) and fixed to a moveable wire with a collar. The number of clockwise (CW) and counterclockwise (CCW) rotations (difference of 42.3° in their position) were automatically counted. Spontaneous rotation test lasted 5 min.

Apomorphine-evoked rotational asymmetry was evaluated for 60 min after s.c. administration of apomorphine hydrochloride (0.25 mg/kg) dissolved in physiological saline containing 0.1% ascorbic acid (Sigma Aldrich, St. Louis, Missouri, USA). Two priming injections of apomorphine (one week interval off-drug) were necessary to produce sensitization to the treatment. The program RotaMeter (TSE Systems GmBH, Bad Homburg, Germany) was used to acquire the data. Data were analyzed as follows" [1]:

$$\frac{turns}{min} = ccw\ rotation\ -\ cw\ rotations \qquad [11]$$

2.1.2.6.3 Beam walk test

"Rats were trained for 4 days to cross a built-in-house beam (1.7 cm width, 60 cm length, 40 cm height), and reach a cage with environmental enrichment. Rats had 5 trials to cross the beam with the reward resting time decreasing from 30 s to 10 s. On the test day (one week apart from the fourth day of training) rats were

videotaped. The acquired videos were analyzed using a slow-motion video player (VLC software, VideoLan) and the amount of footslips (falls) was counted. Data were analyzed as follows" [1]:

$$contralateral\ footslips\ (\%\ to\ total\ steps) = \frac{contralateral\ footslips}{total\ steps} \times 100 \qquad [12]$$

2.1.2.6.4 Open Field test

"Untrained rats were set in a rectangular box (TSE Systems GmBH, Bad Homburg, Germany) for 11 min (1 min habituation, 10 min test) to evaluate the spontaneous exploratory behavior. A frame with light sensors, as high as the animals' body center, was connected to a receiver box to record the rats' walked distance. The program ActiMod (TSE Systems GmBH, Bad Homburg, Germany) was used for the analysis and the experimental session was divided in 1 min time bins. Results were averaged from the total travelled distance over 10 min (mean ± SD)" [1].

2.1.2.6.5 Body weight gain

"Rats body weight was measured before (week 0) and 14 weeks after CRISPR/SaCas9 VMAT2 KD. Body weight gain was calculated as follows" [1]:

$$body\ weight\ gain\ (g) = \frac{weight\ at\ week\ 14 - weight\ at\ week\ 0}{weight\ at\ week\ 0} \times 100 \qquad [13]$$

2.1.3 *Ex vivo* evaluation of the CRISPR/SaCas9-induced *Slc18a2* KD

2.1.3.1 Immunohistochemistry

"Rats were sacrificed 19 weeks after viral vector injection via CO_2 inhalation followed by intracardial perfusion with heparinized DPBS (1:50 v/v, 100 mL). After decapitation, brains were rapidly removed and placed in a brain matrix on ice. The left and right striata were dissected, from 2 mm thick coronal sections, flash-frozen in liquid nitrogen, and stored at -80 °C until further analysis (biochemistry). The remaining tissue was fixed in 4% PFA for 48 h and then transferred to 20% sucrose solution for cryoprotection. Brains were cut into 35 µm thick coronal sections on a freezing microtome (Leica Biosystems, Wetzlar, Germany) and stored in anti-freeze solution (0.5 M phosphate buffer, 30% glycerol, 30% ethylene glycol) at -20 °C. Sections were collected in 12 equally

spaced series through the entire anterior-posterior extent of the SN and striatum and stored until further analysis. IHC was performed on free-floating sections. Sections were washed 3 times with TBS buffer and antigen retrieval was carried for 30 min at 80 °C in Tris/EDTA buffer. Afterward, pre-incubation in MeOH (10%) and H_2O_2 (3%) in TBS was performed for 30 min. Following the blocking in 5% normal goat serum in TBS-X (0.05%), primary antibody incubation was performed for 24 h at room temperature in 1% BSA in TBS-X (TH: 1:5000, P40101, Pel-freez, Arkansas, USA, VMAT2: 1:5000, 20042, Immunostar, Hudson, USA). The tissue was rinsed in TBS-X and reacted with the respective biotinylated secondary antibody (1:200, Vector Laboratories Ltd., Peterborough, UK) for 60 min at room temperature in 1% BSA in TBS-X. Staining was developed using 3,3'-diaminobenzidine (DAB Substrate Kit, Vector Laboratories Ltd., Peterborough, UK) and an immunoperoxidase system (Vectastain Elite ABC-Kit, Vector Laboratories Ltd., Peterborough, UK). Slices were rinsed, mounted onto chromalum gelatinized slides, dehydrated in ascending concentrations of alcohol and xylene baths, and coverslipped with DPX mounting medium (Sigma Aldrich, St. Louis, Missouri, USA)" [1].

2.1.3.2 Stereology

"Estimates of total numbers of TH+ cells in nigral sections were obtained with an unbiased stereological quantification method by employing the optical fractionator principle [250]. Brain sections from 5 rats (VMAT2 KD n= 2, Control n= 3) were excluded from the stereological analysis, due to weak TH immunoreactivity. First, 5x images were acquired with the automated Metafer slide scanning platform (MetaSystems, Altlußheim, Germany). Then, ROIs were drawn using the VSViewer program (Metasystems, Altlußheim, Germany), and a sampling fraction of 50% was defined. Afterwards, 63x images were acquired in an automated fashion based on the sampling fraction in a random orientation within the ROI. The acquired 63x images were imported into the VIS program and cell counting was performed with the CAST module (Visiopharm A/S, Hørsholm, Denmark, Version 2020.08.2.8800).

The number of cells estimates was obtained by applying the formula" [1]:

$$Total\ n\ of\ TH+\ cells = \sum \left(\frac{\text{Number of cells counted per brain}}{\text{Acquisition fraction x counting frame}} \right) \times n\ of\ series \quad [14]$$

2.1.3.3 Immunofluorescence

"Immunofluorescence was performed on SN sections (35 µm thick coronal sections), mounted onto chromalum gelatinized slides, dehydrated in ascending concentrations of alcohol and xylene baths. Sections were washed 3 times with KPBS buffer and antigen retrieval was carried for 30 min at 80 °C in Tris/EDTA buffer. Following blocking in 5% donkey serum and normal horse serum in KPBS-X (0.25%), primary antibody incubation was performed for 24 h at RT (VMAT2: 1:5000, 20042, Immunostar, Hudson, USA, HA-tag: 1:5000, MMS- 101R, Nordic BioSite, Taby, Sweden, GFP: 1:50.000, ab13970, Abcam, Cambridge, UK). The tissue was rinsed in KPBS-X and reacted with the respective fluorophore-conjugated secondary antibody (1:200, Vector Laboratories Ltd., Peterborough, UK) for 2 h in 0.2% KPBS-X. Slides were coverslipped with Vectashield mounting medium (Vector Laboratories Ltd., Peterborough, UK)" [1].

2.1.3.4 Biochemistry

"DA, DOPAC, HVA and 5-HT striatal levels were determined by HPLC. Brain samples from 5 rats (VMAT2 KD n= 3, Control n= 2) were excluded from the analysis as striatal sections did not fall in the selected range: 1.2 – 0.4 mm. Briefly, striatal brain lysates were injected by a cooled autosampler into an ESA Coulchem III coupled to a Decade Elite electrochemical detector (Antec Scientific, Zoeterwoude, The Netherlands) set to a potential of +350 mV. Separation was facilitated by using an Atlantis Premier BEH C18 AX column (Waters Corporation, Massachusetts, USA) and a dual mobile phase gradient of decreasing octane sulfonic acid (OSA) and increasing MeOH content (mobile phase A containing 100 mM PO_4-buffer pH 2.50 and 4.62 mM OSA and mobile phase B containing 100 mM PO_4-buffer pH 2.50 and 2.31 mM OSA), delivered at a flow rate of 0.35 mL/min to an Atlantis Premier BEH C18 column (particle size 2.5 µm, 2.1 mm x 150 mm) (Waters Corporation, Massachusetts, USA). Data was collected using the Chemstation software (Agilent, California, USA) and then exported to Chromeleon (LifeTechnologies, Massachusetts, USA) for data quality control, peak integration, and concentration calculations. Striatal metabolites'

content was expressed in nmol for each sample and normalized to total protein (mg). DA turnover rate was calculated according to the formula" [1]:

$$DA\ turnover\ rate = \frac{HVA+DOPAC}{DA} \quad [15]$$

2.1.4 *In vivo* evaluation of the CRISPR/SaCas9-induced *Slc18a2* KD and downstream functional connectivity changes

2.1.4.1 Experimental design

"Cylinder test and [^{11}C]RAC PET/fMRI scans were performed at baseline and after CRISPR/SaCas9-induced VMAT2 KD to inspect the motor changes (12 – 14 weeks post-injection) and functional connectivity adpatations (8 – 14 weeks post-injection). [...] Wild-type LE rats were injected with AAV-PHP.EB-sgRNA-Slc18a2 and AVV-PHP.EB-SaCas9. DPBS was injected into the contralateral side as sham. In vivo [^{11}C]DTBZ PET scans were performed to inspect the extent of the induced VMAT2 KD (8 – 10 weeks post-injection)" [1] (Figure 13).

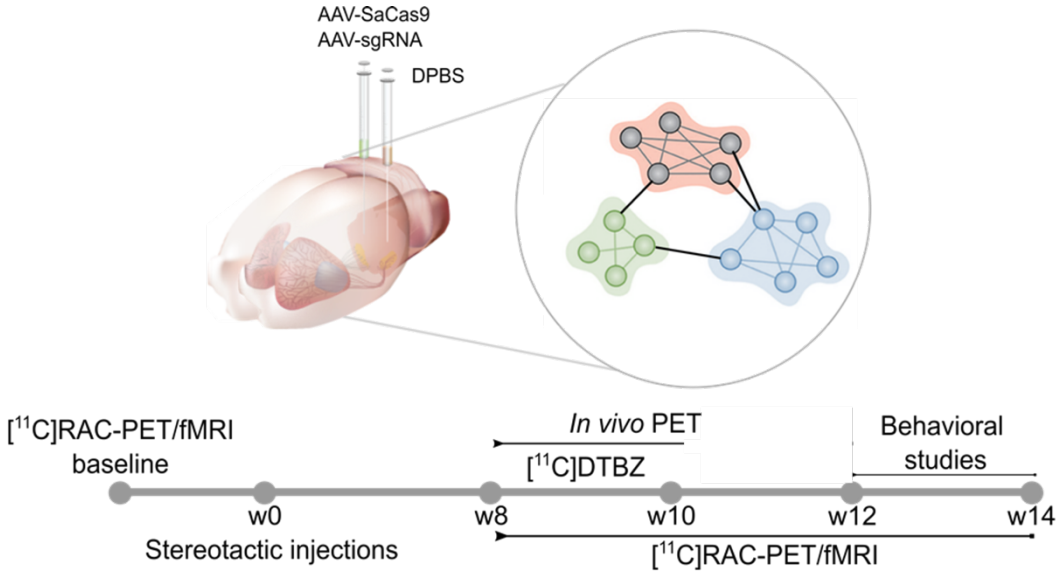

Figure 13: Experimental design of the *in vivo* PET/fMRI study. Cylinder test and [^{11}C]RAC PET/fMRI scans were performed at baseline. AAV-PHP.EB for SaCas9 and sgRNA-*Slc18a2* were injected into the right SNc of wild-type LE rats. DPBS was injected into the contralateral SNc. Starting 8 weeks after AAVs delivery, VMAT2 expression, postsynaptic changes, and functional connectivity adaptations were quantified using [^{11}C]DTBZ PET and symultaneous [^{11}C]RAC PET/fMR imaging. Motor consequences of the KD were investigated with cylinder test. Figure adapted from [1].

2.1.4.2 Animals

"Wild-type LE rats (f, 7 – 8 weeks, 202 ± 17 g, n= 33) were purchased from Charles River Laboratories (Sulzfeld, Germany). Rats were kept on a 12 h day-night cycle at a room temperature of 22 °C and 40 – 60% humidity. Animals received a standard diet and tap water ad libitum before and during the experimental period. All animal experiments were performed according to the German Animal Welfare Act and were approved by the local ethical authorities, permit number R4/20G" [1].

2.1.4.3 Stereotactic injections

See paragraph 2.1.2 3.

2.1.4.4 Simultaneous PET/fMRI and data analysis

"Rats (n=33) underwent longitudinal simultaneous [^{11}C]RAC-PET/ fMRI scans at baseline and 8 – 14 weeks after CRISPR/SaCas9-induced VMAT2 KD. [...] Animals received a medetomidine bolus injection (0.05 mg/kg) and the anesthesia was switched to constant medetomidine infusion (0.1 mg/kg/h), and 0.5% isoflurane in air during the scan time, as adapted from the literature [251]. Next, rats were placed onto a dedicated rat bed (Medres, Cologne, Germany) and a temperature feedback control unit (Medres, Cologne, Germany), ensuring the delivery and removal of the anesthesia gas and stabilizing the body temperature at 37 °C during the scan time. A breathing pad and a pulse oximeter were used to observe respiration and heart rates. Scans were acquired using a small-animal 7 T Clinscan MRI scanner, a 72 cm diameter linearly polarized RF coil (Bruker) for transmission, and a four-channel rat brain coil for reception (Bruker Biospin MRI, Ettlingen, Germany). Localizer scans were first acquired to accurately position the rat brains into the center of the PET/MRI FOV. Subsequently, local field homogeneity was optimized by measuring local magnetic field maps. Anatomical reference scans were performed using T2-weighted Turbo-RARE MRI sequences (TR: 1800 ms, TE: 67.11 ms, FOV: 40 x 32 x 32 mm, image size: 160 x 128 x 128 px, Rare factor: 28, averages: 1). Finally, T2-weighted gradient echo EPI sequences (TR: 2500 ms, TE: 18 ms, 0.25 mm isotropic resolution, FoV 25 x 23 mm, image size: 92 x 85 x 20 px, slice*

thickness 0.8 mm, slice separation 0.2 mm, 20 slices) were acquired for BOLD-fMRI.

A dedicated small-animal PET insert developed in cooperation with Bruker (Bruker Biospin MRI, Ettlingen, Germany) was used for the [^{11}C]RAC acquisitions, the second generation of a PET insert developed in-house with similar technical specifications [252]. [^{11}C]RAC was applied via a bolus injection. In Table 5 injected activities (MBq/kg) and molar activities (GBq/µmol) at the time of injection are reported. PET/fMRI acquisitions started simultaneously with the tracer injection and were performed over a period of 60 min. The list-mode files of the PET data were histogrammed into 14 time-frames (1x30 s, 5x60 s, 5x300 s, 3x600 s), the 30s between acquisition start and the injection were excluded from the analysis. Reconstruction was performed with an in-house-written OSEM2D algorithm. Data preprocessing and analysis were performed as described in paragraph 2.2.d). A population average k2' ([^{11}C]RAC t0: 0.20 min^{-1}, [^{11}C]RAC t8: 0.23 min^{-1}) was set for the Logan reference, and retrieved from SRTM [176, 248].

Preprocessing of the fMRI data was performed using a pipeline employing SPM12, Analysis of Functional NeuroImages (AFNI, National Institute of Mental Health (NIMH), Bethesda, Maryland, USA), and in-house-written scripts in MATLAB, as reported previously [253] .

RS-FC was calculated using a seed-based approach. To this extent, 20 regions were selected from the Schiffer rat brain atlas (a list of the regions is provided in Table 6). The SPM toolbox Marseille Boîte À Région d'Intérêt (MarsBaR) was employed to extract fMRI time-courses from all regions [254]. These were then used to calculate pairwise Pearson's r correlation coefficients for each dataset, generating correlation matrices containing 20 x 20 elements. Self-correlations were set to zero. The computed Pearson's r coefficients then underwent Fischer's transformation into z values for group-level analysis.

Several rs-FC metrics were computed on different regional levels to investigate the potential effects of DA depletion in the right striatum. Regional node strengths were computed as the sum of all correlations of one seed to the regions included in one network. Interregional node strengths were defined as the sum of the

correlations of one node to the regions of another network. Network strengths were defined as the sum of strengths of all correlations between regions belonging to a network. Internetwork strengths were calculated as the sum of all correlations between two sets of regions belonging to two networks [255]" [1].

Table 5: Radioligands' injected and molar activity. [^{11}C]DTBZ and [^{11}C]RAC injected and molar activity. Table from [1].

Radioligand	Injected Activity (Mean ± SD) MBq	Molar Activity (Mean ± SD) GBq/µmol
[^{11}C]RAC t0	27 ± 4	108 ± 49
[^{11}C]RAC t8	28 ± 1	115 ± 41
[^{11}C]DTBZ	27 ± 1	180 ± 48

Table 6: Rat brain atlas regions. Brain regions included in the Paxinos rat brain atlas, including their respective volumes and abbreviations. Table from [1].

Brain region (ROI)	Hemisphere	ROI volume [mm^3]	Abbreviation
Striatum	left	43.552	STR
	right		
Cingulate Cortex	left	14.480	CgC
	right		
Medial Prefrontal Cortex	left	6.304	mPFC
	right		
Motor Cortex	left	32.608	MC
	right		
Orbitofrontal Cortex	left	18.936	OFC
	right		
Parietal Cortex	left	7.632	PaC
	right		
Retrosplenial Cortex	left	18.920	RSC
	right		
Somatosensory Cortex	left	71.600	SC
	right		
Hippocampus	left	25.064	Hipp
	right		
Thalamus	left	30.712	Th
	right		

2.1.4.5 Behavioral studies

Cylinder test See paragraph 2.1.2.6.1

2.1.4.6 Data exclusion

"Three rats were excluded from the study due to aliasing artifacts, local distortion, and motion during the data acquisition. Seven rats died during a PET/BOLD-fMRI scan. The final cohort included n= 23 rats. One rat was excluded from the cylinder test analysis due to issues during video recording" [1].

2.2. Imaging exogenous gene expression changes in the rat brain

2.2.1 *In vivo* and *ex vivo* characterization of [^{11}C]TMP in the rat brain

2.2.1.1 Animals

Wild-type SD rats (f, 8 weeks, 263 ± 7 g, n= 9) were purchased from Charles River Laboratories (Sulzfeld, Germany). Rats were kept on a 12 h day-night cycle at a room temperature of 22 °C and 40 – 60% humidity. Animals received a standard diet and tap water ad libitum before and during the experimental period. All animal experiments were performed according to the German Animal Welfare Act and were approved by the local ethical authorities, Regierungspräsidium Tübingen, permit number R4/15.

2.2.1.2 *In vivo* PET imaging and data analysis

Inveon small-animal PET scanners (Siemens, Knoxville, TN, USA) and dedicated single rat beds (Jomatik Gmbh, Tuebingen, Germany), ensuring the delivery and removal of the anesthesia gas and stabilizing the animals' movements and body temperature (37 °C), were used. Rats (n= 9) were anesthetized with isoflurane (1.5%) vaporized in 1.0 L/min of oxygen gas and placed in the center FOV. 60 min dynamic PET acquisitions started 5 s prior to the bolus injection of the tracer. The list-mode data from the dynamic acquisitions were histogrammed into 39 time frames (12x5 s, 6x10 s, 6x30 s, 5x60 s, 10x300 s). Images were reconstructed using FBP algorithm and a matrix size of 256 x 256, resulting in a pixel size of 0.38 x 0.38 x 0.79 mm. Data analysis was performed with PMOD software 3.2. PET images (sum of the first 20 frames) were coregistered to the Schiffer rat brain atlas provided by PMOD software [247]. To generate the

respective TACs, VOIs were defined over the target and reference regions. TACs were extracted for each scan and expressed as SUV:

$$SUV = \frac{Radioactivity\ concentration}{Injected \frac{dose}{body\ weight}} \left[\frac{\frac{MBq}{mL}}{\frac{MBq}{Kg}}\right] \quad [16]$$

2.2.1.3 Sulfamethoxazole and Elacridar administration

Rats (n= 6) received a solution of Sulfamethoxazole (Sigma Aldrich, St. Louis, Missouri, USA) and [^{11}C]TMP (5:1 ratio) via tail vein catheter right before the start of the dynamic PET scans.

Elacridar (Sigma Aldrich, St. Louis, Missouri, USA) was freshly dissolved at a concentration of 5mg/Kg in an aqueous solution containing 10% dimethylacetamide, 40% PEG-800, and 30% hydroxypropyl-β-cyclodextrin and was injected *i.v.* (3 mL/Kg) 30 min before the start of the dynamic PET scans (n=6).

2.2.1.4 Biodistribution experiments

Rats (n=9) were injected with [^{11}C]TMP and were sacrificed via CO_2 inhalation 2 min (n=3), 15 min (n=3), and 45 min (n=3) post-injection. Kidneys, brain, and blood were collected at the three time points. Radioactivity concentration in the samples was measured in a gamma-counter (Perkin Elmer, Waltham, USA). A single background measurement was performed, and the counts per minute from each tissue sample were corrected by background subtraction and radioactive decay. The corrected counts per minute were normalized to the samples weight (g) and converted in SUVs (%).

2.2.1.5 Radio-HPLC

[^{11}C]TMP was injected into the tail vein and 1 min, 5 min, and 10 min post-injection rats (n=1/group) were sacrificed via CO_2 inhalation. Blood was collected from the heart left ventricle and centrifuged at 13.3 rpm for 2 min at 4 °C to separate the plasma. The supernatant (0.3 – 0.7 mL) was recovered and analyzed with radio-HPLC. Afterwards, transcardiac perfusion with ice-cold DPBS (100 mL) was performed. The brain was collected from the skull, homogenized in ice-cold DPBS (500 µL), and analyzed with radio-HPLC. Radio-

HPLC was performed on a Luna 5 µ C18 (2) 100 Angström (Phenomenex, Aschaffenburg, Germany) with 75% H_2O, 0.1% trifluoroacetic acid, 25% acetonitrile.

In Table 7, injected, and molar activities are reported.

Table 7: Radioligand's injected and molar activity. [^{11}C]TMP injected activity and molar activity values.

Study	Injected Activity (Mean ± SD) MBq	Molar Activity (Mean ± SD) GBq/µmol
Baseline	22.4 ± 1.9	49.8 ± 1.6
Sulfamethoxazole	26.6 ± 0.4	77.4 ± 1.4
Elacridar	24.4 ± 2.9	92.5 ± 2.9
Biodistribution	25.7 ± 1.9	34.5 ± 26.2

2.3. Statistics

"Statistical analysis was performed with GraphPad Prism 9.0 (Graphpad Software) if not otherwise stated. Results were analyzed using paired t-test for the within-subjects comparison (right vs left emisphere) and an unpaired t-test for the between-groups comparisons. Correlations between PET and behavioral or ex vivo data were performed using linear regression analysis. Synaptic dysfunction discrimination was tested with multiple-comparison ANOVA" [1]. Results were considered significant for $^{+}P < 0.05$, $^{*}P \leq 0.01$, $^{**}P \leq 0.001$.

3 Results

3.1. Imaging endogenous gene expression changes in the rat brain

3.1.1 *In vitro* validation of the CRISPR/SaCas9-induced *Slc18a2* KD

3.1.1.1 Immunofluorescence

Neurons were stained for DAPI (first column), GFP (sgRNA, second column), HA-tag (SaCas9, third column), and VMAT2 protein (fourth column). VMAT2 expression (red) was highly abundant in the cytoplasm of non-transduced neurons (Figure 14A), neurons transduced solely with sgRNA-*Slc18a2* (Figure 14B), and control neurons transduced with sgRNA-*lacZ* and SaCas9 (Figure 14C). Contrarily, in neurons transduced with sgRNA-*Slc18a2* and SaCas9, we observed a noticeable reduction of the VMAT2 protein (Figure 14D).

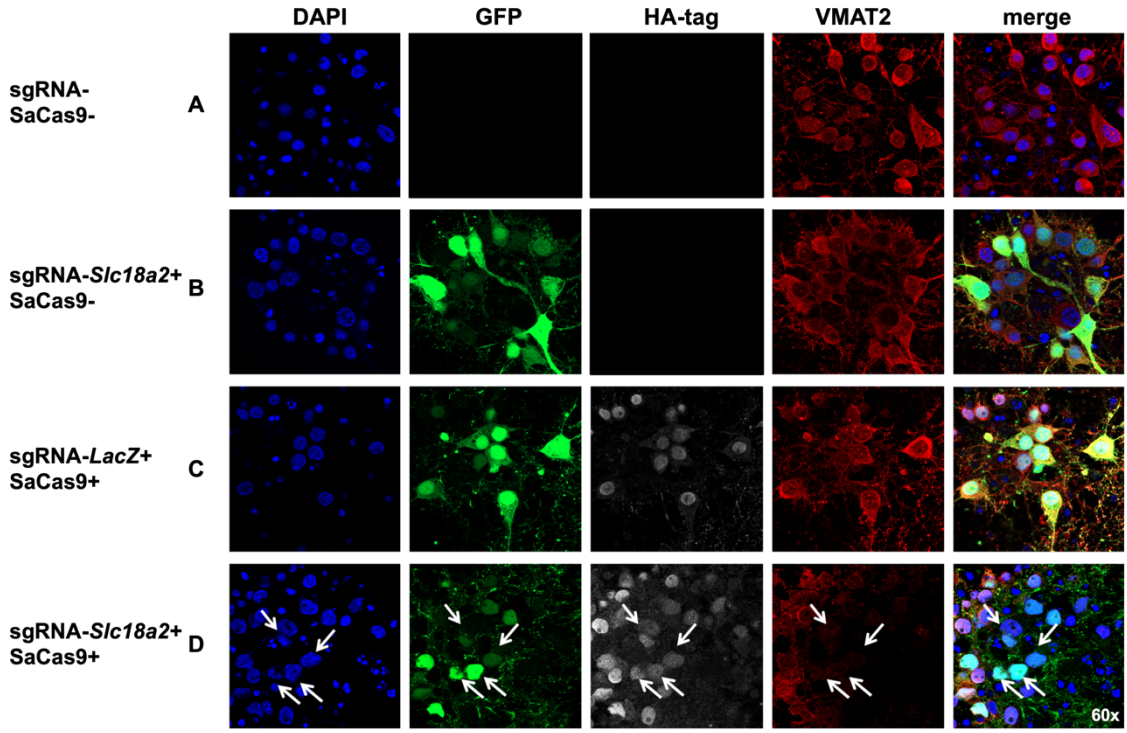

Figure 14: Immunofluorescence. A: Non-transduced neurons. B: Neurons transduced with AAV-PHP.EB-sgRNA-*Slc18a2*. C: Neurons transduced with AAV-PHP.EB-SaCas9 and AAV-PHP.EB-sgRNA-*lacZ*. D: Neurons transduced with AAV-PHP.EB-SaCas9 and AAV-PHP.EB-sgRNA-*Slc18a2*. Nuclei were labeled with DAPI (blue). GFP signal (green) indicates the expression of the sgRNA vector. HA-tag staining (white) indicates the expression of the SaCas9 vector. VMAT2 expression is depicted in red. Figure adapted from [1].

3.1.1.2 Surveyor assay

One-week post-transduction with conditional vectors for SaCas9 and sgRNA- *Slc18a2*, neurons were processed for the Surveyor assay. The expected cleavage products (arrows), and estimated editing of 20%, could be seen for the digested DNA (Figure 15).

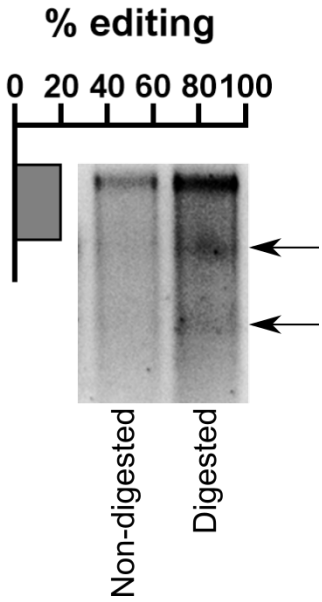

Figure 15: Surveyor assay. The expected cleavage products (arrows), and estimated editing of 20% could be seen for the digested DNA. Figure from [1].

3.1.2 *In vivo* evaluation of the CRISPR/SaCas9-induced *Slc18a2* KD and downstream molecular changes

3.1.2.1 *In vivo* PET imaging

"To test the in vivo efficiency of the CRISPR/SaCas9 gene-editing, we expressed SaCas9 and sgRNA targeting Slc18a2 to knock down the VMAT2, or targeting lacZ as control, by AAV- mediated gene transfer into the SNc. DPBS was injected into the left SNc. [...] [^{11}C]DTBZ BP_{ND} was decreased by 30% (0 - 62%) in the right striatum of rats where the VMAT2 was knocked down in comparison to the contralateral striatum.

No changes of [^{11}C]DTBZ BP_{ND} were observed in the contralateral striatum, as [^{11}C]DTBZ BP_{ND} did not differ between the left striatum of rats injected with sgRNA targeting lacZ and rats injected with sgRNA targeting Slc18a2" [1].

([^{11}C]DTBZ BP_{ND}: control: right striatum: 3.0 ± 0.3, left striatum: 2.9 ± 0.3; VMAT2 KD: right striatum: 1.9 ± 0.7, left striatum: 2.9 ± 0.3, **P*= 0.002, Bonferroni-corrected). *"We further evaluated changes of DA availability in the striatum using [^{11}C]RAC, which competes with DA for the same binding site at the D2R [56]. 12 – 14 weeks after VMAT2 KD in nigrostriatal neurons, we observed 17% increased binding of [^{11}C]RAC in the right striatum of VMAT2 KD rats and no changes in control rats, indicating a reduction of synaptic DA levels and/or compensatory changes of D2R expression at postsynaptic medium spiny neurons*" [1]. ([^{11}C]RAC BP_{ND}: control: right striatum: 2.4 ± 0.2, left striatum: 2.4 ± 0.3; VMAT2 KD: right striatum: 2.6 ± 0.4, left striatum: 2.2 ± 0.2, **P*= 0.007, Bonferroni-corrected) (Figure 16A,B).

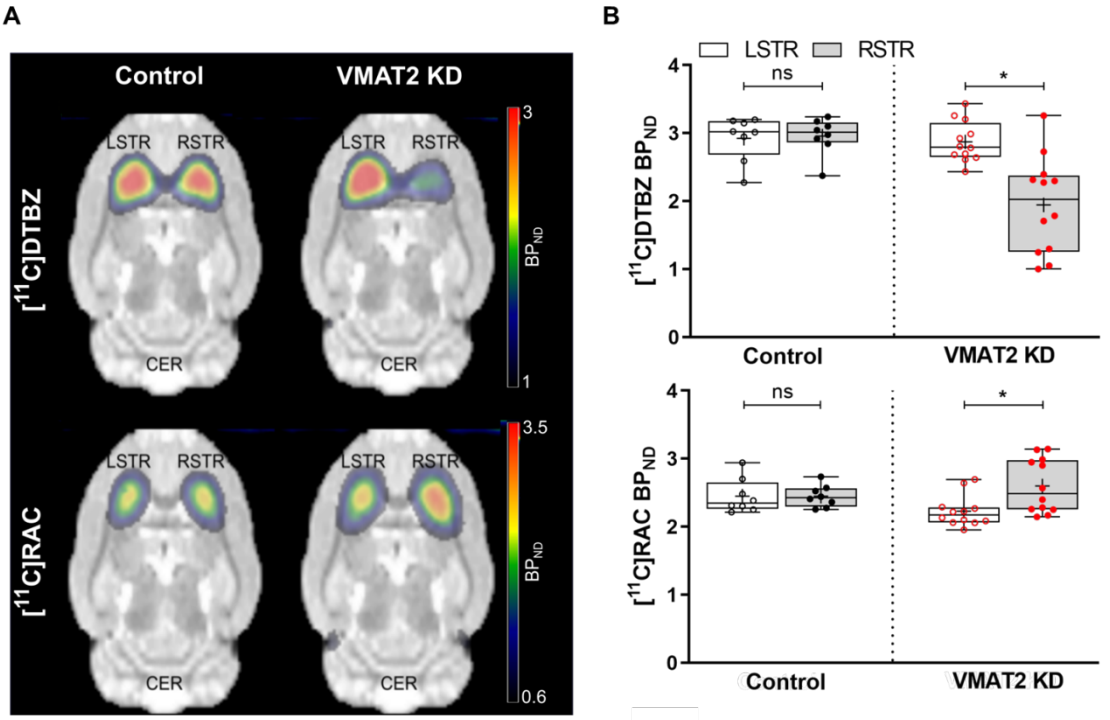

Figure 16: Downstream molecular changes following CRISPR/SaCas9-induced *Slc18a2* KD. A: Mean BP_{ND} maps of control and VMAT2 KD rats co-registered to the Schiffer anatomical MRI atlas. B: BP_{ND} values of individual control and VMAT2 KD rats in the left and right striatum. Kinetic modeling was applied using the Logan Reference. BP_{ND} were calculated from individual TACs of the left striatum (LSTR), right striatum (RSTR), and cerebellum (CER), which was used as a reference region. LSTR: DPBS-injected, RSTR: AAV-injected, Control: AAV-PHP.EB-SaCas9 and AAV-PHP.EB-sgRNA-*lacZ*, VMAT2 KD: AAV-PHP.EB-SaCas9 and AAV-PHP.EB-sgRNA-*Slc18a2*. Figure adapted from [1].

"A larger VMAT2 KD led putatively to lower DA levels in the striatum and likely to a higher D2R BP_{ND}" [1] (R^2= 0.64, ***P*< 0.0001) (Figure 17).

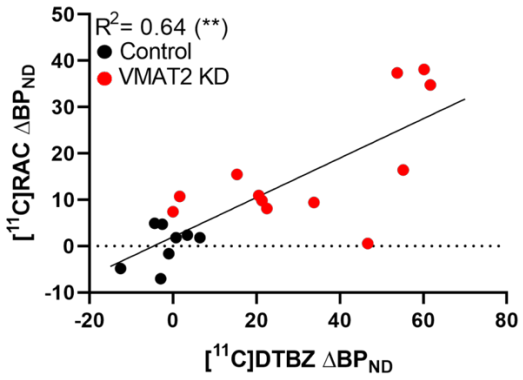

Figure 17: Correlations of CRISPR/SaCas9-induced *Slc18a2* KD and downstream molecular changes. Linear regression modeling the relationship between the [^{11}C]DTBZ and [^{11}C]RAC binding changes (%, ΔBP_{ND}). Control: AAV-PHP.EB-SaCas9 and AAV-PHP.EB-sgRNA-*lacZ*, VMAT2 KD: AAV-PHP.EB-SaCas9 and AAV-PHP.EB-sgRNA-*Slc18a2*. Figure adapted from [1].

"We calculated the [^{11}C]RAC/[^{11}C]DTBZ BP_{ND} ratio for the right and left striatum to explore the threshold at which the observed postsynaptic changes occur. The ratio remained close to 1 in the DPBS-injected striatum and control rats, indicating no substantial difference between the two hemispheres. In contrast, VMAT2 KD rats displayed large [^{11}C]RAC BP_{ND} changes when the level of VMAT2 KD was ~ 20%. From this point, a noticeable increase in D2R BP_{ND} was observed in the right striatum" [1] (Left striatum: R^2= 0.02, right striatum: R^2= 0.78, ***P*< 0.0001) (Figure 18).

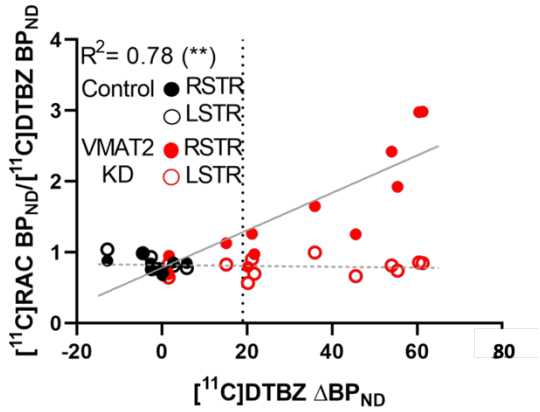

Figure 18: Threshold of [^{11}C]RAC changes as a function of CRISPR/SaCas9-induced *Slc18a2* KD. DA availability changes following the VMAT2 KD for the left (DPBS-injected, empty dots) and right (AAV-injected, full dots) striatum. VMAT2 KD extent is expressed as [^{11}C]DTBZ binding changes (%, ΔBP_{ND}). Control: AAV-PHP.EB-

SaCas9 and AAV-PHP.EB-sgRNA-*lacZ*, VMAT2 KD: AAV-PHP.EB-SaCas9 and AAV-PHP.EB-sgRNA-*Slc18a2*. Figure adapted from [1].

"Therefore the 20% threshold was set to split the VMAT2 KD rats into mild (n= 3, [^{11}C]DTBZ ΔBP_{ND} < 20% (5.7 ± 8.4)), and moderate (n= 9, [^{11}C]DTBZ ΔBP_{ND} ≥ 20% (41.8 ± 17.3)). Notably, [^{11}C]RAC PET imaging was able to discriminate between different degrees of synaptic dysfunction, classified from [^{11}C]DTBZ BP_{ND} changes" [1] (*mild vs moderate* **P*= 0.004, control *vs moderate* ***P*< 0.0001) (Figure 19).

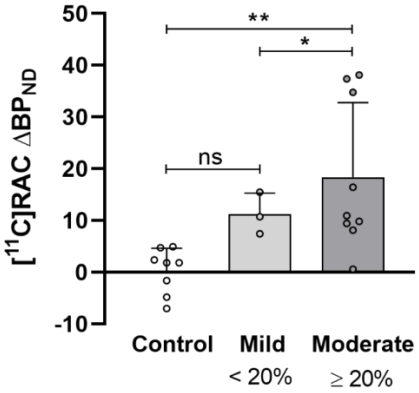

Figure 19: [^{11}C]RAC classifier analysis. [^{11}C]RAC lesion type discrimination was tested in control and VMAT2 KD *mild* and *moderate* rats. *Mild*: [^{11}C]DTBZ ΔBP_{ND} < 20%; *Moderate*: [^{11}C]DTBZ ΔBP_{ND} ≥ 20%. Figure adapted from [1].

"We next inspected the integrity of the nerve terminals and the occurrence of inflammation in the striatum after the VMAT2 KD. [^{11}C]MP PET imaging of the DAT and [^{18}F]GE-180 PET imaging of the translocator protein (TSPO), overexpressed on activated microglia, was performed" [1]. VMAT2 KD did neither alter [^{11}C]MP BP_{ND} ([^{11}C]MP BP_{ND}: control: right striatum: 1.0 ± 0.1, left striatum: 0.9 ± 0.1; VMAT2 KD: right striatum: 0.9 ± 0.1, left striatum: 0.8 ± 0.1), nor [^{18}F]GE-180 uptake ([^{18}F]GE-180 $RSTR_{norm}$: control: 1.0 ± 0.1; VMAT2 KD: 1.0 ± 0.1) (Figure 20).

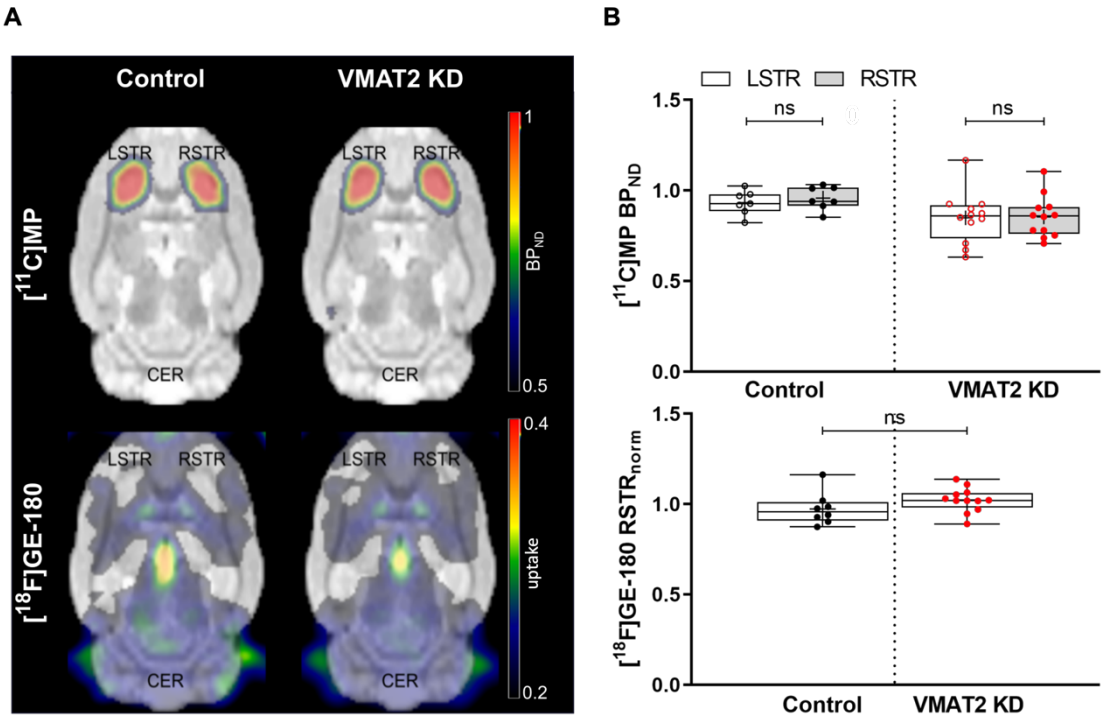

Figure 20: Downstream molecular changes following CRISPR/SaCas9-induced *Slc18a2* KD. A: Mean BP_{ND} maps of control and VMAT2 KD rats co-registered to the Schiffer anatomical MRI atlas. B: BP_{ND} values of individual control and VMAT2 KD rats in the left and right striatum. Kinetic modeling was applied using the Logan Reference for [^{11}C]MP. BP_{ND} were calculated from individual TACs of the left striatum (LSTR), right striatum (RSTR), and cerebellum (CER), which was used as a reference region. For [^{18}F]GE-180 standard uptake values normalized to the left striatum are shown. LSTR: DPBS-injected, RSTR: AAV-injected, Control: AAV-PHP.EB-SaCas9 and AAV-PHP.EB-sgRNA-*lacZ*, VMAT2 KD: AAV-PHP.EB-SaCas9 and AAV-PHP.EB-sgRNA-*Slc18a2*. Figure adapted from [1].

3.1.2.2 Behavioral studies

The downstream motor changes following the CRISPR/Cas9-induced *Slc18a2* KD were characterized with behavioral tests, as reported in the timeline below (Figure 21).

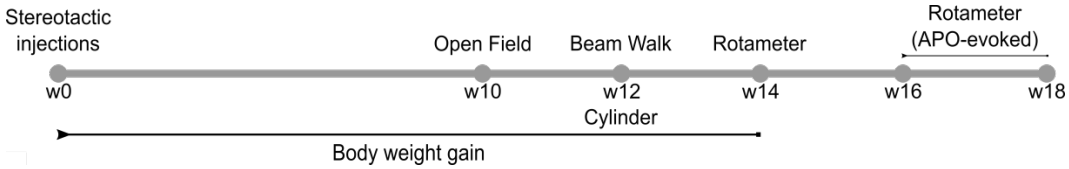

Figure 21: Timeline of the behavioral experiments. Adapted from [1].

Motor tests were performed to assess the forelimb akinesia (Figure 22), locomotor activity (Figure 23), gait and balance (Figure 24), and spontaneous (Figures 25) and apomorphine-evoked (Figure 26) rotational behavior. Finally, as previous studies suggest that body weight changes reflect striatal DA depletion

[256], we inspected the impact of the VMAT2 KD on the rats' body weight gain (Figure 27).

3.1.2.2.1 Cylinder test

We evaluated the forelimb akinesia using the cylinder test (Figure 22A). VMAT2 KD rats displayed a preference for the right forepaw, while control rats used their right and left forepaw with the same frequency (Contralateral paw touches, % to total: control: 50.5 ± 4.8; VMAT2 KD: 37.8 ± 9.3, *P= 0.002) (Figure 22B). Paw use alterations highly correlated with VMAT2 KD ([^{11}C]DTBZ ΔBP_{ND}) (R^2= 0.71, **P< 0.0001), and DA availability/D2R changes ([^{11}C]RAC ΔBP_{ND}) (R^2= 0.67, **P< 0.0001) (Figure 22C,D).

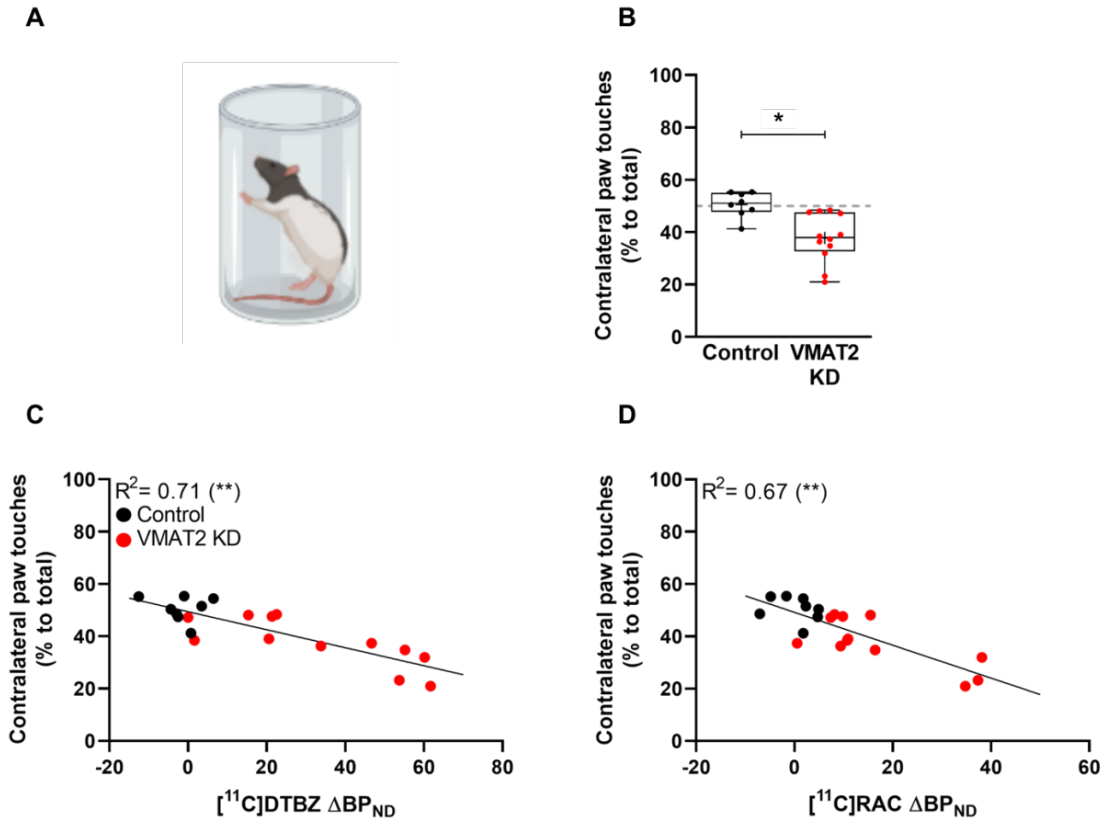

Figure 22: Forelimb akinesia and its correlation with the molecular changes. A: Representation of the cylinder test assessing the spontaneous forelimb lateralization. B: Contralateral paw touches (% to total) were measured for control and VMAT2 KD rats. C,D: Linear regression of the rats' performance in the cylinder test and [^{11}C]DTBZ and [^{11}C]RAC ΔBP_{ND}, respectively. Control: AAV-PHP.EB-SaCas9 and AAV-PHP.EB-sgRNA-*lacZ*, VMAT2 KD: AAV-PHP.EB-SaCas9 and AAV-PHP.EB-sgRNA-*Slc18a2*. Figure adapted from [1].

3.1.2.2.2 Open Field

Locomotor activity was measured in an open field where rats could walk freely for 11 min (Figure 23A). *"We observed a reduction in the locomotor activity of VMAT2 KD rats in the open field test* (Travelled distance (m): control: 19.6 ± 2.2; VMAT2 KD: 15.7 ± 4.2, ^{+}P= 0.03) (Figure 23B), *but no correlation to VMAT2 expression changes* ([^{11}C]DTBZ ΔBP_{ND}) (R^2= 0.12), *or DA availability/D2R changes* ([^{11}C]RAC ΔBP_{ND}) (R^2= 0.03) (Figure 23C,D)*"* [1].

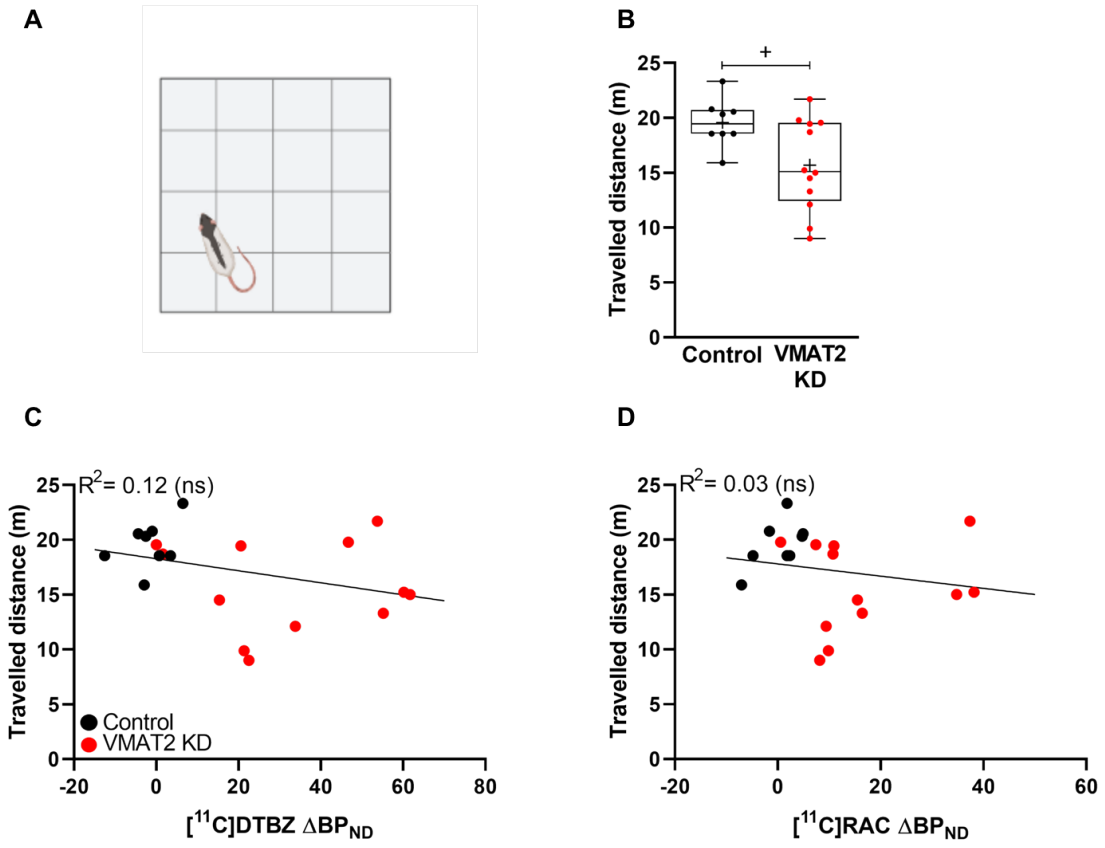

Figure 23: Locomotor activity and its correlation with the molecular changes. A: Representation of the open field test assessing the animals' locomotion. B: Travelled distance (m) was measured in an open field for control and VMAT2 KD rats. C,D: Linear regression modeling the distance traveled by the rats and [^{11}C]DTBZ and [^{11}C]RAC ΔBP_{ND}, respectively. Control: AAV-PHP.EB-SaCas9 and AAV-PHP.EB-sgRNA-*lacZ*, VMAT2 KD: AAV-PHP.EB-SaCas9 and AAV-PHP.EB-sgRNA-*Slc18a2*. Figure adapted from [1].

3.1.2.2.3 Beam Walk

Using the beam walk test we evaluated the motor function, coordination, and balance (Figure 24A). *"VMAT2 KD rats stumbled with higher frequency to the left side, while control rats displayed equal chances to slip in each direction*

(Contralateral footslips, % to total steps: control: 55.3 ± 15.9; VMAT2 KD: 78.7 ± 20.1, *P= 0.01) (Figure 24B). *No correlations between gait alterations and VMAT2 KD* ([^{11}C]DTBZ ΔBP_{ND}) (R^2= 0.08) (Figure 24C) *or DA availability/D2R changes* ([^{11}C]RAC ΔBP_{ND}) (R^2= 0.02) *were found* (Figure 24D)*"* [1].

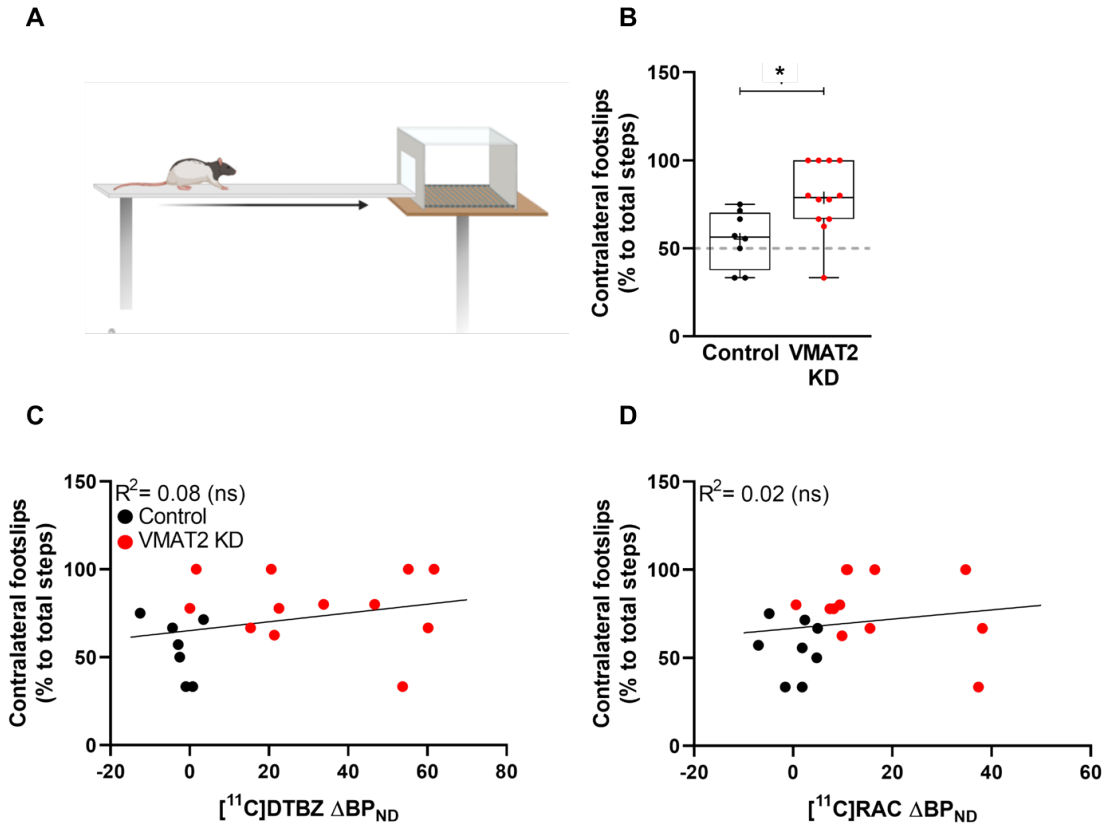

Figure 24: Gait function and its correlation with the molecular changes. A: Representation of the beam walk test evaluating the animals' motor function, coordination, and balance. B: Contralateral footslips (% to total steps) were counted for control and VMAT2 KD rats. C, D: Linear regression indicating the correlation between the number of contralateral footslips and [^{11}C]DTBZ and [^{11}C]RAC ΔBP_{ND}, respectively. Control: AAV-PHP.EB-SaCas9 and AAV-PHP.EB-sgRNA-*lacZ*, VMAT2 KD: AAV-PHP.EB-SaCas9 and AAV-PHP.EB-sgRNA-*Slc18a2*. Figure adapted from [1].

3.1.2.2.4 Rotameter test: spontaneous rotation

Spontaneous rotation in a novel spherical environment was evaluated during a 5 min session in a rotameter (Figure 25A). VMAT2 KD rats displayed more ipsilateral net turns than control rats (Turns/min: control: -5.6 ± 9.4; VMAT2 KD: 6.7 ± 14.6, ^{+}P= 0.04) (Figure 25B). "*The number of turns did not correlate with VMAT2 expression changes* ([^{11}C]DTBZ ΔBP_{ND}) (R^2= 0.13) (Figure 25C), *nor changes in DA availability/D2R expression"* [1] ([^{11}C]RAC ΔBP_{ND}) (R^2= 0.05) (Figure 25D).

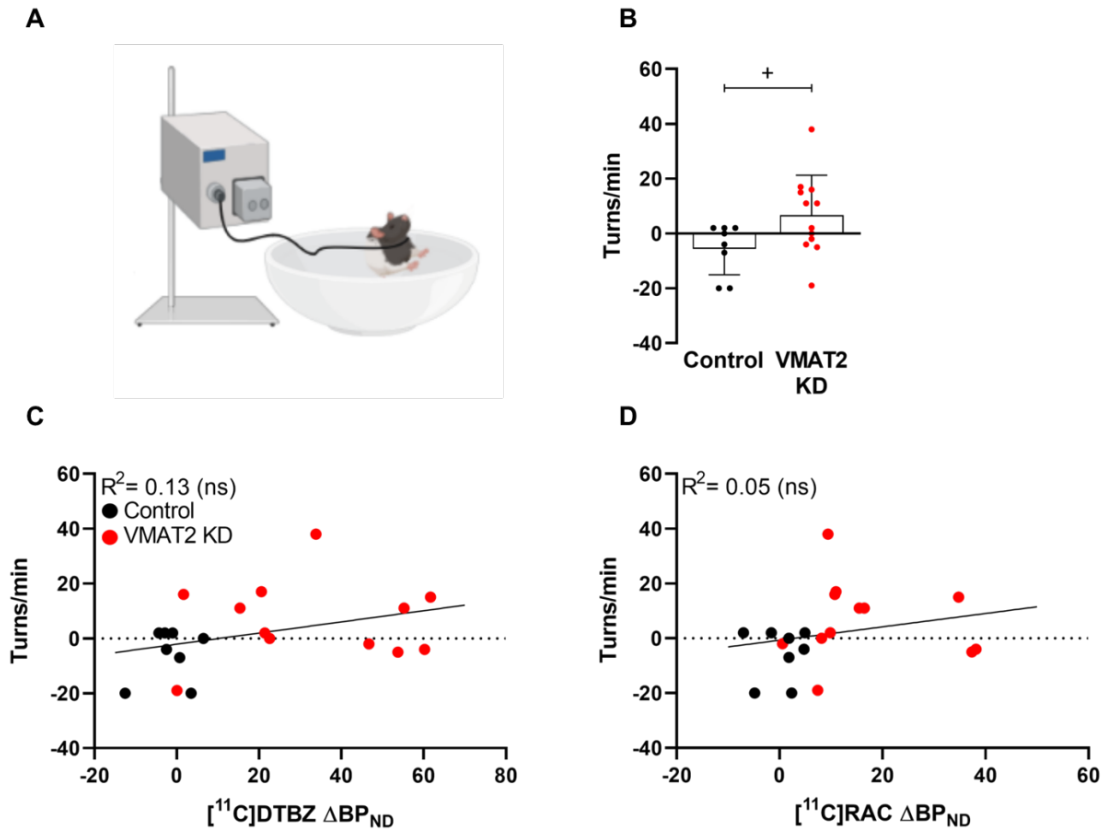

Figure 25: Spontaneous rotational behavior and its correlation with the molecular changes. A: Representation of the rotameter test. B: Spontaneous turns/min of control and VMAT2 KD rats in a novel spherical environment. C,D: Linear regression modeling the correlation between the rotational asymmetry and [^{11}C]DTBZ or [^{11}C]RAC ΔBP_{ND}, respectively. Control: AAV-PHP.EB-SaCas9 and AAV-PHP.EB-sgRNA-*lacZ*, VMAT2 KD: AAV-PHP.EB-SaCas9 and AAV-PHP.EB-sgRNA-*Slc18a2*. Figure adapted from [1].

3.1.2.2.5 Rotameter test: apomorphine-induced rotation

Apomorphine-induced rotations were evaluated during a 60 min session in a rotameter (Figure 26A). Rotations to the contralateral side were higher in VMAT2 KD rats compared to control rats (CCW turns/min, APO-evoked: control: 4.2 ± 23.3; VMAT2 KD: 237.8 ± 199.0; *P= 0.004) (Figure 26B), and correlated with changes in VMAT2 expression ([^{11}C]DTBZ ΔBP_{ND}) (R^2= 0.54, **P= 0.0002) and DA availability/D2R expression ([^{11}C]RAC ΔBP_{ND}) (R^2= 0.37, *P= 0.005) (Figure 26C,D).

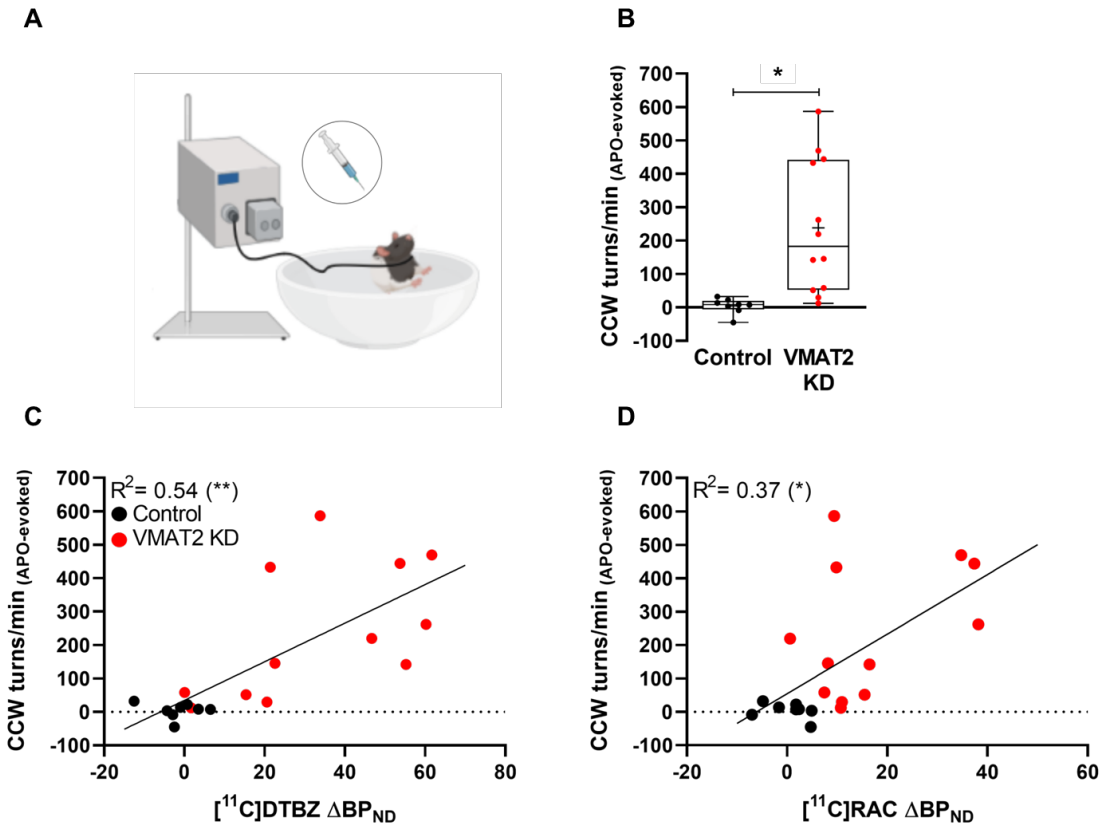

Figure 26: Apomorphine-evoked rotational behavior and its correlation with the molecular changes. A: Representation of the drug-evoked rotameter test. B: Number of CCW turns in the rotameter test following the third apomorphine administration for control and VMAT2 KD rats. C,D: Linear regression modeling the correlation between the drug-evoked rotations and the [^{11}C]DTBZ and [^{11}C]RAC ΔBP_{ND}, respectively. Control: AAV-PHP.EB-SaCas9 and AAV-PHP.EB-sgRNA-*lacZ*, VMAT2 KD: AAV-PHP.EB-SaCas9 and AAV-PHP.EB-sgRNA-*Slc18a2*. Figure adapted from [1].

3.1.2.2.6 Body weight gain

Body weight gain was measured over 14 weeks (Figure 27A). VMAT2 KD rats exhibited a 30% reduction in their gained weight, compared with controls (Body weight gain (g): control: 65.3 ± 13.2; VMAT2 KD: 46.2 ± 6.7, ***P*= 0.0004) (Figure 27B). Body weight gain correlated with changes in VMAT2 expression ([^{11}C]DTBZ ΔBP_{ND}) (R^2= 0.39, **P*= 0.003), and DA availability/D2R changes ([^{11}C]RAC ΔBP_{ND}) (R^2= 0.32, **P*= 0.01) (Figure 27C,D).

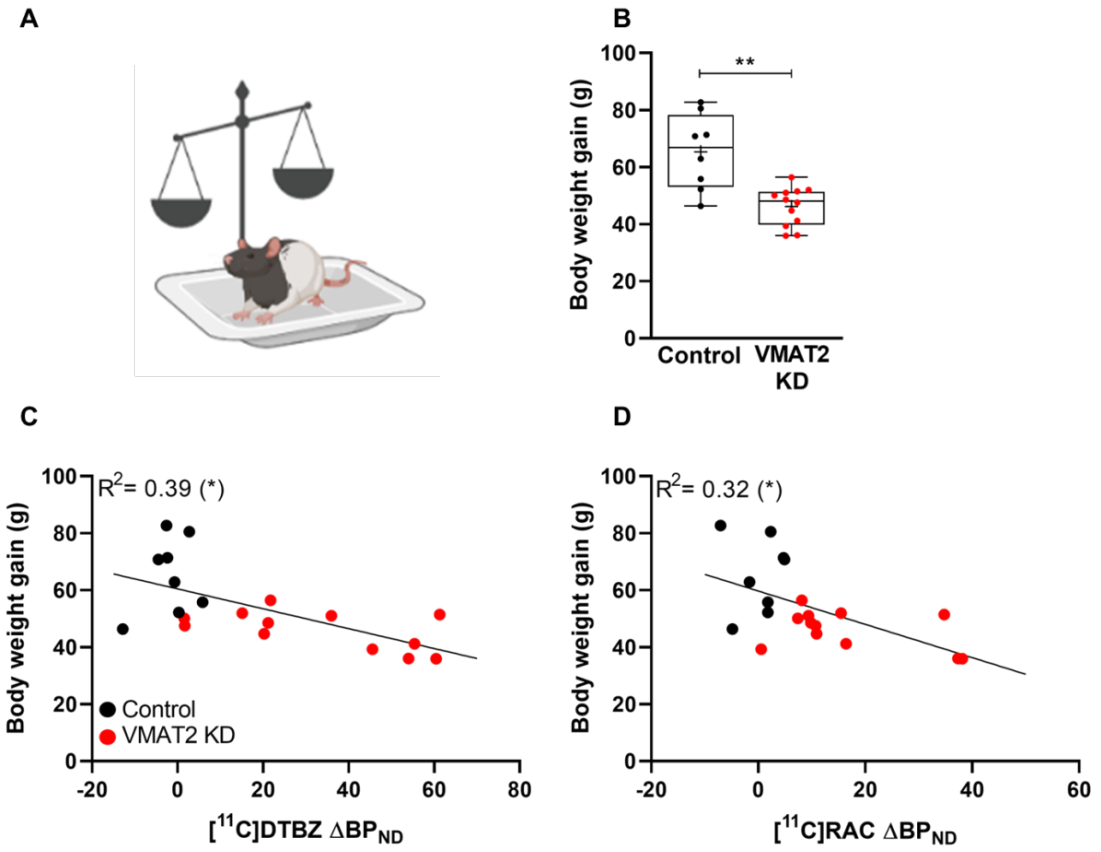

Figure 27: Body weight gain and its correlation with the molecular changes. A: Body weight was measured before and 14 weeks after CRISPR/Cas9-targeting in control and VMAT2 KD rats (B). C,D: Linear regression modeling the correlation between body weight gain and [^{11}C]DTBZ and [^{11}C]RAC ΔBP_{ND}, respectively. Control: AAV-SaCas9 and AAV-sgRNA-*lacZ*; VMAT2 KD: AAV-SaCas9 and AAV-sgRNA-*Slc18a2*. Figure adapted from [1].

3.1.3 *Ex vivo* evaluation of the CRISPR/SaCas9-induced *Slc18a2* KD

3.1.3.1 Immunofluorescence

"Using immunofluorescence, we confirmed the concomitant expression of SaCas9 and Slc18a2–targeting sgRNA 19 weeks post-transduction and a corresponding decrease of VMAT2 expression in the SNc of the VMAT2 KD group" [1] (Figure 28).

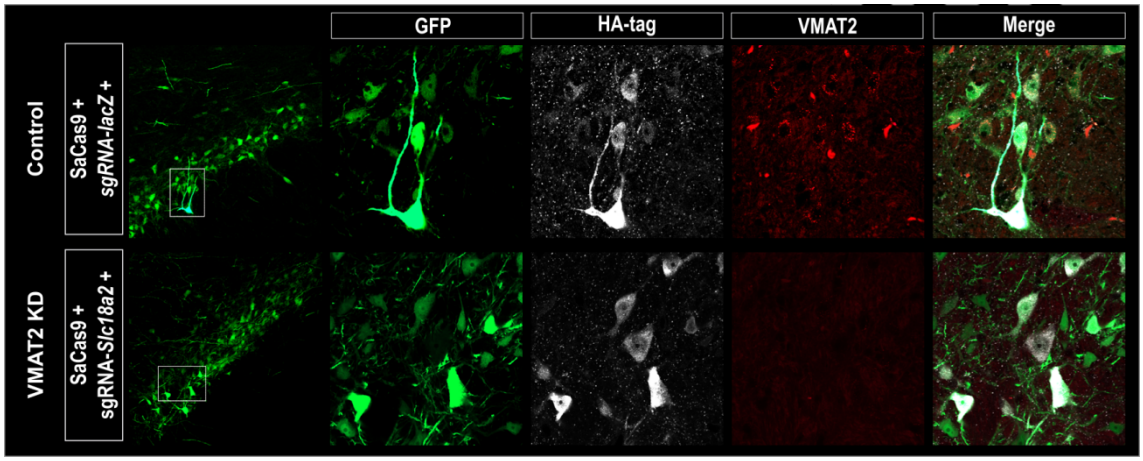

Figure 28: Immunofluorescence. Immunofluorescence for GFP (AAV-sgRNAs, green), HA-tag (AAV-SaCas9, white), and VMAT2 expression (red) of nigral sections for two exemplary rats. Control: AAV-SaCas9 and AAV-sgRNA-*lacZ*; VMAT2 KD: AAV-SaCas9 and AAV-sgRNA-*Slc18a2*. Figure adapted from [1].

3.1.3.2 Immunohistochemistry

"IHC revealed a reduction of VMAT2 expression in the right striatum and SN (Figure 29A), but no changes in TH expression levels in striatum and SN" [1] (Total number of TH+ cells: control: right SNc: 11,873 ± 6,706, left SNc: 12,287 ± 8,145; VMAT2 KD: right SNc: 13,857 ± 5,490, left SNc: 16,789 ± 6,039) (Figure 29B,C).

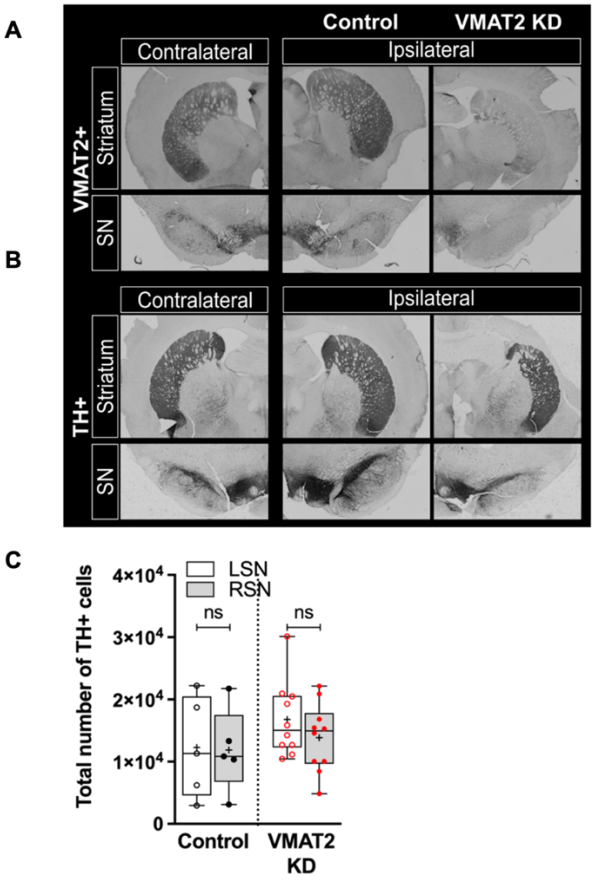

Figure 29: Immunohistochemistry. IHC of VMAT2 (A) and TH (B,C) expression in the ipsilateral and contralateral striatum and SN of VMAT KD and control rats. Control: AAV-SaCas9 and AAV-sgRNA-*lacZ*; VMAT2 KD: AAV-SaCas9 and AAV-sgRNA-*Slc18a2*. Figure adapted from [1].

3.1.3.3 Biochemistry

"Biochemical analysis showed a large reduction of DA (DA nmol/mg: control: right striatum: 308 ± 166, left striatum: 244 ± 109; VMAT2 KD: right striatum: 100 ± 97, left striatum: 351 ± 169) (Figure 30A), *paralleled by an increased ratio of DA metabolites* (*DOPAC, HVA) to DA, in the right striatum of VMAT2 KD rats* (DA turnover rate: control: right striatum: 0.37 ± 0.41, left striatum: 0.33 ± 0.28; VMAT2 KD: right striatum: 0.85 ± 0.50, left striatum: 0.19 ± 0.08) (Figure 30B). *The reduced DA content correlated with the in vivo VMAT2 expression changes* ([^{11}C]DTBZ ΔBP_{ND}) (R^2= 0.28, ^{+}P= 0.04) *and postsynaptic changes"* [1] ([^{11}C]RAC ΔBP_{ND}) (R^2= 0.36, ^{+}P= 0.02) (Figure 30C,D).

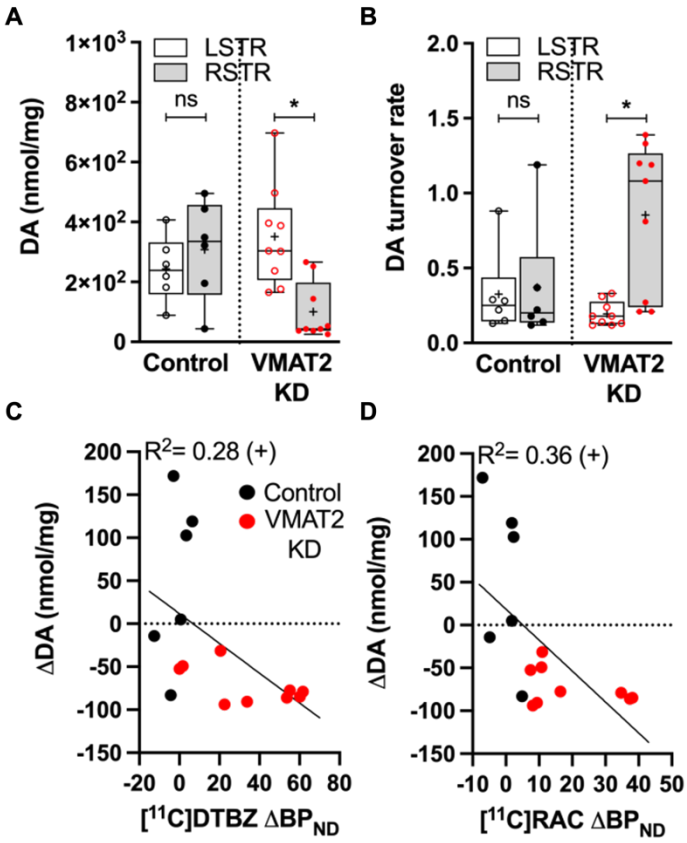

Figure 30: Biochemistry. A: Striatal DA, normalized to total protein concentration, in control and VMAT2 KD rats. B: DA turnover rate in control and VMAT2 KD rats. C,D: Linear regression modeling striatal DA changes and VMAT2 KD extent and postsynaptic changes, deducted from [^{11}C]DTBZ and [^{11}C]RAC, respectively. Control: AAV-SaCas9 and AAV-sgRNA-*lacZ*; VMAT2 KD: AAV-SaCas9 and AAV-sgRNA-*Slc18a2*. Figure adapted from [1].

5-HT was unchanged in the striata of VMAT2 KD and control rats (5-HT nmol/mg: control: right striatum: 19.5 ± 5.8, left striatum: 17.2 ± 2.2; VMAT2 KD: right striatum: 22.9 ± 8.5, left striatum: 19.2 ± 8.4), suggesting DA nigrostriatal pathway specificity. Metabolites and neurotransmitters striatal levels are reported in Table 8.

Table 8: Neurotransmitters' striatal content. DA (dopamine), DOPAC (3,4-Dihydroxyphenylacetic acid), HVA (homovanillic acid), and 5-HT (serotonin) striatal content determined by HPLC. Table from [1].

Neurotransmitter or Metabolite	nmol/mg (mean ± SD)	
DA	**Control**	**VMAT2 KD**
STR-L	244 ± 109	351 ± 168
STR-R	308 ± 166	100 ± 97
DOPAC	**Control**	**VMAT2 KD**
STR-L	34 ± 7	34 ± 11
STR-R	38 ± 4	27 ± 5
HVA	**Control**	**VMAT2 KD**
STR-L	24 ± 5	25 ± 5
STR-R	26 ± 6	19 ± 4
5-HT	**Control**	**VMAT2 KD**
STR-L	17 ± 2	19 ± 8
STR-R	19 ± 6	23 ± 9

3.1.4. *In vivo* evaluation of the CRISPR/SaCas9-induced *Slc18a2* KD and downstream functional connectivity changes

3.1.4.1 PET/BOLD-fMRI

"As multiple lines of evidence suggest a broader role of DA in the dynamic reconfiguration of brain networks [32, 257, 258], we next investigated the impact of unilateral DA depletion on brain rs-FC. A second cohort of rats underwent longitudinal simultaneous [^{11}C]RAC-PET/BOLD-fMRI scans at baseline and 8 - 14 weeks after CRISPR/SaCas9-induced VMAT2 KD (Figure 13). [^{11}C]DTBZ PET scans and behavioral analysis confirmed previous findings in the first cohort, that is, an efficient depletion of the VMAT2 (20% decrease of [^{11}C]DTBZ binding) (Figure 31A), paralleled by motor disturbances in the cylinder test (Figure 31E-G). In line with the findings of cohort 1, DA availability was decreased (10% increase in [^{11}C]RAC binding and correlated to the extent of the VMAT2 KD (Figure 31B,C). An increase in D2R binding was observed in the right striatum when the level of VMAT2 KD reached ~ 20% (Figure 31D), enabling a subdivision into mild (< 20%) and moderate rats (≥ 20%)" [1].

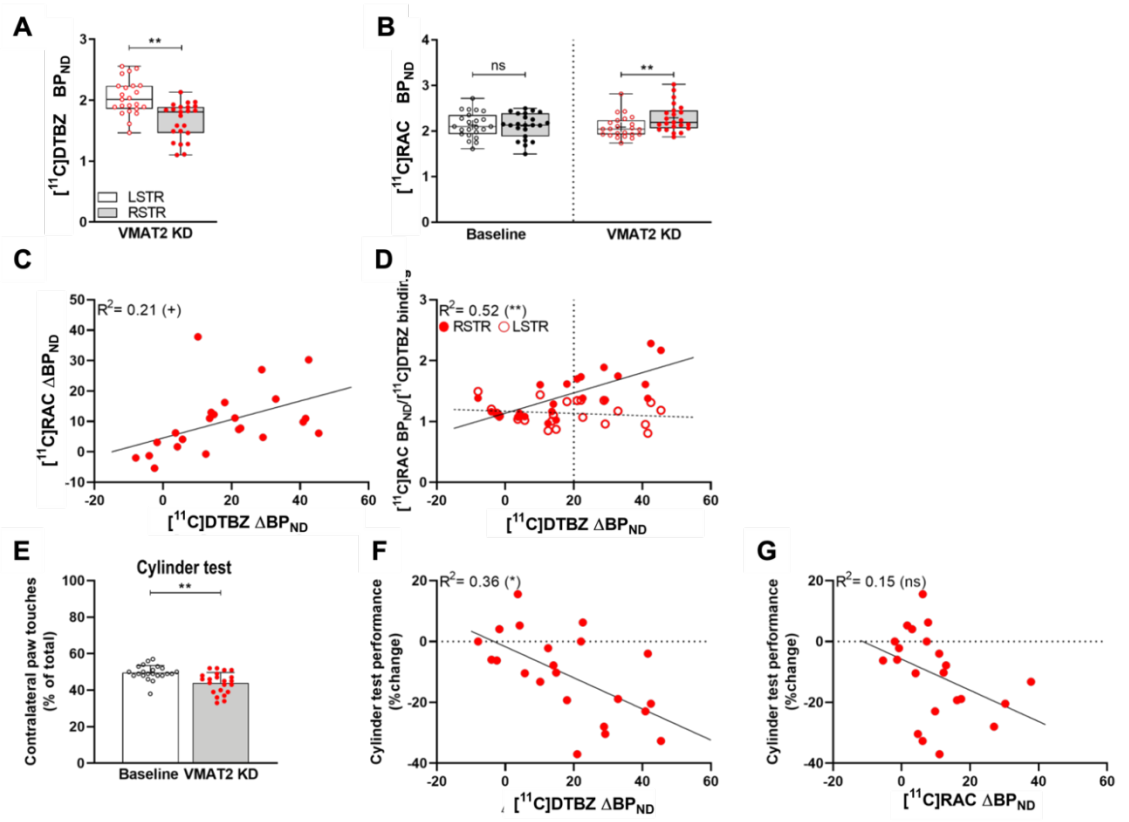

Figure 31: Reproducibility of the CRISPR/SaCas9-induced VMAT2 KD. A: [^{11}C]DTBZ in VMAT2 KD rats and B: [^{11}C]RAC PET at baseline and after CRISPR/SaCas9-induced VMAT2 KD. C: Correlation between [^{11}C]RAC and [^{11}C]DTBZ ΔBP_{ND}. D: At 20% VMAT2 KD ([^{11}C]DTBZ ΔBP_{ND}), D2R binding ([^{11}C]RAC binding) prominently increased. This threshold was therefore set to separate the rats into *mild* and *moderate*. E: Cylinder test at baseline and 12 - 14 weeks after CRISPR/SaCas9 gene-editing. F,G: Rats performance in the cylinder test, % change from baseline, and correlation with VMAT2 expression ([^{11}C]DTBZ ΔBP_{ND}) and DA availability/D2R changes ([^{11}C]RAC ΔBP_{ND}). VMAT2 KD: AAV-SaCas9 and AAV-sgRNA-*Slc18a2*. Figure adapted from [1].

"We next assessed the occurrence of rs-FC changes in DMN and SMN. Our analysis focused on identifying early biomarkers of mild dysfunction and patterns of spreading of synaptic dysfunction. Figure 32A,B illustrates intraregional rs-FC group-level correlation matrices at baseline and after VMAT2 KD in mild and moderate rats for the DMN and SMN, respectively. We observed within-network rs-FC changes in rats with moderate VMAT2 KD, in both DMN and SMN.

Rats of the mild KD group revealed rs-FC changes up to 20%, in prefrontal cortical regions of the DMN, and between the left thalamus (Th) and somatosensory cortex (SC) in the SMN. However, these data need to be carefully

*interpreted as they did not survive a more stringent P value selection (*P< 0.01) (P values are reported in Table 9,10).*

Rats with moderate VMAT2 KD exhibited a 60% increase in rs-FC within the right medial prefrontal cortex (mPFC) and the right and left hippocampus (Hipp) (Figure 31B) (P values are reported in Table 11).

FC increase between the left thalamus and somatosensory cortex in the SMN doubled to 34% in rats with moderate VMAT2 KD and extended throughout the left and right thalamus and striatum, respectively (Figure 32B) (P values are reported in Table 12).

Moreover, we inspected rs-FC changes between the DMN and SMN at baseline and after the CRISPR/SaCas9-induced VMAT2 KD.

Figure 32C illustrates internetwork rs-FC correlation matrices in rats with mild (left panel) and moderate (right panel) VMAT2 KD. Brain graphs display the nodes and edges (raw values) that demonstrated internetwork rs-FC changes to baseline (%). Strikingly, large alterations between DMN and SMN were already observable in the mild VMAT2 KD group. Rats presented opposite rs-FC changes between regions of the anterior/posterior DMN and the SMN, compared with baseline. A 30 to 60% increase in rs-FC was observed between regions of the anterior DMN and the SMN. Specifically, rs-FC increased between the right orbitofrontal cortex (OFC) and striatum bilaterally and the contralateral somatosensory cortex, and between the contralateral orbitofrontal cortex and striatum. Instead, a 20% decrease in rs-FC was found between regions of the posterior DMN and the SMN. Specifically, rs-FC decreased between the left retrosplenial cortex (RSC) and right somatosensory cortex (Figure 32C, left panel) (P values are reported in Table 13).

Rats with a moderate VMAT2 KD presented increased rs-FC between regions of the anterior/posterior DMN and the SMN, compared with baseline. Of particular note, internetwork rs-FC changes were not found between the regions of the posterior DMN and the SMN that showed decreased rs-FC in rats with mild VMAT2 KD. Moreover, between-network rs-FC increase extended to other regions. A 60 to 80% increase in rs-FC was found between the medial prefrontal cortex and the right striatum, and the motor (MC) and somatosensory cortex

bilaterally. FC increased by more than 20% between the hippocampi and contralateral somatosensory cortex. (Figure 32C, right panel) (P values are reported in Table 14). Notably, between-network rs-FC changes did not involve the thalamus, which connectivity was however altered within the SMN" [1].

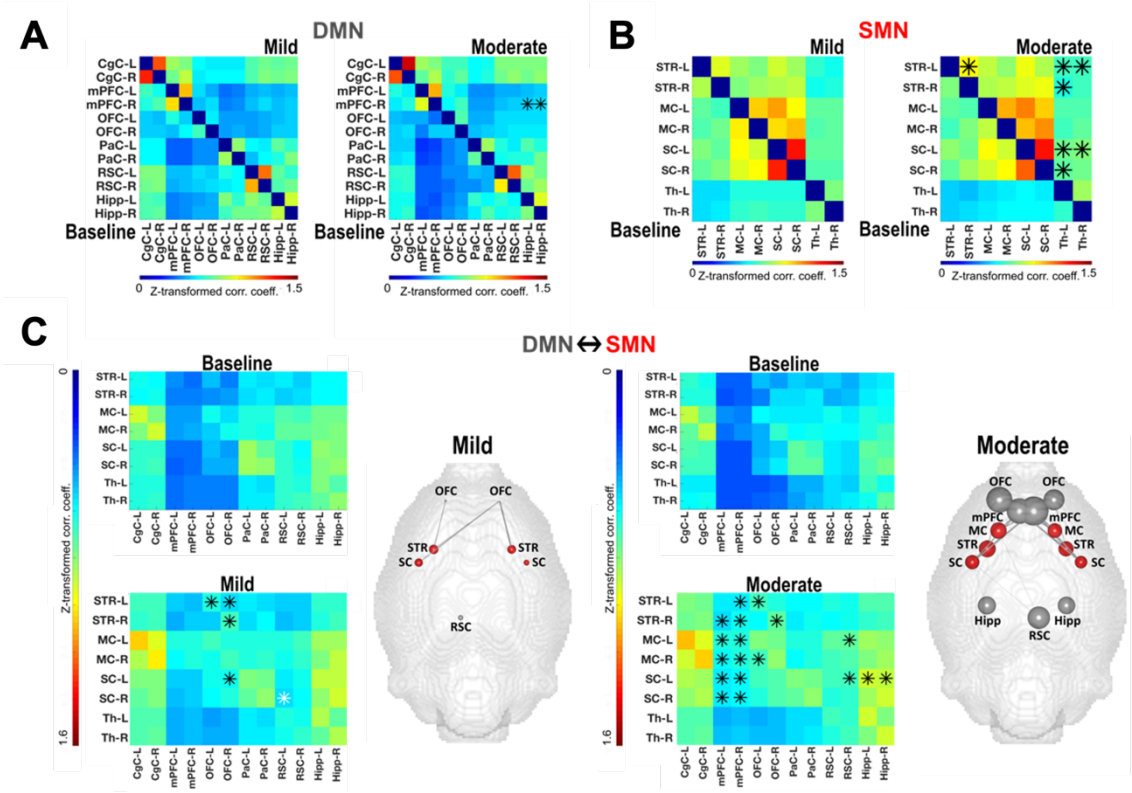

Figure 32: PET/BOLD-fMRI. Group level correlation matrices of the DMN (A) and SMN (B) at baseline and after CRISPR/SaCas9-targeting for rats with a *mild* (left panel) and *moderate* (right panel) VMAT2 KD. C: Internetwork rs-FC changes in the *mild* (left panel) and *moderate* (right panel) VMAT2 KD rats. Brain graphs, right to the matrices, illustrate the nodes and edges (raw values) that demonstrated rs-FC changes to baseline (%). **P*< 0.01. VMAT2 KD: AAV-SaCas9 and AAV-sgRNA-*Slc18a2*. *Mild*: [^{11}C]DTBZ ΔBP_{ND} < 20%; *Moderate*: [^{11}C]DTBZ $\Delta BP_{ND} \geq$ 20%. VMAT2 KD: AAV-SaCas9 and AAV-sgRNA-*Slc18a2*. Abbreviations of brain regions considered for the analysis of the fMRI data, including their respective volumes, are reported in Table 6. Figure adapted from [1].

Table 9: *P* values of the FC changes. *P* values of the FC changes in regions of the DMN for rats with *mild* VMAT2 KD. Data were analyzed using paired t-tests. Table from [1].

Mild	Hipp-R	Hipp-L	RSC-R	RSC-L	PaC-R	PaC-L	OFC-R	OFC-L	mPFC-R	mPFC-L	CgC-R
CgC-L	0.40	0.56	0.95	0.33	0.76	0.84	0.22	0.27	0.07	0.07	0.61
CgC-R	0.30	0.41	0.83	0.29	0.84	0.86	0.17	0.23	0.03	0.08	
mPFC-L	0.21	0.34	0.77	0.73	0.36	0.55	0.46	0.02	0.53		
mPFC-R	0.12	0.23	0.54	0.99	0.24	0.46	0.24	0.61			
OFC-L	0.49	0.55	0.20	0.05	0.51	0.67	0.18				
OFC-R	0.31	0.20	0.26	0.13	0.23	0.45					
PaC-L	0.61	0.39	0.84	0.08	0.31						
PaC-R	0.74	0.59	0.83	0.11							
RSC-L	0.18	0.22	0.31								
RSC-R	0.75	0.65									
Hipp-L	0.67										

Table 10: *P* values of the FC changes. *P* values of the FC changes in regions of the SMN for rats with *mild* VMAT2 KD. Data were analyzed using paired t-tests. Table from [1].

Mild	Th-R	Th-L	SC-R	SC-L	MC-R	MC-L	STR-R
STR-L	0.13	0.06	0.21	0.14	0.23	0.21	0.39
STR-R	0.13	0.09	0.19	0.13	0.39	0.29	
MC-L	0.24	0.16	0.47	0.16	0.46		
MC-R	0.29	0.23	0.38	0.21			
SC-L	0.14	0.04	0.76				
SC-R	0.30	0.12					
Th-L	0.79						
Th-R							

Table 11: *P* values of the FC changes. *P* values of the FC changes in regions of the DMN for rats with *moderate* VMAT2 KD. Data were analyzed using paired t-tests. Table from [1].

Moderate	Hipp-R	Hipp-L	RSC-R	RSC-L	PaC-R	PaC-L	OFC-R	OFC-L	mPFC-R	mPFC-L	CgC-R
CgC-L	0.05	0.02	0.07	0.11	0.24	0.22	0.05	0.03	0.03	0.04	0.07
CgC-R	0.03	0.02	0.08	0.14	0.21	0.25	0.04	0.01	0.03	0.05	
mPFC-L	0.01	0.03	0.03	0.09	0.05	0.04	0.04	0.04	0.06		
mPFC-R	**0.005**	**0.007**	0.01	0.03	0.03	0.03	0.06	0.01			
OFC-L	0.08	0.10	0.04	0.13	0.24	0.21	0.05				
OFC-R	0.16	0.11	0.03	0.07	0.29	0.47					
PaC-L	0.35	0.60	0.03	0.10	0.13						
PaC-R	0.42	0.32	0.06	0.22							
RSC-L	0.10	0.07	0.02								
RSC-R	0.03	0.04									

Hipp-L	0.15										

Table 12: *P* values of the FC changes. *P* values of the FC changes in regions of the SMN for rats with *moderate* VMAT2 KD. Data were analyzed using paired t-tests. Table from [1].

Moderate	**Th-R**	**Th-L**	**SC-R**	**SC-L**	**MC-R**	**MC-L**	**STR-R**
STR-L	**0.01**	**0.004**	0.02	0.05	0.03	0.04	**0.007**
STR-R	0.02	**0.008**	0.06	0.04	0.16	0.07	
MC-L	0.04	0.01	0.10	0.08	0.04		
MC-R	0.02	0.02	0.07				
SC-L	**0.003**	**0.001**	0.11				
SC-R	0.02	**0.008**					
Th-L	0.07						
Th-R							

Table 13: *P* values of the FC changes. *P* values of the internetwork FC changes in regions of the DMN and SMN for rats with *mild* VMAT2 KD. Data were analyzed using paired t-tests. Table from [1].

Mild	**Hipp-R**	**Hipp-L**	**RSC-R**	**RSC-L**	**PaC-R**	**PaC-L**	**OFC-R**	**OFC-L**	**mPFC-R**	**mPFC-L**	**CgC-R**	**CgC-L**
STR-L	0.23	0.18	0.82	0.26	0.94	0.93	**0.006**	**0.005**	0.10	0.15	0.27	0.29
STR-R	0.16	0.44	0.65	0.32	0.65	0.98	**0.0004**	0.03	0.06	0.19	0.24	0.31
MC-L	0.34	0.39	0.92	0.29	0.93	0.94	0.11	0.40	0.02	0.04	0.10	0.07
MC-R	0.26	0.60	0.18	0.04	0.49	0.88	0.37	0.16	0.02	0.05	0.18	0.35
SC-L	0.12	0.26	0.78	0.05	0.87	0.46	**0.002**	0.02	0.03	0.05	0.13	0.17
SC-R	0.13	0.57	0.19	**0.006**	0.89	0.04	0.01	0.04	0.02	0.06	0.18	0.28
Th-L	0.35	0.27	0.55	0.39	1.00	0.89	0.09	0.21	0.11	0.17	0.14	0.17
Th-R	0.38	0.98	0.66	0.26	0.94	0.70	0.09	0.15	0.09	0.11	0.28	0.33

Table 14: *P* values of the FC changes. *P* values of the internetwork FC changes in regions of the DMN and SMN for rats with *moderate* VMAT2 KD. Data were analyzed using paired t-tests. Table from [1].

Moderate	**Hipp-R**	**Hipp-L**	**RSC-R**	**RSC-L**	**PaC-R**	**PaC-L**	**OFC-R**	**OFC-L**	**mPFC-R**	**mPFC-L**	**CgC-R**	**CgC-L**
STR-L	0.02	0.02	0.02	0.11	0.16	0.30	0.03	**0.003**	**0.006**	0.01	0.07	0.09
STR-R	0.08	0.08	0.04	0.14	0.30	0.63	**0.008**	0.01	**0.002**	**0.003**	0.04	0.07
MC-L	0.03	0.03	**0.003**	0.03	0.45	0.46	0.04	0.07	**0.003**	**0.003**	0.02	0.02
MC-R	0.03	0.05	0.05	0.18	0.52	0.97	0.19	**0.008**	**0.01**	**0.007**	0.03	0.03
SC-L	**0.004**	**0.008**	**0.008**	0.08	0.11	0.44	0.05	0.02	**0.003**	**0.004**	0.04	0.06
SC-R	0.02	0.08	0.06	0.35	0.27	0.94	0.07	0.04	**0.001**	**0.003**	0.04	0.07
Th-L	0.06	0.02	0.09	0.10	0.17	0.15	0.06	0.03	0.02	0.03	0.03	0.04
Th-R	0.03	0.10	0.09	0.23	0.15	0.13	0.14	0.08	0.02	0.04	0.07	0.15

3.2. Imaging exogenous gene expression in the rat brain

3.2.1 *In vivo* and *ex vivo* characterization of [^{11}C]TMP in the rat brain

3.2.1.1 *In vivo* PET imaging

In vivo PET studies were conducted to investigate the feasibility of using [^{11}C]TMP as a reporter gene probe in the rat brain. We observed very poor tracer uptake in the rats' striatum at baseline (SUV Baseline (mean ± SD): 0.15 ± 0.02) (Figure 33A,D). The co-administration with Sulfamethoxazole did not improve [^{11}C]TMP uptake in the striatum (SUV Sulfamethoxazole (mean ± SD): 0.13 ± 0.03) (Figure 33B,D). Instead, we observed ~ 46% increase of [^{11}C]TMP striatal uptake following the Pgp-blockade (SUV Elacridar (mean ± SD): 0.28 ± 0.09, ^{+}P= 0.04) (Figure 33C,D).

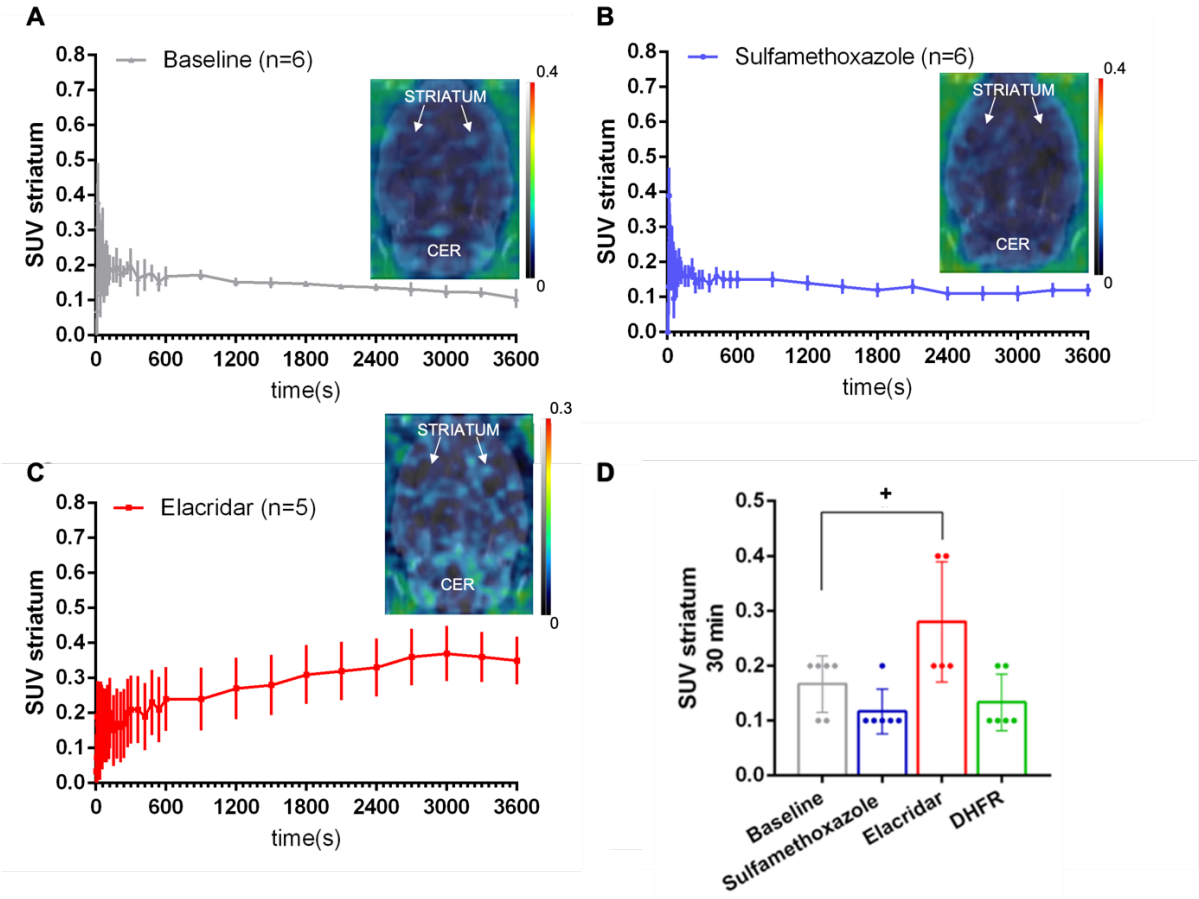

Figure 33: [^{11}C]TMP *in vivo* PET imaging. Radioactivity uptakes were decay corrected to the injection time and are expressed as the standardized uptake value (SUV), normalized for the injected radioactivity and rats' body weight. [^{11}C]TMP striatal SUVs (mean ± SD) and exemplary coronal PET images (sum of all frames) for rats scanned at baseline (A), after Sulfamethoxazole administration (B) and following PgP-blockade with Elacridar (3 mL/Kg) (C). D: SUVs (mean ± SD) values (0-30 min) of [^{11}C]TMP at baseline, with Sulfamethoxazole and Elacridar in the rats' striatum.

3.2.1.2 Biodistribution

Ex vivo biodistribution was performed 2 min, 15 min, and 45 min after [^{11}C]TMP injection. Brain, blood, and kidney were isolated from wild-type SD rats at the indicated time points (n= 3/group) and analyzed in a gamma counter. Our data revealed a high initial kidney uptake (SUV ~ 70%). [^{11}C]TMP was present in a minimal quote in the brain 2 min post-injection (SUV ~ 20%) and showed low retention by 15 – 45 min (SUV < 0.2%), supporting the *in vivo* imaging data. Similar [^{11}C]TMP uptake (SUV ~ 30%) was found in blood (Figure 34).

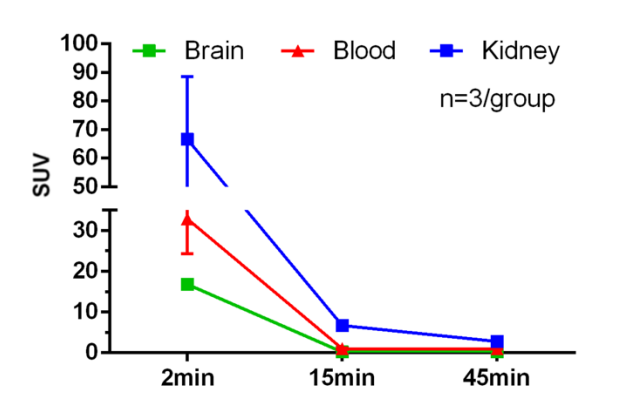

Figure 34: [^{11}C]TMP biodistribution. Radioactivity, expressed as the % of the standardized uptake value (SUV), normalized for the injected radioactivity, rats' body weight and mass of tissue samples (g) (mean ± SD), in the brain, blood, and kidney, collected 2 min, 15 min, and 45 min after [^{11}C]TMP injection, as measured in a gamma counter.

3.2.1.3 Metabolism

In Figure 35, results of the radio-HPLC analysis of blood and brain samples collected from wild-type SD rats (n= 1/group), 1 min, 5 min, and 10 min after [^{11}C]TMP administration are shown. The parent radioligand (Figure 35A) (t_R [^{11}C]TMP= 5 min) was not detected in blood and brain at 1 min after tracer injection (Figure 35B). 5 min post-injection, the parent compound and one metabolite ([^{11}C]A) were identified in the blood (t_R [^{11}C]A= 3.8 min, ~ 80%; t_R [^{11}C]TMP= 5 min, ~ 20%), however only the [^{11}C]A peak could be detected in the brain tissue ([^{11}C]A t_R= 3.8 min, ~ 40%), while the parent tracer was not detectable (Figure 35C). 10 min post-injection, the metablite [^{11}C]A was present in the blood (~ 95%) but undetectable in the brain (Figure 35D). The percentage of the parent compound [^{11}C]TMP rapidly decreased in blood during the first 10 min after the injection, as no parent compound (t_R= 5 min) could be detected

in the sample. Instead, the radioactive metabolite [^{11}C]A could still be found in the blood collected after 10 min (t_R= 3.8 min), with a quote of ~ 95% (Figure 35D).

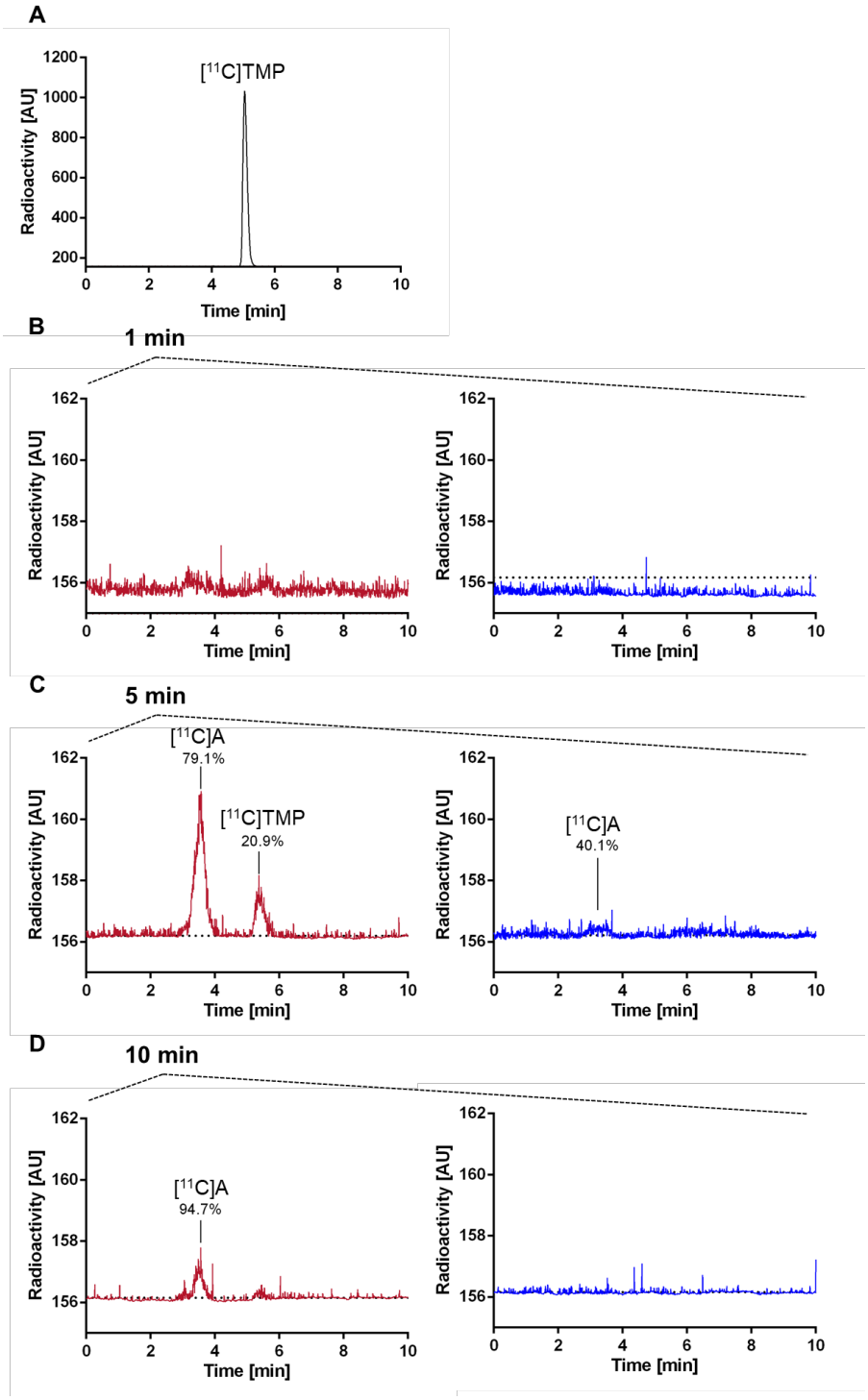

Figure 35: [^{11}C]TMP metabolism. A: HPLC standard of [^{11}C]TMP after tracer synthesis. Brain lysate (blue graphs) and serum (red graphs) were collected 1 min (B), 5 min (C), and 10 min (D) following [^{11}C]TMP injection andparent compound and metabolites in plasma and tissue were determined by radio-HPLC.

4 Discussion

This CRISPR/Cas9-brain imaging study *"highlights the feasibility and potential of combining CRISPR/Cas9 gene-editing with PET imaging to identify molecular adaptations in response to targeted gene modulations. Using CRISPR/SaCas9, we knocked down the Slc18a2 gene, encoding the VMAT2, which plays a key role in the storage and release of DA in response to neuronal activity [83]. The CRISPR/SaCas9-mediated KD allowed us to investigate the VMAT2-dependent DA signaling in the striatum while structurally preserving neuronal integrity. [^{18}F]GE-180 data suggested that glial activation is not the source of dopaminergic synaptic dysfunction and excluded the occurrence of inflammatory responses arising from the surgical procedure and the chosen AAV-serotype, in line with recent reports [151].*

Our study revealed that the targeted gene KD in the SNc leads to an expected reduction of DA release in the striatum, paralleled by [^{11}C]RAC binding changes. It is conceivable that the observed postsynaptic changes result from an increase in binding due to the reduced DA concentration in the striatum. Yet, several studies have revised this notion [259, 260]. In this regard, our results of the drug-evoked rotational behavior are in better agreement with a D2R compensatory upregulation. Indeed, supersensitivity to apomorphine in rats with nigrostriatal lesions or VMAT2 knockout is accompanied by an increase in striatal D2R binding sites but no change in affinity [261-266]. Further, the observed striatal increase in [^{11}C]RAC binding is independent of presynaptic nerve terminal loss and occurs in response to a ~ 20% decrease of [^{11}C]DTBZ binding. This confirms, in line with our [^{11}C]MP results, that [^{11}C]RAC can be used to delineate postsynaptic changes in the absence of DAT-mediated compensation triggered by neuronal loss. Accordingly, increased [^{11}C]RAC binding is observed in the early but not later stages of PD [267], characterized by severe neuronal cell loss and DAT changes (> 50%) [161]. Consistently, rats with severe denervation (> 75%) present earlier mitigation by the DAT, followed by D2R binding changes [159]. Hence, with our method, it is feasible to study the consequences of synaptic DA dysfunction without compensations triggered by neuronal cell loss. Moreover, the observed [^{11}C]RAC and [^{11}C]DTBZ correlations to the motor behavior highlight that

[^{11}C]RAC binding remains at control levels as long as synaptic DA levels are sufficient to maintain adequate motor function. Motor disturbances strongly correlate to pre and postsynaptic changes if movements of the forelimbs, but not whole-body, are considered, in agreement with earlier observations in DA-depleted rats [256]. VMAT2 KD reduced DA tissue levels in the ipsilateral striatum, nicely merging with the in vivo data. Moreover, metabolite analysis suggested that DA is quickly converted due to the lack of VMAT2-mediated storage in presynaptic vesicles. The increased metabolism might as well be a possible compensatory mechanism consequent to the VMAT2 KD, reflecting actions that residual nigrostriatal neurons undertake to maintain DA homeostasis, as already speculated by others [262, 268]. Further, by inducing a mild to moderate gene KD, we could investigate early to late rs brain network adaptations prompted by presynaptic dysfunction. We show that the selective impairment of presynaptic DA storage and release is followed by rs-FC alterations within and between the DMN and SMN. Our results confirm previous findings that the DMN, associated with ideation and mind wandering [235], and the SMN, involved in sensory processing and motor function [242], do not function in isolation from each other, but rather synchronize [269]. The observed internetwork synchronization may reflect compensatory brain reorganization, as already speculated by others [270, 271]. We also identified enhanced intranetwork rs-FC in the DMN and SMN. Rs-FC changes were observed in prefrontal cortical regions, hippocampus, thalamus, and striatum. Our data parallel previous findings of cortico-striato-thalamic hyperconnectivity in decreased DA transmission states [272-275]. In line, increased synchronous neural oscillatory activity and functional coupling in the basal ganglia and its associated networks have been observed in PD [276-281]. The increase of cortico-striatal FC could in part be due to dysfunctions of multiple tonic inhibitory gate actions of D2R [282]. Increased FC across the thalamus and prefrontal cortex has been reported in drug-treated PD patients [283, 284], potentially indicating functional compensation, as the brain recruits additional anatomical areas to aid in restoring cognitive processes. This might as well explain the engagement of the hippocampus, functionally connected with DMN cortical regions [285, 286]. In this

regard, research has shown that the hyperconnectivity of brain circuits is a common response to neurological dysfunction, and may reflect a protective mechanism to maintain normal brain functioning [287]. Such a mechanism has been proposed in PD, mild cognitive impairment, and AD [288-291]. Collectively, our findings support this model and indicate a reorganization of brain networks that adapt to the synaptic dysfunction through enhanced interregional synchrony. Recruiting alternative brain regions may be an early response to the dysfunction preceding neuronal cell loss and motor impairment. Interestingly, brain connectome adaptations occurred symmetrically in the DMN but were more weighted towards the contralateral hemisphere in the SMN" [1]. Our findings suggest that the lack of DA release due to VMAT2 KD is insufficient to induce cell loss or that this might develop over a longer time frame. Herewith, we speculate that the observed increase in D2R expression, together with the network-level functional adaptations and the metabolic outcome appears as a compensatory neurochemical and functional manifestation preceding neuronal cell loss. Yet, a longitudinal study that monitors these changes beyond our endpoint (19 weeks post-targeting) would be needed to confirm this hypothesis.

"We knocked down VMAT2 in dopaminergic projection neurons from the SNc to the dorsal striatum. To achieve selective targeting of this neuronal subtype, rat Cre driver lines have been developed [19, 292]. Although all monoamine-releasing neurons express VMAT2, in contrast to other brain regions, SNc neurons are predominantly dopaminergic [293]. Thus, even though we used wild-type rats, we can largely dismiss effects on other monoaminergic neurons, as also indicated by biochemical analysis of 5-HT striatal levels.

Despite its limited off-target editing [138], undesired targeting of SaCas9 on other genes cannot be entirely excluded. Nevertheless, off-target candidates with up to 4 mismatches were screened in the whole genome of Rattus norvegicus (http://www.rgenome.net/cas-offinder/), consistently with past reports [18]. To the best of our knowledge, the off-target matches (Ndrg1, RGD1305938, Btn2a2, AABR07042293.2) have no effects on VMAT2 function, being involved in cell differentiation, T-cell regulation, and mRNA processing, respectively (https://www.ncbi.nlm.nih.gov/IEB/Research/Acembly/index.html).

Another limitation of the study is the relatively small sample size, related to the complex and high-cost procedures involved in the in vivo imaging measurements. In addition to this, the differences in VMAT2 KD efficiency, contributed to the significant variance in our cohorts. Nevertheless, the variability of gene-editing efficiency was in line with previous in vivo brain studies [18, 143]" [1].

We show that CRISPR/Cas9 editing combined with multimodal *in vivo* imaging can be used to detect pathological features typical of mild or severe disease phenotypes. Indeed, it identifies stage-specific molecular and functional brain adaptations. Ultimately, our combinatorial approach has the potential to aid in the development of targeted therapies to restore physiological brain function. Further, our multimodal design can aid dissecting the pathogenic role of receptors, transporters, and ion channels playing a role in neurological diseases.

Future studies could profit from *in vivo* reporter gene PET probes to quantitatively assess and monitor the Cas9 and sgRNA brain expression over time [38, 220]. This would provide a quantitative measure of the gene expression differences between rats and would additionally allow a longitudinal examination of the gene expression. Despite several reporter genes have been developed in the last years, these show major limitations, which include f.e. endogenous expression in the brain, resulting in high background binding or low brain uptake [37-43]. Thus, our aim was to investigate the potential of [^{11}C]TMP as a novel PET reporter probe to image *Ec*DHFR-expressing cells in the rat brain. [^{11}C]TMP has shown great potential as reporter gene probe in xenografted tumor models [47], binding with very low affinity to the mammalian DHFR (4-fold less) and being biologically inert [47]. As no studies on [^{11}C]TMP suitability for brain imaging were perfomed in the rat, our aim was to investigate the [^{11}C]TMP brain pharmacokinetics and biodistribution in the species.

Our study proved the unsuitability of [^{11}C]TMP as a PET reporter gene probe in the rat brain. We conducted *in vivo* and *ex vivo* examinations to characterize [^{11}C]TMP uptake, pharmacokinetics and metabolism. [^{11}C]TMP highest SUV in the rat brain was about 7-fold lower the suitable values for brain imaging (SUV_{30min} ~ 0.2 *vs* > 1.5) [157], in line with a recent study performed in mice [210]. Further, we observed a significant enhancement in [^{11}C]TMP uptake following

PgP-blockade (SUV_{30min} 0.3 ± 0.1 *vs* 0.15 ± 0.1), suggesting dependency on the efflux pumps at the BBB that might have hampered the compound brain uptake. Strong efflux transporter dependency greatly reduces the concentration of radioligands within the brain, leading to negligible uptake [294, 295]. Similarly, [^{11}C]TMP analogs with improved pharmacokinetics show PgP-dependency in mice [210]. Of note, due to the higher PgP activity in rodents, several tracers perform poorly in rodent imaging studies compared to higher-order species [188]. Indeed, brain uptake discrepancies due to the PgP efflux transporter differences have been observed in the rat, pig, monkey, and human BBB [188, 296, 297].

Finally, our study revealed [^{11}C]TMP rapid *in vivo* metabolism hampering the tracer brain availability and producing a radiometabolite crossing the BBB. We observed that [^{11}C]TMP is metabolized to [^{11}C]A *in vivo* within 5 min, and that [^{11}C]A is predominant in blood and brain by 5 - 10 min. In the brain, the HPLC analytical findings at 5 min suggested that the *in vivo* PET data may mostly reflect the behavior of the radioactive metabolite [^{11}C]A rather than [^{11}C]TMP. Our data agree with a recent study from Shimojo *et al*., published after completion of our study, and performed in mice and non-human primates [210]. Similarly to what we observed, the authors showed limited brain uptake of [^{11}C]TMP and its analogs, potentially due to the dependency on PgP efflux transport at the BBB.

In conclusion, our data indicated unfavorable characteristics of [^{11}C]TMP and discouraged its use as a reporter gene probe in the rat brain. Future studies should focus on investigating different targets or developing [^{11}C]TMP analogs with more favorable brain pharmacokinetics and detectability, which are neither PgP substrate nor metabolized.

5. Summary

"Receptors, transporters and ion channels are important targets for therapy development in neurological diseases, [...] but their mechanistic role in pathogenesis is often poorly understood. Gene-editing and in vivo imaging approaches will help to identify the molecular and functional role of these targets and the consequence of their regional dysfunction on whole-brain level. Here, we combine CRISPR/Cas9 gene-editing with in vivo PET and fMRI to investigate the direct link between genes, molecules, and the brain connectome. The extensive knowledge of the Slc18a2 gene encoding the VMAT2, involved in the storage and release of DA, makes it an excellent target for studying the gene networks relationships while structurally preserving neuronal integrity and function. We edited the Slc18a2 in the SNc of adult rats and used in vivo molecular imaging besides behavioral, histological, and biochemical assessments to characterize the CRISPR/Cas9-mediated VMAT2 KD.

Simultaneous PET/fMRI was performed to inspect the molecular and functional brain adaptations, beyond the predicted dopaminergic changes.

We found a regional increase in postsynaptic DA receptor availability, preceded by a reorganization of brain networks that adapt to reduced DA transmission states by becoming functionally connected and organized. We observed that FC adaptations are stage-specific and *follow the selective impairment of presynaptic DA storage and release.* Further, the observed hyperconnectivity within and between brain networks spreads from the contralateral thalamus and prefrontal cortical regions to the striata and hippocampi.

Our study reveals that recruiting different brain networks is an early response to the dopaminergic dysfunction preceding neuronal cell loss. Our combinatorial approach is a novel tool to investigate the impact of specific genes on brain molecular and functional dynamics which will help to develop tailored therapies for normalizing brain function. The method can easily be transferred to higher-order species allowing for a direct comparison of the molecular imaging findings" [1].

Future studies could benefit from *in vivo* reporter gene PET probes to quantitatively assess and monitor the Cas9 and sgRNA brain expression over time [38, 220]. Indeed, *in vivo* reporter gene imaging is a powerful tool to monitor gene therapy and image exogenous gene expression in the brain of preclinical models of neurological diseases. Despite several reporter genes have been developed in the last years, these show major limitations. Indeed, most available reporter gene systems are based on endogenously expressed genes, resulting in high background binding or low brain uptake.

Here, we characterized the pharmacokinetics and metabolism of [^{11}C]TMP, a novel PET reporter probe which binds to *Ec*DHFR-engineered cells and shows potential for imaging ectopic gene expression in xenografted tumor models *in vitro* and *in vivo* [47].

We found that [^{11}C]TMP presents several unfavorable characteristics; dependency on PgP efflux transport at the BBB, hindering its brain uptake in the rat species, and *in vivo* metabolism, hampering the PET data quantification.

Our study shows that [^{11}C]TMP is not a suitable PET reporter gene probe to image exogeneous gene expression in the rat brain, presenting low brain uptake and fast metabolism.

Future studies should focus on the investigation of different targets and the development of [^{11}C]TMP analogs with more favorable pharmacokinetics and detectability, which are neither PgP substrate nor rapidely metabolized.

Signature of the Doctoral Thesis Supervisor

Prof.Dr.Kristina Herfert

6. German summary

Rezeptoren, Transporter und Ionenkanäle sind wichtige Zielstrukturen für die Entwicklung von Therapien bei neurologischen Erkrankungen, doch ist ihre mechanistische Rolle bei der Pathogenese oft nur unzureichend bekannt. Gen-Editierungen und *In-vivo*-Bildgebungsverfahren können dazu beitragen, die molekulare und funktionelle Rolle dieser Ziele und die Folgen ihrer regionalen Fehlfunktion auf der Ebene des gesamten Gehirns zu ermitteln. Hier kombinieren wir CRISPR/Cas9-Gen-Editing mit *In-vivo*-PET und -fMRI, um die direkte Verbindung zwischen Genen, Molekülen und dem Konnektom des Gehirns zu untersuchen. Das umfangreiche Wissen über das *Slc18a2*-Gen, das für den VMAT2 kodiert und an der Speicherung und Freisetzung von DA beteiligt ist, macht es zu einem ausgezeichneten Ziel für die Untersuchung der Beziehungen zwischen Gennetzwerken bei gleichzeitiger struktureller Erhaltung der neuronalen Integrität und Funktion. Wir haben das *Slc18a2*-Gen in der SNc erwachsener Ratten editiert und *in vivo* molekulare Bildgebung sowie verhaltensbiologische, histologische und biochemische Untersuchungen durchgeführt, um den CRISPR/Cas9-vermittelte VMAT2-KD zu charakterisieren. Es wurde eine gleichzeitige PET/fMRI-Untersuchung durchgeführt, um die molekularen und funktionellen Anpassungen des Gehirns zu untersuchen, die über die vorhergesagten dopaminergen Veränderungen hinausgehen. Wir fanden eine regionale Zunahme der postsynaptischen Dopamin-Rezeptorverfügbarkeit, der eine Reorganisation der Gehirnnetzwerke vorausging, die sich an die reduzierte Dopamin-Übertragung anpassen, indem sie funktionell verbunden und organisiert werden. Wir beobachteten, dass die Anpassungen der funktionellen Konnektivität stadienspezifisch sind und auf die selektive Beeinträchtigung der präsynaptischen DA-Speicherung und -Freisetzung folgen. Darüber hinaus breitete sich die beobachtete Hyperkonnektivität innerhalb und zwischen Gehirnnetzwerken vom kontralateralen Thalamus und den präfrontalen kortikalen Regionen bis zu den Striaten und dem Hippocampus aus. Unsere Studie zeigt, dass die Rekrutierung verschiedener Hirnnetzwerke eine frühe Reaktion auf die dopaminerge Dysfunktion ist, die dem neuronalen Zellverlust vorausgeht. Unser

kombinatorischer Ansatz ist ein neuartiges Instrument zur Untersuchung des Einflusses spezifischer Gene auf die molekulare und funktionelle Dynamik des Gehirns, was zur Entwicklung maßgeschneiderter Therapien zur Normalisierung der Gehirnfunktion beitragen wird [1]. Die Methode lässt sich leicht auf Arten höherer Ordnung übertragen, was einen direkten Vergleich der Ergebnisse der molekularen Bildgebung ermöglicht. Künftige Studien könnten von *In-vivo*-Reportergen-PET-Tracern profitieren, um die Cas9- und sgRNA-Expression im Gehirn im Laufe der Zeit quantitativ zu bewerten und zu überwachen [214, 224]. In der Tat ist die *In-vivo*-Reportergen-Bildgebung ein leistungsfähiges Instrument zur Überwachung der Gentherapie und zur Darstellung der exogenen Genexpression im Gehirn präklinischer Modelle neurologischer Erkrankungen. Obwohl in den letzten Jahren mehrere Reportergene entwickelt wurden, weisen diese erhebliche Einschränkungen auf. Die meisten verfügbaren Reportergensysteme basieren nämlich auf endogen exprimierten Genen, was zu einer hohen Hintergrundbindung oder einer geringen Aufnahme im Gehirn führt. Hier haben wir die Pharmakokinetik und den Stoffwechsel von [^{11}C]TMP charakterisiert, einem neuen PET-Reportergen-Tracer, der an EcDHFR gezüchtete Zellen bindet und das Potenzial hat, ektopische Genexpression in xenotransplantierten Tumormodellen *in vitro* und *in vivo* darzustellen [40]. Wir haben festgestellt, dass [^{11}C]TMP mehrere ungünstige Eigenschaften aufweist: Abhängigkeit vom PgP-Efflux-Transport an der BHS, was die Aufnahme im Gehirn der Ratte verhindert, und *In-vivo*-Metabolismus, der die Quantifizierung der PET-Daten erschwert. Unsere Studie zeigt, dass [^{11}C]TMP aufgrund der geringen Aufnahme ins Gehirn und des schnellen Metabolismus keine geeignete PET-Reportergen-Sonde für die Darstellung exogener Genexpression im Rattenhirn ist. Künftige Studien sollten sich auf die Untersuchung anderer Targets und die Entwicklung von [^{11}C]TMP-Analoga mit günstigerer Pharmakokinetik und Nachweisbarkeit konzentrieren, die weder PgP-Substrat sind noch schnell metabolisiert werden.

List of Publications

Research articles-first author

- Combining CRISPR/Cas9 and brain imaging: from genes to proteins to networks, *PNAS*, **2022 (**prev. published on bioRxiv: https://www.biorxiv.org/content/10.1101/2021.09.10.459766v3.full)

Research articles-co-author

- Universal Gene Correction Approaches for β-hemoglobinopathies Using CRISPR-Cas9 and Adeno-Associated Virus Serotype 6 Donor Templates, *The CRISPR Journal*, **2021**

- A consensus protocol for functional connectivity analysis in the rat brain, *Nature Neuroscience*, in press
-

Review-co-author

- Quantitative Rodent Brain Receptor Imaging, *Molecular Imaging and Biology*, **2020**

Book Chapter-co-author

- Preclinical Experimentation in Neurology, *Radiopharmaceutical Chemistry*, **2019**

EU Patent

- “Compound and method for the treatment of a VMAT2-associated disease”

Bibliography

1. Marciano, S., et al., *Combining CRISPR/Cas9 and brain imaging: from genes to molecules to networks.* BioRxiv, 2021.
2. Travis, J., *Making the cut.* Science, 2015. **350**(6267): p. 1456-7.
3. Sciences, T.R.S.A.o., *The Nobel Prize in Chemistry [Press release].*https://www.nobelprize.org/uploads/2020/10/press-chemistryprize2020.pdf. 2020.
4. Adli, M., *The CRISPR tool kit for genome editing and beyond.* Nat Commun, 2018. **9**(1): p. 1911.
5. Jinek, M., et al., *A programmable dual-RNA-guided DNA endonuclease in adaptive bacterial immunity.* Science, 2012. **337**(6096): p. 816-21.
6. Cong, L., et al., *Multiplex genome engineering using CRISPR/Cas systems.* Science, 2013. **339**(6121): p. 819-23.
7. Whitworth, K.M., et al., *Use of the CRISPR/Cas9 system to produce genetically engineered pigs from in vitro-derived oocytes and embryos.* Biol Reprod, 2014. **91**(3): p. 78.
8. Chen, Y., et al., *Functional disruption of the dystrophin gene in rhesus monkey using CRISPR/Cas9.* Hum Mol Genet, 2015. **24**(13): p. 3764-74.
9. Chang, N., et al., *Genome editing with RNA-guided Cas9 nuclease in zebrafish embryos.* Cell Res, 2013. **23**(4): p. 465-72.
10. Platt, R.J., et al., *CRISPR-Cas9 knockin mice for genome editing and cancer modeling.* Cell, 2014. **159**(2): p. 440-55.
11. Yu, Z., et al., *Highly efficient genome modifications mediated by CRISPR/Cas9 in Drosophila.* Genetics, 2013. **195**(1): p. 289-91.
12. Musunuru, K., et al., *In vivo CRISPR base editing of PCSK9 durably lowers cholesterol in primates.* Nature, 2021. **593**(7859): p. 429-434.
13. Swiech, L., et al., *In vivo interrogation of gene function in the mammalian brain using CRISPR-Cas9.* Nat Biotechnol, 2015. **33**(1): p. 102-6.
14. Demirci, S., N. Uchida, and J.F. Tisdale, *Gene therapy for sickle cell disease: An update.* Cytotherapy, 2018. **20**(7): p. 899-910.
15. Cai, B., et al., *Application of CRISPR/Cas9 technologies combined with iPSCs in the study and treatment of retinal degenerative diseases.* Hum Genet, 2018. **137**(9): p. 679-688.
16. Lu, Y., et al., *Safety and feasibility of CRISPR-edited T cells in patients with refractory non-small-cell lung cancer.* Nat Med, 2020. **26**(5): p. 732-740.
17. Zimmer, E.R., et al., *MicroPET imaging and transgenic models: a blueprint for Alzheimer's disease clinical research.* Trends Neurosci, 2014. **37**(11): p. 629-41.
18. Sun, H., et al., *Development of a CRISPR-SaCas9 system for projection- and function-specific gene editing in the rat brain.* Sci Adv, 2020. **6**(12): p. eaay6687.
19. Back, S., et al., *Neuron-Specific Genome Modification in the Adult Rat Brain Using CRISPR-Cas9 Transgenic Rats.* Neuron, 2019.
20. Shen, L.H., M.H. Liao, and Y.C. Tseng, *Recent advances in imaging of dopaminergic neurons for evaluation of neuropsychiatric disorders.* J Biomed Biotechnol, 2012. **2012**: p. 259349.
21. Finnema, S.J., et al., *Application of cross-species PET imaging to assess neurotransmitter release in brain.* Psychopharmacology (Berl), 2015. **232**(21-22): p. 4129-57.
22. Jorgensen, L.M., et al., *Cerebral 5-HT release correlates with [(11)C]Cimbi36 PET measures of 5-HT2A receptor occupancy in the pig brain.* J Cereb Blood Flow Metab, 2017. **37**(2): p. 425-434.

23. Phan, J.A., et al., *Quantification of [(11)C]yohimbine binding to alpha2 adrenoceptors in rat brain in vivo.* J Cereb Blood Flow Metab, 2015. **35**(3): p. 501-11.
24. Buiter, H.J., et al., *[11C]AF150(S), an agonist PET ligand for M1 muscarinic acetylcholine receptors.* EJNMMI Res, 2013. **3**(1): p. 19.
25. Frankle, W.G., et al., *[11C]flumazenil binding is increased in a dose-dependent manner with tiagabine-induced elevations in GABA levels.* PLoS One, 2012. **7**(2): p. e32443.
26. van der Doef, T.F., et al., *Quantification of the novel N-methyl-d-aspartate receptor ligand [11C]GMOM in man.* J Cereb Blood Flow Metab, 2016. **36**(6): p. 1111-21.
27. Ding, Y.S., et al., *Pharmacokinetics and in vivo specificity of [11C]dl-threo-methylphenidate for the presynaptic dopaminergic neuron.* Synapse, 1994. **18**(2): p. 152-60.
28. Ogawa, S., et al., *Brain magnetic resonance imaging with contrast dependent on blood oxygenation.* Proc Natl Acad Sci U S A, 1990. **87**(24): p. 9868-72.
29. Biswal, B., et al., *Functional connectivity in the motor cortex of resting human brain using echo-planar MRI.* Magn Reson Med, 1995. **34**(4): p. 537-41.
30. Roffman, J.L., et al., *Dopamine D1 signaling organizes network dynamics underlying working memory.* Science advances, 2016. **2**(6): p. e1501672-e1501672.
31. McCutcheon, R.A., et al., *Mesolimbic Dopamine Function Is Related to Salience Network Connectivity: An Integrative Positron Emission Tomography and Magnetic Resonance Study.* Biol Psychiatry, 2019. **85**(5): p. 368-378.
32. Nagano-Saito, A., et al., *Posterior dopamine D2/3 receptors and brain network functional connectivity.* Synapse, 2017. **71**(11).
33. Hahn, A., et al., *Differential modulation of the default mode network via serotonin-1A receptors.* Proc Natl Acad Sci U S A, 2012. **109**(7): p. 2619-24.
34. Vidal, B., et al., *In vivo biased agonism at 5-HT(1A) receptors: characterisation by simultaneous PET/MR imaging.* Neuropsychopharmacology, 2018. **43**(11): p. 2310-2319.
35. Shiyam Sundar, L.K., et al., *Fully Integrated PET/MR Imaging for the Assessment of the Relationship Between Functional Connectivity and Glucose Metabolic Rate.* Front Neurosci, 2020. **14**: p. 252.
36. Sander, C.Y., et al., *Imaging Agonist-Induced D2/D3 Receptor Desensitization and Internalization In Vivo with PET/fMRI.* Neuropsychopharmacology, 2016. **41**(5): p. 1427-36.
37. Liang, Q., et al., *Noninvasive, quantitative imaging in living animals of a mutant dopamine D2 receptor reporter gene in which ligand binding is uncoupled from signal transduction.* Gene Ther, 2001. **8**(19): p. 1490-8.
38. Gambhir, S.S., et al., *Imaging adenoviral-directed reporter gene expression in living animals with positron emission tomography.* Proc Natl Acad Sci U S A, 1999. **96**(5): p. 2333-8.
39. MacLaren, D.C., et al., *Repetitive, non-invasive imaging of the dopamine D2 receptor as a reporter gene in living animals.* Gene Ther, 1999. **6**(5): p. 785-91.
40. Yoon, S.Y., et al., *Quantitative, noninvasive, in vivo longitudinal monitoring of gene expression in the brain by co-AAV transduction with a PET reporter gene.* Mol Ther Methods Clin Dev, 2014. **1**: p. 14016.
41. Maresz, K., et al., *Modulation of the cannabinoid CB2 receptor in microglial cells in response to inflammatory stimuli.* J Neurochem, 2005. **95**(2): p. 437-45.
42. Yaghoubi, S.S., et al., *Noninvasive detection of therapeutic cytolytic T cells with 18F-FHBG PET in a patient with glioma.* Nat Clin Pract Oncol, 2009. **6**(1): p. 53-8.
43. Vandeputte, C., et al., *A PET brain reporter gene system based on type 2 cannabinoid receptors.* J Nucl Med, 2011. **52**(7): p. 1102-9.

44. Iwamoto, M., et al., *A general chemical method to regulate protein stability in the mammalian central nervous system.* Chem Biol, 2010. **17**(9): p. 981-8.
45. Tai, K., et al., *Destabilizing domains mediate reversible transgene expression in the brain.* PLoS One, 2012. **7**(9): p. e46269.
46. Quintino, L., et al., *Functional neuroprotection and efficient regulation of GDNF using destabilizing domains in a rodent model of Parkinson's disease.* Mol Ther, 2013. **21**(12): p. 2169-80.
47. Sellmyer, M.A., et al., *Quantitative PET Reporter Gene Imaging with [(11)C]Trimethoprim.* Mol Ther, 2017. **25**(1): p. 120-126.
48. Abi-Dargham, A., et al., *Increased striatal dopamine transmission in schizophrenia: confirmation in a second cohort.* Am J Psychiatry, 1998. **155**(6): p. 761-7.
49. Charvin, D., et al., *Unraveling a role for dopamine in Huntington's disease: the dual role of reactive oxygen species and D2 receptor stimulation.* Proc Natl Acad Sci U S A, 2005. **102**(34): p. 12218-23.
50. Dubol, M., et al., *Lower midbrain dopamine transporter availability in depressed patients: Report from high-resolution PET imaging.* J Affect Disord, 2020. **262**: p. 273-277.
51. Ginovart, N., et al., *PET study of the pre- and post-synaptic dopaminergic markers for the neurodegenerative process in Huntington's disease.* Brain, 1997. **120 (Pt 3)**: p. 503-14.
52. Laruelle, M., et al., *Increased dopamine transmission in schizophrenia: relationship to illness phases.* Biol Psychiatry, 1999. **46**(1): p. 56-72.
53. Pearlson, G.D., et al., *In vivo D2 dopamine receptor density in psychotic and nonpsychotic patients with bipolar disorder.* Arch Gen Psychiatry, 1995. **52**(6): p. 471-7.
54. Spencer, T.J., et al., *Further evidence of dopamine transporter dysregulation in ADHD: a controlled PET imaging study using altropane.* Biol Psychiatry, 2007. **62**(9): p. 1059-61.
55. Volkow, N.D., et al., *Imaging endogenous dopamine competition with [11C]raclopride in the human brain.* Synapse, 1994. **16**(4): p. 255-62.
56. Laruelle, M., *Imaging synaptic neurotransmission with in vivo binding competition techniques: a critical review.* J Cereb Blood Flow Metab, 2000. **20**(3): p. 423-51.
57. Patel, V.D., et al., *Imaging dopamine release with Positron Emission Tomography (PET) and (11)C-raclopride in freely moving animals.* Neuroimage, 2008. **41**(3): p. 1051-66.
58. Yoon, J.H., et al., *Impaired prefrontal-basal ganglia functional connectivity and substantia nigra hyperactivity in schizophrenia.* Biol Psychiatry, 2013. **74**(2): p. 122-9.
59. Lodge, D.J. and A.A. Grace, *Hippocampal dysregulation of dopamine system function and the pathophysiology of schizophrenia.* Trends Pharmacol Sci, 2011. **32**(9): p. 507-13.
60. Perez-Costas, E., M. Melendez-Ferro, and R.C. Roberts, *Basal ganglia pathology in schizophrenia: dopamine connections and anomalies.* J Neurochem, 2010. **113**(2): p. 287-302.
61. Elsworth, J.D. and R.H. Roth, *Dopamine synthesis, uptake, metabolism, and receptors: relevance to gene therapy of Parkinson's disease.* Exp Neurol, 1997. **144**(1): p. 4-9.
62. Hastings, T.G., D.A. Lewis, and M.J. Zigmond, *Role of oxidation in the neurotoxic effects of intrastriatal dopamine injections.* Proc Natl Acad Sci U S A, 1996. **93**(5): p. 1956-61.
63. Sulzer, D., *Multiple hit hypotheses for dopamine neuron loss in Parkinson's disease.* Trends Neurosci, 2007. **30**(5): p. 244-50.
64. Eisenhofer, G., I.J. Kopin, and D.S. Goldstein, *Catecholamine metabolism: a contemporary view with implications for physiology and medicine.* Pharmacol Rev, 2004. **56**(3): p. 331-49.

65. da Silva Alves, F., et al., *The revised dopamine hypothesis of schizophrenia: evidence from pharmacological MRI studies with atypical antipsychotic medication.* Psychopharmacol Bull, 2008. **41**(1): p. 121-32.
66. Walter, H., et al., *Altered reward functions in patients on atypical antipsychotic medication in line with the revised dopamine hypothesis of schizophrenia.* Psychopharmacology (Berl), 2009. **206**(1): p. 121-32.
67. Pogarell, O., et al., *Dopaminergic neurotransmission in patients with schizophrenia in relation to positive and negative symptoms.* Pharmacopsychiatry, 2012. **45 Suppl 1**: p. S36-41.
68. Patel, N.H., et al., *Positron emission tomography in schizophrenia: a new perspective.* J Nucl Med, 2010. **51**(4): p. 511-20.
69. Maj, J., K. Wedzony, and V. Klimek, *Desipramine given repeatedly enhances behavioural effects of dopamine and d-amphetamine injected into the nucleus accumbens.* Eur J Pharmacol, 1987. **140**(2): p. 179-85.
70. Plaznik, A. and W. Kostowski, *The effects of antidepressants and electroconvulsive shocks on the functioning of the mesolimbic dopaminergic system: a behavioral study.* Eur J Pharmacol, 1987. **135**(3): p. 389-96.
71. Durlach-Misteli, C. and J.M. Van Ree, *Dopamine and melatonin in the nucleus accumbens may be implicated in the mode of action of antidepressant drugs.* Eur J Pharmacol, 1992. **217**(1): p. 15-21.
72. D'Haenen H, A. and A. Bossuyt, *Dopamine D2 receptors in depression measured with single photon emission computed tomography.* Biol Psychiatry, 1994. **35**(2): p. 128-32.
73. Takakusaki, K., et al., *Basal ganglia efferents to the brainstem centers controlling postural muscle tone and locomotion: a new concept for understanding motor disorders in basal ganglia dysfunction.* Neuroscience, 2003. **119**(1): p. 293-308.
74. de la Fuente-Fernandez, R., et al., *Levodopa-induced changes in synaptic dopamine levels increase with progression of Parkinson's disease: implications for dyskinesias.* Brain, 2004. **127**(Pt 12): p. 2747-54.
75. de la Fuente-Fernandez, R., et al., *Biochemical variations in the synaptic level of dopamine precede motor fluctuations in Parkinson's disease: PET evidence of increased dopamine turnover.* Ann Neurol, 2001. **49**(3): p. 298-303.
76. Bezard, E., et al., *Relationship between the appearance of symptoms and the level of nigrostriatal degeneration in a progressive 1-methyl-4-phenyl-1,2,3,6-tetrahydropyridine-lesioned macaque model of Parkinson's disease.* J Neurosci, 2001. **21**(17): p. 6853-61.
77. Fearnley, J.M. and A.J. Lees, *Striatonigral degeneration. A clinicopathological study.* Brain, 1990. **113 (Pt 6)**: p. 1823-42.
78. Nirenberg, M.J., et al., *Ultrastructural localization of the vesicular monoamine transporter 2 in mesolimbic and nigrostriatal dopaminergic neurons.* Adv Pharmacol, 1998. **42**: p. 240-3.
79. Tritsch, N.X., J.B. Ding, and B.L. Sabatini, *Dopaminergic neurons inhibit striatal output through non-canonical release of GABA.* Nature, 2012. **490**(7419): p. 262-6.
80. Tritsch, N.X., et al., *Midbrain dopamine neurons sustain inhibitory transmission using plasma membrane uptake of GABA, not synthesis.* Elife, 2014. **3**: p. e01936.
81. Rudnick, G., *ATP-driven H+ pumping into intracellular organelles.* Annu Rev Physiol, 1986. **48**: p. 403-13.
82. Guillot, T.S. and G.W. Miller, *Protective actions of the vesicular monoamine transporter 2 (VMAT2) in monoaminergic neurons.* Mol Neurobiol, 2009. **39**(2): p. 149-70.
83. Liu, Y. and R.H. Edwards, *The role of vesicular transport proteins in synaptic transmission and neural degeneration.* Annu Rev Neurosci, 1997. **20**: p. 125-56.

84. Jenner, P., *Oxidative stress in Parkinson's disease.* Ann Neurol, 2003. **53 Suppl 3**: p. S26-36; discussion S36-8.
85. Lohr, K.M., et al., *Increased vesicular monoamine transporter enhances dopamine release and opposes Parkinson disease-related neurodegeneration in vivo.* Proc Natl Acad Sci U S A, 2014. **111**(27): p. 9977-82.
86. Pifl, C., et al., *Is Parkinson's disease a vesicular dopamine storage disorder? Evidence from a study in isolated synaptic vesicles of human and nonhuman primate striatum.* J Neurosci, 2014. **34**(24): p. 8210-8.
87. Glatt, C.E., et al., *Gain-of-function haplotypes in the vesicular monoamine transporter promoter are protective for Parkinson disease in women.* Hum Mol Genet, 2006. **15**(2): p. 299-305.
88. Brighina, L., et al., *Analysis of vesicular monoamine transporter 2 polymorphisms in Parkinson's disease.* Neurobiol Aging, 2013. **34**(6): p. 1712 e9-13.
89. Rilstone, J.J., R.A. Alkhater, and B.A. Minassian, *Brain dopamine-serotonin vesicular transport disease and its treatment.* N Engl J Med, 2013. **368**(6): p. 543-50.
90. Howes, O.D., et al., *Elevated striatal dopamine function linked to prodromal signs of schizophrenia.* Arch Gen Psychiatry, 2009. **66**(1): p. 13-20.
91. O'Daly, O.G., et al., *Functional magnetic resonance imaging investigation of the amphetamine sensitization model of schizophrenia in healthy male volunteers.* Arch Gen Psychiatry, 2011. **68**(6): p. 545-54.
92. Simons, C.J., R. van Winkel, and Group, *Intermediate phenotype analysis of patients, unaffected siblings, and healthy controls identifies VMAT2 as a candidate gene for psychotic disorder and neurocognition.* Schizophr Bull, 2013. **39**(4): p. 848-56.
93. Zubieta, J.K., et al., *Vesicular monoamine transporter concentrations in bipolar disorder type I, schizophrenia, and healthy subjects.* Biol Psychiatry, 2001. **49**(2): p. 110-6.
94. Takahashi, N., et al., *VMAT2 knockout mice: heterozygotes display reduced amphetamine-conditioned reward, enhanced amphetamine locomotion, and enhanced MPTP toxicity.* Proc Natl Acad Sci U S A, 1997. **94**(18): p. 9938-43.
95. Fon, E.A., et al., *Vesicular transport regulates monoamine storage and release but is not essential for amphetamine action.* Neuron, 1997. **19**(6): p. 1271-83.
96. Mooslehner, K.A., et al., *Mice with very low expression of the vesicular monoamine transporter 2 gene survive into adulthood: potential mouse model for parkinsonism.* Mol Cell Biol, 2001. **21**(16): p. 5321-31.
97. Caudle, W.M., et al., *Reduced vesicular storage of dopamine causes progressive nigrostriatal neurodegeneration.* J Neurosci, 2007. **27**(30): p. 8138-48.
98. Taylor, T.N., et al., *Nonmotor symptoms of Parkinson's disease revealed in an animal model with reduced monoamine storage capacity.* J Neurosci, 2009. **29**(25): p. 8103-13.
99. Perel, P., et al., *Comparison of treatment effects between animal experiments and clinical trials: systematic review.* BMJ, 2007. **334**(7586): p. 197.
100. Boettcher, M. and M.T. McManus, *Choosing the Right Tool for the Job: RNAi, TALEN, or CRISPR.* Mol Cell, 2015. **58**(4): p. 575-85.
101. Zhou, X., et al., *Generation of CRISPR/Cas9-mediated gene-targeted pigs via somatic cell nuclear transfer.* Cell Mol Life Sci, 2015. **72**(6): p. 1175-84.
102. Hruscha, A., et al., *Efficient CRISPR/Cas9 genome editing with low off-target effects in zebrafish.* Development, 2013. **140**(24): p. 4982-7.
103. Yang, H., H. Wang, and R. Jaenisch, *Generating genetically modified mice using CRISPR/Cas-mediated genome engineering.* Nat Protoc, 2014. **9**(8): p. 1956-68.
104. Ran, F.A., et al., *Genome engineering using the CRISPR-Cas9 system.* Nat Protoc, 2013. **8**(11): p. 2281-2308.

105. Heyer, W.D., K.T. Ehmsen, and J. Liu, *Regulation of homologous recombination in eukaryotes.* Annu Rev Genet, 2010. **44**: p. 113-39.
106. Saleh-Gohari, N. and T. Helleday, *Conservative homologous recombination preferentially repairs DNA double-strand breaks in the S phase of the cell cycle in human cells.* Nucleic Acids Res, 2004. **32**(12): p. 3683-8.
107. Long, C., et al., *Postnatal genome editing partially restores dystrophin expression in a mouse model of muscular dystrophy.* Science, 2016. **351**(6271): p. 400-3.
108. Nelson, C.E., et al., *In vivo genome editing improves muscle function in a mouse model of Duchenne muscular dystrophy.* Science, 2016. **351**(6271): p. 403-7.
109. Tabebordbar, M., et al., *In vivo gene editing in dystrophic mouse muscle and muscle stem cells.* Science, 2016. **351**(6271): p. 407-411.
110. Jiang, W., et al., *RNA-guided editing of bacterial genomes using CRISPR-Cas systems.* Nat Biotechnol, 2013. **31**(3): p. 233-9.
111. Jiang, W., et al., *Demonstration of CRISPR/Cas9/sgRNA-mediated targeted gene modification in Arabidopsis, tobacco, sorghum and rice.* Nucleic Acids Res, 2013. **41**(20): p. e188.
112. Miao, J., et al., *Targeted mutagenesis in rice using CRISPR-Cas system.* Cell Res, 2013. **23**(10): p. 1233-6.
113. Bao, A., et al., *The CRISPR/Cas9 system and its applications in crop genome editing.* Crit Rev Biotechnol, 2019. **39**(3): p. 321-336.
114. Polstein, L.R. and C.A. Gersbach, *A light-inducible CRISPR-Cas9 system for control of endogenous gene activation.* Nat Chem Biol, 2015. **11**(3): p. 198-200.
115. Qi, L.S., et al., *Repurposing CRISPR as an RNA-guided platform for sequence-specific control of gene expression.* Cell, 2013. **152**(5): p. 1173-83.
116. Larson, M.H., et al., *CRISPR interference (CRISPRi) for sequence-specific control of gene expression.* Nat Protoc, 2013. **8**(11): p. 2180-96.
117. Zheng, Y., et al., *CRISPR interference-based specific and efficient gene inactivation in the brain.* Nat Neurosci, 2018. **21**(3): p. 447-454.
118. Ma, H., et al., *Multiplexed labeling of genomic loci with dCas9 and engineered sgRNAs using CRISPRainbow.* Nat Biotechnol, 2016. **34**(5): p. 528-30.
119. Pulecio, J., et al., *CRISPR/Cas9-Based Engineering of the Epigenome.* Cell Stem Cell, 2017. **21**(4): p. 431-447.
120. Konermann, S., et al., *Transcriptome Engineering with RNA-Targeting Type VI-D CRISPR Effectors.* Cell, 2018. **173**(3): p. 665-676 e14.
121. Cox, D.B.T., et al., *RNA editing with CRISPR-Cas13.* Science, 2017. **358**(6366): p. 1019-1027.
122. Campa, C.C., et al., *Multiplexed genome engineering by Cas12a and CRISPR arrays encoded on single transcripts.* Nat Methods, 2019. **16**(9): p. 887-893.
123. Gaudelli, N.M., et al., *Programmable base editing of A*T to G*C in genomic DNA without DNA cleavage.* Nature, 2017. **551**(7681): p. 464-471.
124. Fu, Y.F., et al., *High-frequency off-target mutagenesis induced by CRISPR-Cas nucleases in human cells.* Nature Biotechnology, 2013. **31**(9): p. 822-+.
125. Haeussler, M., et al., *Evaluation of off-target and on-target scoring algorithms and integration into the guide RNA selection tool CRISPOR.* Genome Biol, 2016. **17**(1): p. 148.
126. Ran, F.A., et al., *Double nicking by RNA-guided CRISPR Cas9 for enhanced genome editing specificity.* Cell, 2013. **154**(6): p. 1380-9.
127. Fu, Y., et al., *Improving CRISPR-Cas nuclease specificity using truncated guide RNAs.* Nat Biotechnol, 2014. **32**(3): p. 279-284.
128. Davis, K.M., et al., *Small molecule-triggered Cas9 protein with improved genome-editing specificity.* Nat Chem Biol, 2015. **11**(5): p. 316-8.

129. Pawluk, A., et al., *Inactivation of CRISPR-Cas systems by anti-CRISPR proteins in diverse bacterial species.* Nat Microbiol, 2016. **1**(8): p. 16085.
130. Charlesworth, C.T., et al., *Identification of preexisting adaptive immunity to Cas9 proteins in humans.* Nat Med, 2019. **25**(2): p. 249-254.
131. Kouranova, E., et al., *CRISPRs for Optimal Targeting: Delivery of CRISPR Components as DNA, RNA, and Protein into Cultured Cells and Single-Cell Embryos.* Hum Gene Ther, 2016. **27**(6): p. 464-75.
132. Kim, S., et al., *Highly efficient RNA-guided genome editing in human cells via delivery of purified Cas9 ribonucleoproteins.* Genome Res, 2014. **24**(6): p. 1012-9.
133. Lee, B., et al., *Nanoparticle delivery of CRISPR into the brain rescues a mouse model of fragile X syndrome from exaggerated repetitive behaviours.* Nat Biomed Eng, 2018. **2**(7): p. 497-507.
134. de Solis, C.A., et al., *The Development of a Viral Mediated CRISPR/Cas9 System with Doxycycline Dependent gRNA Expression for Inducible In vitro and In vivo Genome Editing.* Front Mol Neurosci, 2016. **9**: p. 70.
135. Chow, R.D., et al., *AAV-mediated direct in vivo CRISPR screen identifies functional suppressors in glioblastoma.* Nat Neurosci, 2017. **20**(10): p. 1329-1341.
136. Wu, Z., H. Yang, and P. Colosi, *Effect of genome size on AAV vector packaging.* Mol Ther, 2010. **18**(1): p. 80-6.
137. Nishimasu, H., et al., *Crystal Structure of Staphylococcus aureus Cas9.* Cell, 2015. **162**(5): p. 1113-26.
138. Ran, F.A., et al., *In vivo genome editing using Staphylococcus aureus Cas9.* Nature, 2015. **520**(7546): p. 186-91.
139. Kim, E., et al., *In vivo genome editing with a small Cas9 orthologue derived from Campylobacter jejuni.* Nat Commun, 2017. **8**: p. 14500.
140. Esvelt, K.M., et al., *Orthogonal Cas9 proteins for RNA-guided gene regulation and editing.* Nat Methods, 2013. **10**(11): p. 1116-21.
141. Kleinstiver, B.P., et al., *Engineered CRISPR-Cas9 nucleases with altered PAM specificities.* Nature, 2015. **523**(7561): p. 481-5.
142. Friedland, A.E., et al., *Characterization of Staphylococcus aureus Cas9: a smaller Cas9 for all-in-one adeno-associated virus delivery and paired nickase applications.* Genome Biol, 2015. **16**: p. 257.
143. Kumar, N., et al., *The Development of an AAV-Based CRISPR SaCas9 Genome Editing System That Can Be Delivered to Neurons in vivo and Regulated via Doxycycline and Cre-Recombinase.* Front Mol Neurosci, 2018. **11**: p. 413.
144. Hunker, A.C., et al., *Conditional Single Vector CRISPR/SaCas9 Viruses for Efficient Mutagenesis in the Adult Mouse Nervous System.* Cell Rep, 2020. **30**(12): p. 4303-4316 e6.
145. Burger, C., et al., *Recombinant AAV viral vectors pseudotyped with viral capsids from serotypes 1, 2, and 5 display differential efficiency and cell tropism after delivery to different regions of the central nervous system.* Mol Ther, 2004. **10**(2): p. 302-17.
146. Van der Perren, A., et al., *Efficient and stable transduction of dopaminergic neurons in rat substantia nigra by rAAV 2/1, 2/2, 2/5, 2/6.2, 2/7, 2/8 and 2/9.* Gene Ther, 2011. **18**(5): p. 517-27.
147. Dayton, R.D., M.S. Grames, and R.L. Klein, *More expansive gene transfer to the rat CNS: AAV PHP.EB vector dose-response and comparison to AAV PHP.B.* Gene Ther, 2018. **25**(5): p. 392-400.
148. Chan, K.Y., et al., *Engineered AAVs for efficient noninvasive gene delivery to the central and peripheral nervous systems.* Nat Neurosci, 2017. **20**(8): p. 1172-1179.

149. Deverman, B.E., et al., *Cre-dependent selection yields AAV variants for widespread gene transfer to the adult brain.* Nat Biotechnol, 2016. **34**(2): p. 204-9.
150. Seo, J.W., et al., *Positron emission tomography imaging of novel AAV capsids maps rapid brain accumulation.* Nat Commun, 2020. **11**(1): p. 2102.
151. Chatterjee, D., et al., *Enhanced CNS transduction from AAV.PHP.eB infusion into the cisterna magna of older adult rats compared to AAV9.* Gene Ther, 2021.
152. Jackson, K.L., et al., *Better Targeting, Better Efficiency for Wide-Scale Neuronal Transduction with the Synapsin Promoter and AAV-PHP.B.* Front Mol Neurosci, 2016. **9**: p. 116.
153. Hordeaux, J., et al., *The Neurotropic Properties of AAV-PHP.B Are Limited to C57BL/6J Mice.* Mol Ther, 2018. **26**(3): p. 664-668.
154. Meikle S.R., B.R.D., *Quantitative Techniques in PET*, in *Positron Emission Tomography*, T.D.W. Bailey D.L., Valk P.E., Maisey M.N., Editor. 2005, Springer: London.
155. Goertzen, A.L., et al., *NEMA NU 4-2008 comparison of preclinical PET imaging systems.* J Nucl Med, 2012. **53**(8): p. 1300-9.
156. Chatziioannou, A., et al., *Comparison of 3-D maximum a posteriori and filtered backprojection algorithms for high-resolution animal imaging with microPET.* IEEE Trans Med Imaging, 2000. **19**(5): p. 507-12.
157. Herfert, K., et al., *Preclinical Experimentation in Neurology.* Radiopharmaceutical Chemistry, 2019.
158. Booij, J., L.K. Teune, and H.J. Verberne, *The role of molecular imaging in the differential diagnosis of parkinsonism.* Q J Nucl Med Mol Imaging, 2012. **56**(1): p. 17-26.
159. Sossi, V., et al., *Dopamine transporter relation to levodopa-derived synaptic dopamine in a rat model of Parkinson's: an in vivo imaging study.* J Neurochem, 2009. **109**(1): p. 85-92.
160. Sossi, V., et al., *In vivo measurement of density and affinity of the monoamine vesicular transporter in a unilateral 6-hydroxydopamine rat model of PD.* J Cereb Blood Flow Metab, 2007. **27**(7): p. 1407-15.
161. Kraemmer, J., et al., *Correlation of striatal dopamine transporter imaging with post mortem substantia nigra cell counts.* Mov Disord, 2014. **29**(14): p. 1767-73.
162. Tang, J., et al., *PET imaging with [(18)F]FP-(+)-DTBZ in 6-OHDA-induced partial and full unilaterally-lesioned model rats of Parkinson's disease and the correlations to the biological data.* Nucl Med Biol, 2020. **90-91**: p. 1-9.
163. Weng, C.C., et al., *[(18)F]FP-(+)-DTBZ PET study in a lactacystin-treated rat model of Parkinson disease.* Ann Nucl Med, 2017. **31**(7): p. 506-513.
164. Albin, R.L., et al., *Increased ventral striatal monoaminergic innervation in Tourette syndrome.* Neurology, 2003. **61**(3): p. 310-5.
165. Tinazzi, M., et al., *Imaging of the dopamine transporter predicts pattern of disease progression and response to levodopa in patients with schizophrenia and parkinsonism: a 2-year follow-up multicenter study.* Schizophr Res, 2014. **152**(2-3): p. 344-9.
166. Sekiguchi, H., G. Pavey, and B. Dean, *Altered levels of dopamine transporter in the frontal pole and dorsal striatum in schizophrenia.* NPJ Schizophr, 2019. **5**(1): p. 20.
167. Taylor, S.F., et al., *In vivo measurement of the vesicular monoamine transporter in schizophrenia.* Neuropsychopharmacology, 2000. **23**(6): p. 667-75.
168. Leroy, C., et al., *Striatal and extrastriatal dopamine transporter in cannabis and tobacco addiction: a high-resolution PET study.* Addict Biol, 2012. **17**(6): p. 981-90.
169. Dubol, M., et al., *Dopamine Transporter and Reward Anticipation in a Dimensional Perspective: A Multimodal Brain Imaging Study.* Neuropsychopharmacology, 2018. **43**(4): p. 820-827.

170. Narendran, R., et al., *In vivo evidence for low striatal vesicular monoamine transporter 2 (VMAT2) availability in cocaine abusers.* Am J Psychiatry, 2012. **169**(1): p. 55-63.
171. Innis, R.B., et al., *Consensus nomenclature for in vivo imaging of reversibly binding radioligands.* J Cereb Blood Flow Metab, 2007. **27**(9): p. 1533-9.
172. R.E., C., *Tracer Kinetic Modeling in PET*, in *Positron Emission Tomography*, T.D.W. Bailey D.L., Valk P.E., Maisey M.N., Editor. 2005, Springer: London.
173. Herfert, K., et al., *Quantitative Rodent Brain Receptor Imaging.* Mol Imaging Biol, 2019.
174. Cunningham, V.J., et al., *Compartmental analysis of diprenorphine binding to opiate receptors in the rat in vivo and its comparison with equilibrium data in vitro.* J Cereb Blood Flow Metab, 1991. **11**(1): p. 1-9.
175. Zhou, Y., et al., *Linear regression with spatial constraint to generate parametric images of ligand-receptor dynamic PET studies with a simplified reference tissue model.* Neuroimage, 2003. **18**(4): p. 975-89.
176. Lammertsma, A.A. and S.P. Hume, *Simplified reference tissue model for PET receptor studies.* Neuroimage, 1996. **4**(3 Pt 1): p. 153-8.
177. Normandin, M.D., R.A. Koeppe, and E.D. Morris, *Selection of weighting factors for quantification of PET radioligand binding using simplified reference tissue models with noisy input functions.* Phys Med Biol, 2012. **57**(3): p. 609-29.
178. Zanderigo, F., R.T. Ogden, and R.V. Parsey, *Reference region approaches in PET: a comparative study on multiple radioligands.* J Cereb Blood Flow Metab, 2013. **33**(6): p. 888-97.
179. Gunn, R.N., et al., *Parametric imaging of ligand-receptor binding in PET using a simplified reference region model.* Neuroimage, 1997. **6**(4): p. 279-87.
180. Logan, J., et al., *Graphical analysis of reversible radioligand binding from time-activity measurements applied to [N-11C-methyl]-(-)-cocaine PET studies in human subjects.* J Cereb Blood Flow Metab, 1990. **10**(5): p. 740-7.
181. Zhang, L. and A. Villalobos, *Strategies to facilitate the discovery of novel CNS PET ligands.* EJNMMI Radiopharm Chem, 2017. **1**(1): p. 13.
182. Todd, M.M., J.B. Weeks, and D.S. Warner, *Cerebral blood flow, blood volume, and brain tissue hematocrit during isovolemic hemodilution with hetastarch in rats.* Am J Physiol, 1992. **263**(1 Pt 2): p. H75-82.
183. Zhao, R., et al., *Breast cancer resistance protein interacts with various compounds in vitro, but plays a minor role in substrate efflux at the blood-brain barrier.* Drug Metab Dispos, 2009. **37**(6): p. 1251-8.
184. Lee, Y.J., et al., *Investigation of efflux transport of dehydroepiandrosterone sulfate and mitoxantrone at the mouse blood-brain barrier: a minor role of breast cancer resistance protein.* J Pharmacol Exp Ther, 2005. **312**(1): p. 44-52.
185. Miller, D.S., B. Bauer, and A.M. Hartz, *Modulation of P-glycoprotein at the blood-brain barrier: opportunities to improve central nervous system pharmacotherapy.* Pharmacol Rev, 2008. **60**(2): p. 196-209.
186. Aller, S.G., et al., *Structure of P-glycoprotein reveals a molecular basis for poly-specific drug binding.* Science, 2009. **323**(5922): p. 1718-22.
187. Tournier, N., et al., *Discrepancies in the P-glycoprotein-mediated transport of (18)F-MPPF: a pharmacokinetic study in mice and non-human primates.* Pharm Res, 2012. **29**(9): p. 2468-76.
188. Syvanen, S., et al., *Species differences in blood-brain barrier transport of three positron emission tomography radioligands with emphasis on P-glycoprotein transport.* Drug Metab Dispos, 2009. **37**(3): p. 635-43.

189. Liow, J.S., et al., *Effect of a P-glycoprotein inhibitor, Cyclosporin A, on the disposition in rodent brain and blood of the 5-HT1A receptor radioligand, [11C](R)-(-)-RWAY.* Synapse, 2007. **61**(2): p. 96-105.
190. Yasuno, F., et al., *Quantification of serotonin 5-HT1A receptors in monkey brain with [11C](R)-(-)-RWAY.* Synapse, 2006. **60**(7): p. 510-20.
191. Lacan, G., et al., *Cyclosporine, a P-glycoprotein modulator, increases [18F]MPPF uptake in rat brain and peripheral tissues: microPET and ex vivo studies.* Eur J Nucl Med Mol Imaging, 2008. **35**(12): p. 2256-66.
192. Martin, C., et al., *The molecular interaction of the high affinity reversal agent XR9576 with P-glycoprotein.* Br J Pharmacol, 1999. **128**(2): p. 403-11.
193. Polli, J.W., et al., *Rational use of in vitro P-glycoprotein assays in drug discovery.* J Pharmacol Exp Ther, 2001. **299**(2): p. 620-8.
194. Honer, M., et al., *Radioligand development for molecular imaging of the central nervous system with positron emission tomography.* Drug Discov Today, 2014. **19**(12): p. 1936-44.
195. Patel, S. and R. Gibson, *In vivo site-directed radiotracers: a mini-review.* Nucl Med Biol, 2008. **35**(8): p. 805-15.
196. Tejani-Butt, S.M., *[3H]nisoxetine: a radioligand for quantitation of norepinephrine uptake sites by autoradiography or by homogenate binding.* J Pharmacol Exp Ther, 1992. **260**(1): p. 427-36.
197. Smith, H.R., T.J. Beveridge, and L.J. Porrino, *Distribution of norepinephrine transporters in the non-human primate brain.* Neuroscience, 2006. **138**(2): p. 703-14.
198. Tavares, A.A., et al., *(1)(2)(3)I-NKJ64: a novel single photon emission computed tomography radiotracer for imaging the noradrenaline transporter in brain.* Synapse, 2011. **65**(7): p. 658-67.
199. Tavares, A.A., et al., *Iodine-123 labeled reboxetine analogues for imaging of noradrenaline transporter in brain using single photon emission computed tomography.* Synapse, 2012. **66**(11): p. 923-30.
200. Shetty, H.U., et al., *Identification and regional distribution in rat brain of radiometabolites of the dopamine transporter PET radioligand [11C]PE2I.* Eur J Nucl Med Mol Imaging, 2007. **34**(5): p. 667-678.
201. Hirvonen, J., et al., *Measurement of striatal and extrastriatal dopamine transporter binding with high-resolution PET and [11C]PE2I: quantitative modeling and test-retest reproducibility.* J Cereb Blood Flow Metab, 2008. **28**(5): p. 1059-69.
202. Brown, A.K., et al., *Metabotropic glutamate subtype 5 receptors are quantified in the human brain with a novel radioligand for PET.* J Nucl Med, 2008. **49**(12): p. 2042-8.
203. Simeon, F.G., et al., *Synthesis and simple 18F-labeling of 3-fluoro-5-(2-(2-(fluoromethyl)thiazol-4-yl)ethynyl)benzonitrile as a high affinity radioligand for imaging monkey brain metabotropic glutamate subtype-5 receptors with positron emission tomography.* J Med Chem, 2007. **50**(14): p. 3256-66.
204. Zoghbi, S.S., et al., *On quantitative relationships between drug-like compound lipophilicity and plasma free fraction in monkey and human.* J Pharm Sci, 2012. **101**(3): p. 1028-39.
205. Joshi, E.M., et al., *Efficiency gains in tracer identification for nuclear imaging: can in vivo LC-MS/MS evaluation of small molecules screen for successful PET tracers?* ACS Chem Neurosci, 2014. **5**(12): p. 1154-63.
206. Ma, Y., et al., *Application of LC-MS to the analysis of new radiopharmaceuticals.* Mol Imaging Biol, 2003. **5**(6): p. 397-403.
207. Keu, K.V., et al., *Reporter gene imaging of targeted T cell immunotherapy in recurrent glioma.* Sci Transl Med, 2017. **9**(373).

208. Qin, C., et al., *Cell and gene therapy with reporter gene imaging in myocardial ischemia.* Hell J Nucl Med, 2017. **20**(3): p. 198-203.
209. Hsieh, C.H., et al., *Generation of destabilized herpes simplex virus type 1 thymidine kinase as transcription reporter for PET reporter systems in molecular genetic imaging.* J Nucl Med, 2008. **49**(1): p. 142-50.
210. Shimojo, M., et al., *A genetically targeted reporter for PET imaging of deep neuronal circuits in mammalian brains.* EMBO J, 2021. **40**(22): p. e107757.
211. Gambhir, S.S., et al., *Imaging gene expression: principles and assays.* J Nucl Cardiol, 1999. **6**(2): p. 219-33.
212. Lohith, T.G., et al., *Basic evaluation of FES-hERL PET tracer-reporter gene system for in vivo monitoring of adenoviral-mediated gene therapy.* Mol Imaging Biol, 2008. **10**(5): p. 245-52.
213. Chaudhuri, T.R., et al., *A noninvasive reporter system to image adenoviral-mediated gene transfer to ovarian cancer xenografts.* Gynecol Oncol, 2001. **83**(2): p. 432-8.
214. Tjuvajev, J.G., et al., *Comparison of radiolabeled nucleoside probes (FIAU, FHBG, and FHPG) for PET imaging of HSV1-tk gene expression.* J Nucl Med, 2002. **43**(8): p. 1072-83.
215. Wong, N., J. De Melo, and D. Tang, *PKM2, a Central Point of Regulation in Cancer Metabolism.* Int J Cell Biol, 2013. **2013**: p. 242513.
216. Mukherjee, J., et al., *Pyruvate kinase M2 expression, but not pyruvate kinase activity, is up-regulated in a grade-specific manner in human glioma.* PLoS One, 2013. **8**(2): p. e57610.
217. Israelsen, W.J., et al., *PKM2 isoform-specific deletion reveals a differential requirement for pyruvate kinase in tumor cells.* Cell, 2013. **155**(2): p. 397-409.
218. Shirai, T., et al., *The glycolytic enzyme PKM2 bridges metabolic and inflammatory dysfunction in coronary artery disease.* J Exp Med, 2016. **213**(3): p. 337-54.
219. Rees, M.L., et al., *A PKM2 signature in the failing heart.* Biochem Biophys Res Commun, 2015. **459**(3): p. 430-6.
220. Haywood, T., et al., *Positron emission tomography reporter gene strategy for use in the central nervous system.* Proc Natl Acad Sci U S A, 2019. **116**(23): p. 11402-11407.
221. Alves-Filho, J.C. and E.M. Palsson-McDermott, *Pyruvate Kinase M2: A Potential Target for Regulating Inflammation.* Front Immunol, 2016. **7**: p. 145.
222. Liu, C.T., et al., *Functional significance of evolving protein sequence in dihydrofolate reductase from bacteria to humans.* Proc Natl Acad Sci U S A, 2013. **110**(25): p. 10159-64.
223. Miller, L.W., et al., *In vivo protein labeling with trimethoprim conjugates: a flexible chemical tag.* Nat Methods, 2005. **2**(4): p. 255-7.
224. Sellmyer, M.A., et al., *Bacterial infection imaging with [(18)F]fluoropropyl-trimethoprim.* Proc Natl Acad Sci U S A, 2017. **114**(31): p. 8372-8377.
225. Honey, C.J., et al., *Predicting human resting-state functional connectivity from structural connectivity.* Proceedings of the National Academy of Sciences, 2009. **106**(6): p. 2035-2040.
226. Uddin, L.Q., *Complex relationships between structural and functional brain connectivity.* Trends in cognitive sciences, 2013. **17**(12): p. 600-602.
227. Achard, S., et al., *Hubs of brain functional networks are radically reorganized in comatose patients.* Proceedings of the National Academy of Sciences, 2012. **109**(50): p. 20608-20613.
228. Fox, M.D., et al., *The human brain is intrinsically organized into dynamic, anticorrelated functional networks.* Proc Natl Acad Sci U S A, 2005. **102**(27): p. 9673-8.

229. Fox, M.D., et al., *The human brain is intrinsically organized into dynamic, anticorrelated functional networks.* Proceedings of the National Academy of Sciences of the United States of America, 2005. **102**(27): p. 9673-9678.
230. Handwerker, D.A. and P.A. Bandettini, *Hemodynamic signals not predicted? Not so: a comment on Sirotin and Das (2009).* Neuroimage, 2011. **55**(4): p. 1409-12.
231. Sirotin, Y.B. and A. Das, *Anticipatory haemodynamic signals in sensory cortex not predicted by local neuronal activity.* Nature, 2009. **457**(7228): p. 475-9.
232. Buxton, R.B. and L.R. Frank, *A model for the coupling between cerebral blood flow and oxygen metabolism during neural stimulation.* J Cereb Blood Flow Metab, 1997. **17**(1): p. 64-72.
233. Boxerman, J.L., et al., *The intravascular contribution to fMRI signal change: Monte Carlo modeling and diffusion-weighted studies in vivo.* Magn Reson Med, 1995. **34**(1): p. 4-10.
234. Buckner, R.L., J.R. Andrews-Hanna, and D.L. Schacter, *The brain's default network: anatomy, function, and relevance to disease.* Ann N Y Acad Sci, 2008. **1124**: p. 1-38.
235. Andrews-Hanna, J.R., *The brain's default network and its adaptive role in internal mentation.* Neuroscientist, 2012. **18**(3): p. 251-70.
236. Lu, H., et al., *Rat brains also have a default mode network.* Proc Natl Acad Sci U S A, 2012. **109**(10): p. 3979-84.
237. Becerra, L., et al., *Robust reproducible resting state networks in the awake rodent brain.* PLoS One, 2011. **6**(10): p. e25701.
238. Jonckers, E., et al., *Functional connectivity fMRI of the rodent brain: comparison of functional connectivity networks in rat and mouse.* PLoS One, 2011. **6**(4): p. e18876.
239. Wehrl, H.F., et al., *Simultaneous PET-MRI reveals brain function in activated and resting state on metabolic, hemodynamic and multiple temporal scales.* Nat Med, 2013. **19**(9): p. 1184-9.
240. Amend, M., et al., *Functional resting-state brain connectivity is accompanied by dynamic correlations of application-dependent [(18)F]FDG PET-tracer fluctuations.* Neuroimage, 2019. **196**: p. 161-172.
241. Ionescu, T.M., et al., *Elucidating the complementarity of resting-state networks derived from dynamic [(18)F]FDG and hemodynamic fluctuations using simultaneous small-animal PET/MRI.* Neuroimage, 2021. **236**: p. 118045.
242. Gottlich, M., et al., *Altered resting state brain networks in Parkinson's disease.* PLoS One, 2013. **8**(10): p. e77336.
243. Badhwar, A., et al., *Resting-state network dysfunction in Alzheimer's disease: A systematic review and meta-analysis.* Alzheimers Dement (Amst), 2017. **8**: p. 73-85.
244. Bluhm, R.L., et al., *Spontaneous low-frequency fluctuations in the BOLD signal in schizophrenic patients: anomalies in the default network.* Schizophr Bull, 2007. **33**(4): p. 1004-12.
245. Vouillot, L., A. Thelie, and N. Pollet, *Comparison of T7E1 and surveyor mismatch cleavage assays to detect mutations triggered by engineered nucleases.* G3 (Bethesda), 2015. **5**(3): p. 407-15.
246. Lopez-Gonzalez, F.J., et al., *QModeling: a Multiplatform, Easy-to-Use and Open-Source Toolbox for PET Kinetic Analysis.* Neuroinformatics, 2019. **17**(1): p. 103-114.
247. Schiffer, W.K., et al., *Serial microPET measures of the metabolic reaction to a microdialysis probe implant.* J Neurosci Methods, 2006. **155**(2): p. 272-84.
248. Logan, J., *Graphical analysis of PET data applied to reversible and irreversible tracers.* Nucl Med Biol, 2000. **27**(7): p. 661-70.
249. Ungerstedt, U. and G.W. Arbuthnott, *Quantitative recording of rotational behavior in rats after 6-hydroxy-dopamine lesions of the nigrostriatal dopamine system.* Brain Res, 1970. **24**(3): p. 485-93.

250. West, M.J., *Stereological methods for estimating the total number of neurons and synapses: issues of precision and bias.* Trends Neurosci, 1999. **22**(2): p. 51-61.
251. Paasonen, J., et al., *Functional connectivity under six anesthesia protocols and the awake condition in rat brain.* Neuroimage, 2018. **172**: p. 9-20.
252. Judenhofer, M.S., et al., *Simultaneous PET-MRI: a new approach for functional and morphological imaging.* Nat Med, 2008. **14**(4): p. 459-65.
253. Ionescu, T.M., et al., *Striatal and prefrontal D2R and SERT distributions contrastingly correlate with default-mode connectivity.* Neuroimage, 2021. **243**: p. 118501.
254. Matthew Brett, J.-L.A., Romain Valabregue, Jean-Baptiste Poline, *Region of interest analysis using an SPM toolbox*, in *8th Internation Conference on Functional Mapping of the Human Brain*. June 2-6, 2002: Sendai, Japan.
255. Rubinov, M. and O. Sporns, *Complex network measures of brain connectivity: uses and interpretations.* Neuroimage, 2010. **52**(3): p. 1059-69.
256. Miyanishi, K., et al., *Behavioral tests predicting striatal dopamine level in a rat hemi-Parkinson's disease model.* Neurochem Int, 2019. **122**: p. 38-46.
257. Tomasi, D., et al., *Dopamine transporters in striatum correlate with deactivation in the default mode network during visuospatial attention.* PLoS One, 2009. **4**(6): p. e6102.
258. Sambataro, F., et al., *DRD2 genotype-based variation of default mode network activity and of its relationship with striatal DAT binding.* Schizophr Bull, 2013. **39**(1): p. 206-16.
259. Hume, S.P., et al., *Effect of L-dopa and 6-hydroxydopamine lesioning on [11C]raclopride binding in rat striatum, quantified using PET.* Synapse, 1995. **21**(1): p. 45-53.
260. Mishra, R.K., A.M. Marshall, and S.L. Varmuza, *Supersensitivity in rat caudate nucleus: effects of 6-hydroxydopamine on the time course of dopamine receptor and cyclic AMP changes.* Brain Res, 1980. **200**(1): p. 47-57.
261. Creese, I., D.R. Burt, and S.H. Snyder, *Dopamine receptor binding enhancement accompanies lesion-induced behavioral supersensitivity.* Science, 1977. **197**(4303): p. 596-8.
262. Konieczny, J., et al., *The significance of rotational behavior and sensitivity of striatal dopamine receptors in hemiparkinsonian rats: A comparative study of lactacystin and 6-OHDA.* Neuroscience, 2017. **340**: p. 308-318.
263. Wang, Y.M., et al., *Knockout of the vesicular monoamine transporter 2 gene results in neonatal death and supersensitivity to cocaine and amphetamine.* Neuron, 1997. **19**(6): p. 1285-96.
264. Seeman, P., et al., *Dopamine receptors in the central nervous system.* Fed Proc, 1978. **37**(2): p. 131-6.
265. Gnanalingham, K.K. and R.G. Robertson, *The effects of chronic continuous versus intermittent levodopa treatments on striatal and extrastriatal D1 and D2 dopamine receptors and dopamine uptake sites in the 6-hydroxydopamine lesioned rat--an autoradiographic study.* Brain Res, 1994. **640**(1-2): p. 185-94.
266. Graham, W.C., A.R. Crossman, and G.N. Woodruff, *Autoradiographic studies in animal models of hemi-parkinsonism reveal dopamine D2 but not D1 receptor supersensitivity. I. 6-OHDA lesions of ascending mesencephalic dopaminergic pathways in the rat.* Brain Res, 1990. **514**(1): p. 93-102.
267. Antonini, A., et al., *Long-term changes of striatal dopamine D2 receptors in patients with Parkinson's disease: a study with positron emission tomography and [11C]raclopride.* Mov Disord, 1997. **12**(1): p. 33-8.
268. Zigmond, M.J., T.G. Hastings, and R.G. Perez, *Increased dopamine turnover after partial loss of dopaminergic neurons: compensation or toxicity?* Parkinsonism Relat Disord, 2002. **8**(6): p. 389-93.

269. Huang, S., et al., *Multisensory Competition Is Modulated by Sensory Pathway Interactions with Fronto-Sensorimotor and Default-Mode Network Regions.* J Neurosci, 2015. **35**(24): p. 9064-77.
270. Wu, C.W., et al., *Synchrony Between Default-Mode and Sensorimotor Networks Facilitates Motor Function in Stroke Rehabilitation: A Pilot fMRI Study.* Front Neurosci, 2020. **14**: p. 548.
271. Wang, J., et al., *Functional reorganization of intra- and internetwork connectivity in major depressive disorder after electroconvulsive therapy.* Hum Brain Mapp, 2018. **39**(3): p. 1403-1411.
272. Perlbarg, V., et al., *Alterations of the nigrostriatal pathway in a 6-OHDA rat model of Parkinson's disease evaluated with multimodal MRI.* PLoS One, 2018. **13**(9): p. e0202597.
273. Monnot, C., et al., *Asymmetric dopaminergic degeneration and levodopa alter functional corticostriatal connectivity bilaterally in experimental parkinsonism.* Exp Neurol, 2017. **292**: p. 11-20.
274. Honey, G.D., et al., *Dopaminergic drug effects on physiological connectivity in a human cortico-striato-thalamic system.* Brain, 2003. **126**(Pt 8): p. 1767-81.
275. Kwak, Y., et al., *Altered resting state cortico-striatal connectivity in mild to moderate stage Parkinson's disease.* Front Syst Neurosci, 2010. **4**: p. 143.
276. Costa, R.M., et al., *Rapid alterations in corticostriatal ensemble coordination during acute dopamine-dependent motor dysfunction.* Neuron, 2006. **52**(2): p. 359-69.
277. Gatev, P., O. Darbin, and T. Wichmann, *Oscillations in the basal ganglia under normal conditions and in movement disorders.* Mov Disord, 2006. **21**(10): p. 1566-77.
278. Hammond, C., H. Bergman, and P. Brown, *Pathological synchronization in Parkinson's disease: networks, models and treatments.* Trends Neurosci, 2007. **30**(7): p. 357-64.
279. Eusebio, A., et al., *Resonance in subthalamo-cortical circuits in Parkinson's disease.* Brain, 2009. **132**(Pt 8): p. 2139-50.
280. Brazhnik, E., et al., *State-dependent spike and local field synchronization between motor cortex and substantia nigra in hemiparkinsonian rats.* J Neurosci, 2012. **32**(23): p. 7869-80.
281. Moran, R.J., et al., *Alterations in brain connectivity underlying beta oscillations in Parkinsonism.* PLoS Comput Biol, 2011. **7**(8): p. e1002124.
282. Gerfen, C.R. and D.J. Surmeier, *Modulation of striatal projection systems by dopamine.* Annu Rev Neurosci, 2011. **34**: p. 441-66.
283. Caspers, J., et al., *Differential Functional Connectivity Alterations of Two Subdivisions within the Right dlPFC in Parkinson's Disease.* Front Hum Neurosci, 2017. **11**: p. 288.
284. Owens-Walton, C., et al., *Increased functional connectivity of thalamic subdivisions in patients with Parkinson's disease.* PLoS One, 2019. **14**(9): p. e0222002.
285. Kahn, I., et al., *Distinct cortical anatomy linked to subregions of the medial temporal lobe revealed by intrinsic functional connectivity.* J Neurophysiol, 2008. **100**(1): p. 129-39.
286. Vincent, J.L., et al., *Coherent spontaneous activity identifies a hippocampal-parietal memory network.* J Neurophysiol, 2006. **96**(6): p. 3517-31.
287. Hillary, F.G., et al., *Hyperconnectivity is a fundamental response to neurological disruption.* Neuropsychology, 2015. **29**(1): p. 59-75.
288. Klobusiakova, P., et al., *Connectivity Between Brain Networks Dynamically Reflects Cognitive Status of Parkinson's Disease: A Longitudinal Study.* J Alzheimers Dis, 2019. **67**(3): p. 971-984.
289. Mevel, K., et al., *The default mode network in healthy aging and Alzheimer's disease.* Int J Alzheimers Dis, 2011. **2011**: p. 535816.

290. Gorges, M., et al., *To rise and to fall: functional connectivity in cognitively normal and cognitively impaired patients with Parkinson's disease.* Neurobiol Aging, 2015. **36**(4): p. 1727-1735.
291. Helmich, R.C., et al., *Spatial remapping of cortico-striatal connectivity in Parkinson's disease.* Cereb Cortex, 2010. **20**(5): p. 1175-86.
292. Liu, Z., et al., *Tissue Specific Expression of Cre in Rat Tyrosine Hydroxylase and Dopamine Active Transporter-Positive Neurons.* PLoS One, 2016. **11**(2): p. e0149379.
293. Bjorklund, A. and S.B. Dunnett, *Dopamine neuron systems in the brain: an update.* Trends Neurosci, 2007. **30**(5): p. 194-202.
294. Piel, M., I. Vernaleken, and F. Rosch, *Positron Emission Tomography in CNS Drug Discovery and Drug Monitoring.* Journal of Medicinal Chemistry, 2014. **57**(22): p. 9232-9258.
295. Van de Bittner, G.C., E.L. Ricq, and J.M. Hooker, *A Philosophy for CNS Radiotracer Design.* Accounts of Chemical Research, 2014. **47**(10): p. 3127-3134.
296. Kubo, Y., et al., *Quantitative Determination of Luminal and Abluminal Membrane Distributions of Transporters in Porcine Brain Capillaries by Plasma Membrane Fractionation and Quantitative Targeted Proteomics.* Journal of Pharmaceutical Sciences, 2015. **104**(9): p. 3060-3068.
297. Fowler, J.S., et al., *Species differences in [C-11]clorgyline binding in brain.* Nuclear Medicine and Biology, 2001. **28**(7): p. 779-785.

Declaration of contribution

The dissertation work was carried out at the Department of Preclinical Imaging and Radiopharmacy, Werner Siemens Imaging Center, Eberhard Karls University, Tuebingen, under the supervision of Prof. Kristina Herfert.

Italic content in quotes refers to the original publication [1].

After training by laboratory members Laura Kübler, Sandro Aidone, Maren Harant, Linda Schramm, Funda Cay, I carried out all experiments independently. I confirm that I wrote the doctoral thesis myself, under the supervision of Prof. Kristina Herfert, and that any additional sources of information have been duly cited.

MSc. Tudor Mihai Ionescu, Department of Preclinical Imaging and Radiopharmacy, Werner Siemens Imaging Center, Eberhard Karls University, Tuebingen, has performed the pre-processing and analysis of the PET and PET/BOLD-fMR imaging data. MSc. Ran Sing Saw, Department of Preclinical Imaging and Radiopharmacy, Werner Siemens Imaging Center, Eberhard Karls University, Tuebingen, aided performing the *ex vivo* TH and VMAT2 stainings. Dr. Rachel Cheong, BRAIN Department, University of Lund, Sweden, performed the HPLC experiments and processing of the TH stained brain sections for the stereology.

Dr. Andreas Maurer, Dominik Seyfried, Ramona Stremme, Elena Kimmerle and Johannes Kinzler, Department of Preclinical Imaging and Radiopharmacy, Werner Siemens Imaging Center, Eberhard Karls University, Tuebingen, performed the radioligand syntheses.

Prof. Dr. Deniz Kirik, BRAIN Department, University of Lund, Sweden and Prof. Dr. Bernd Pichler, Department of Preclinical Imaging and Radiopharmacy, Werner Siemens Imaging Center, Eberhard Karls University, Tuebingen, gave access to the labs and resources and provided additional funding.

Prof. Dr. Kristina Herfert, Department of Preclinical Imaging and Radiopharmacy, Werner Siemens Imaging Center, Eberhard Karls University, Tuebingen, created the concept of the study, supervised the doctoral thesis and was involved in the acquisition of funding.

Acknowledgements

I thank the technical assistants Sandro Aidone, Daniel Bukala, Linda Schramm, Maren Harant at the Department of Preclinical Imaging and Radiopharmacy, Werner Siemens Imaging Center, Eberhard Karls University, Tuebingen for their technical support. I also thank Ulla Samuelsson, Ulrika Sparrhult-Björk, Dr. Ulrika Schagerlöf, Anneli Josefsson and Anna Hansen at Lund University, Sweden for their technical support. I acknowledge Dr. Julia Mannheim, Dr. Andreas Schmid, Dr. Rebecca Rock, Ines Herbon, Dr. Neele Hübner, Dr. Andreas Dieterich, Hans Jörg Rahm, Dr. Carsten Calaminus, Funda Cay, Kristin Patzwaldt, Laura Kübler, Marilena Poxleitner, Sabrina Buss for their administrative, technical, and experimental support at the Department of Preclinical Imaging and Radiopharmacy, Werner Siemens Imaging Center, Eberhard Karls University, Tuebingen.

Funding

Werner Siemens Foundation and Deutscher Akademischer Austauschdienst